Atomistic Simulation Studies of Li$_2$MnO$_3$ Nanoarchitectures

By

TSHIDI MOGASHOA

THESIS

Submitted in fulfilment of the requirements for the degree of

DOCTOR OF PHILOSOPHY (PhD)

In

Physics

In the

FACULTY OF SCIENCE AND AGRICULTURE

(School of Physical and Mineral Sciences)

University of Limpopo
South Africa

Supervisor: Prof. P.E. Ngoepe
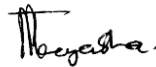
Co-supervisor: Prof. R. S. Ledwaba

[2023]

Declaration

I declare that the work hereby submitted to the University of Limpopo for the PhD degree in Physics is my original work and has not been submitted before for any other degree at any institution and that the materials contained herein have been acknowledged through complete references.

Mrs T. Mogashoa

Signature:

Student Number: ████████   Date 24/07/2023

Dedication

This thesis is dedicated to my loving husband Danny Mogashoa, my two beloved daughters Thoriso and Letago, my mother Linah Malibe, my late father Isaac Malibe and my sisters, Rose, Mosima, Phindile and Basetsana.

Acknowledgements

.

Abstract

High-energy lithium-ion batteries (LIBs) are in high demand for the establishment of electric vehicles and hybrid vehicles in the automotive sector. Considering that the cathode is the limiting factor, it is of significant importance to discover cathode materials with a large number of lithiums, as this has a positive effect on the voltage, capacity and potential difference required for the advancement of the next-generation LIBs. Lithium manganite (Li_2MnO_3), owing to its huge capacity (458 mAh.g^{-1}), nontoxicity and affordability has been considered an active cathode material for high-capacity LIBs. However, its capacity degradation and phase transformation during the cycling process are the main limiting factors to its commercialisation. The mechanisms behind these degradations are not yet fully understood to enable a complete diagnosis of the drawback. Sodium-ion doping at the Li-sites of Li_2MnO_3 can, however, mitigate structural transformation during the charge/discharge process by prohibiting the migration of manganese ions from the transition metal (TM) layers to lithium layers.

In this work, the simulated amorphisation and recrystallisation (A+R) technique was employed during the high-temperature synthesis of Li_2MnO_3 nano-architectures i.e. nanosphere, nanoporous and the bulk material consisting of a large number of atoms (32148). Nanostructuring, due to the advantage in particle size reduction, has been considered, owing to the large surface exposure and shortened diffusion path. Thus facilitating effective activation of the Li_2MnO_3 electrode material. The nano-architectures were investigated between the temperature range of 1500 K and 1900 K as guided by the melting point, which was found to be around 1845 K, from the total energy graph. Recrystallisation of the Li_2MnO_3 models was confirmed by the radial distribution functions (RDFs) which depicted multiple sharp peaks due to the long-range ordering of atoms and strong bonds. Structural validation through the x-ray diffraction plots (XRD) compared very well with experimental work in literature, displaying broadening, splitting and partial shifting of peaks resulting from the mixing of Li and Mn layers. However, the nanosphere depicted broader peaks compared to both the nanoporous and bulk systems. The microstructural features that evolved during the recrystallisation of all the models contained cation mixing and vacancies resulting in structures constituting mixed layers.

Li-ion kinetics for the nanosphere model was found to be higher (approximately 1.54 nm^2s^{-1}) than in the nanoporous and bulk systems which were below 0.3 nm^2s^{-1}.

The Li_2MnO_3 nanosphere model was then used to dope sodium ions into the Li-sites. Accordingly, a series of $Li_{2-x}Na_xMnO_3$ (0≤x≤2) nanosphere models of different lithium and sodium content were generated via the amorphisation and recrystallisation strategy. The results thereof showed structural collapse upon amorphisation for systems containing a large dosage of Na-ions. However, systems with 25% Na content and below, were successfully amorphised and recrystallised at 1700 K, while retaining their structural morphology, with the $Li_{1.75}Na_{0.25}MnO_3$ system resulting in a polycrystalline structure. The microstructural analysis also revealed the mixing of layers and improved structural arrangement for the $Li_{1.95}Na_{0.05}MnO_3$ system, which showed a large portion of a well-ordered Li_2MnO_3 phase. Li-ion mobility for the Na-incorporated systems was found to be higher compared to the undoped systems with the system containing the lowest Na-ions ($Li_{1.975}Na_{0.025}MnO_3$) diffusing better. This proves that incorporating sodium ions into the Li_2MnO_3 lattice aid in improving the ionic movement. XRD analysis revealed peaks with a broad character. The Peaks belonging to 2Θ~38 slightly shift to the right as a result of the enlarged Li-layers which are occupied by Na ions. The enlargement of the Li-layers facilitates Li-ion kinetics. Again, superlattice peaks were observed for the $Li_{1.95}Na_{0.05}MnO_3$ at lower angles due to the ordering of Li/Mn ions in the transitional metal layers.

Charging was achieved by simultaneously removing Li^+ and O^- ions from the outer surfaces of the Li_2MnO_3 and $Li_{2-x}Na_xMnO_3$ nanoarchitectures. All the Li/O deficient systems crystallised into multi-grained crystals with grain boundaries increasing with a decrease in Li/O content for the undoped systems. For the Na-incorporated systems, the $Li_{1.95}Na_{0.05}MnO_3$ revealed minimal grain boundaries as Li/O was varied, with the $Li_{1.70}Na_{0.05}MnO_{2.75}$ and $Li_{1.45}Na_{0.05}MnO_{2.50}$ concentrations showing no formation of grain boundaries. Characterisation of the XRD for the charged systems also resulted in broad peaks, accompanied by the growth of peaks 2Θ~18-25º peak and the 2Θ~29º associated with the spinel phase. Contrarily, the nanoporous system ($Li_{1.25}MnO_{2.25}$) depicts the narrowing and decreasing of diffraction peaks at 2Θ~18-25 and 2Θ~29º. The $Li_{2-x}Na_xMnO_3$ systems also depict the narrowing and decreasing of the peak at approximately

2Θ~38⁰. In addition, the complex internal microstructures of the Li/O deficient models ($Li_{2-x}MnO_{3-x}$) revealed structures governed by defects. These defects contribute to the evolution of distorted $LiMn_2O_4$, Li_2MnO_3 and $LiMnO_2$ polymorphs. The spontaneous migration of manganese into the lithium layers triggers the transformation from layered to spinel-type configurations. The charging of the $Li_{1.95}Na_{0.05}MnO_3$ system resulted in improved structural stability, with structures revealing a high concentration of the layered Li_2MnO_3 structure. Again, the diffusion has been improved by doping sodium into the lithium sites of the Li_2MnO_3 nanosphere upon charging. Our results accentuate the process or mechanism behind the charging of the Li_2MnO_3 and $Li_{2-x}Na_xMnO_3$ constituting complex structures. This study will help guide the optimisation of high-capacity cathodes for advanced LIB technologies.

Table of Contents

List of Tables

List of Figures

xiv

CHAPTER 1

1.1. Introduction and General Background

Energy storage technologies play a central role in addressing the global challenge of clean and sustainable energy by replacing fossil fuels with renewable energy sources such as solar and wind [1]. Lithium-ion batteries (LIBs) are thus far the most dominant power source for portable electronic devices and the potential candidate for providing higher energy density required in powering emerging technologies such as electric vehicles (EV), hybrid-electric vehicles (HEV) and grid-scale energy storages [2, 3]. However, for their complete realisation of these emerging technologies, the performance, safety and life span must be improved with reduced cost [4]. Considering that traditional cathodes materials i.e. layered $LiCoO_2$, olivine $LiFePO_4$ and spinel $LiMn_2O_4$ cannot fulfil the demand due to limited theoretical capacity [5], It is therefore of paramount importance to improve or explore alternative high-capacity electrode materials that will offer higher energy densities [2, 6, 7].

Lithium-rich layered oxides (LLO) are being pursued as high-capacity LIB cathodes due to their high energy density, low cost, non-toxicity and the ability to reversibly intercalate more lithium ions than traditional cathode materials [8, 9, 10]. Owing to its high theoretical capacity of 458 $mAh.g^{-1}$ [11], Li_2MnO_3 is one of the most prominent positive electrode materials. However, the pristine material requires electrochemical activation. Furthermore, the structural transformation from the layered rock-salt to spinel-type as a result of the spontaneous migration of Mn ions into the Li layer has been reported during Lithium extraction and thus causes irreversible capacity loss [10, 12]. However, the reasons governing the undesirable behaviour of this material remain ambiguous. Accordingly, understanding the effect of the synthesis route on the properties of this electrode material may be of great importance for the desired high-performance LIBs [13].

The generation of nanosized cathode materials has been considered for the electrochemical enhancement of LIBs owing to advantageous properties such as high surface exposure and shortened Li^+ diffusion path in nanomaterials [14, 15]. Electrochemically inactive materials such as $LiFeO_3$ [16] and Li_2MnO_3 [17] have been reported as active when synthesized in a nano form. In addition, nanomaterial can better accommodate strains and structural transitions suggesting that the structural changes in nanoscaled cathodes can be minimized thus preserving the integrity of the material. However, the synthesis of nanomaterials is not as easy as it is for bulk materials. The size and dimensions require to be monitored and controlled during synthesis [16].

In order to address the instability of lithium-rich electrodes during cycling, sodium ions have been introduced in an attempt to enhance their electrochemical performance [18, 19]. The introduction of small amounts of sodium into the Li-sites enlarges the interplanar spacing allowing for smooth Li-ion movement during the charge/discharge, and also, helps in stabilizing the structure from collapsing. Moreover, the presence of sodium ions minimizes the migration of manganese ions from the transition metal layers to the lithium layers which contributes significantly to the transition from layered to spinel-like structures [5]. Figure 1.1 (a) below illustrates the widespread LIB applications from portable electronics to large-scale applications. The illustration in (b) is the schematic presentation of the charge/discharge mechanism where the anode and cathode are capable of reversible Li-ion intercalation/deintercalation at different potentials. During charging, lithium ions travel from the positive electrode through the electrolyte into the negative electrode. The discharge process is the reverse of the charging process.
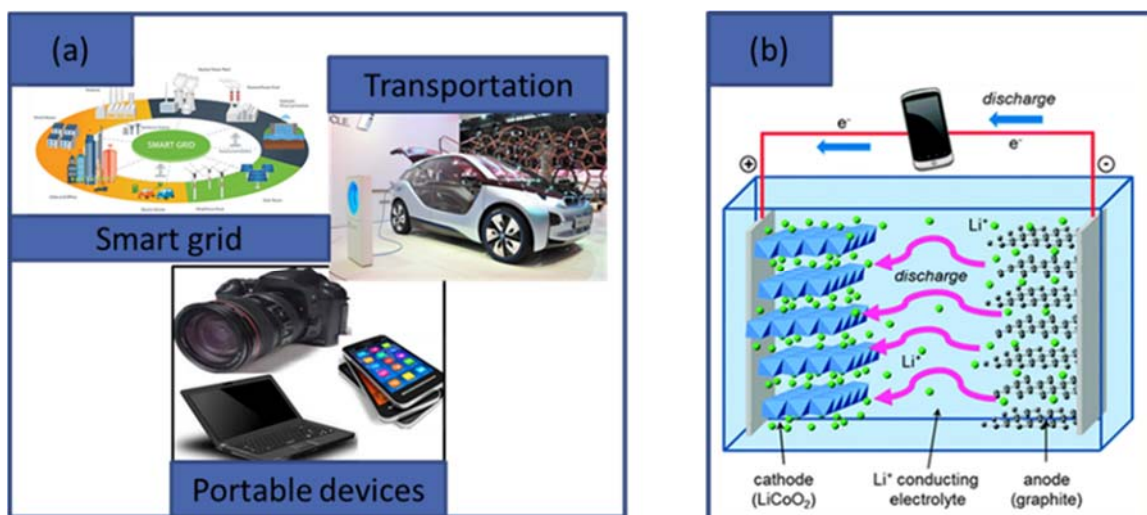
Figure 1.1: (a) Applications of lithium-ion batteries (LIBs) including portable electronic devices (camera, cellphones and laptop), electric cars and smart grid, (b) schematic illustrating the discharge mechanism of a LIB.

1.2. Literature Review

Owing to the immense theoretical capacity of 458 mAh.g^{-1} and low cost due to the wide distribution of manganese [20], Li_2MnO_3 has emerged as a promising cathode material for the next-generation lithium-ion batteries. However, the origin and mechanism governing this anomalous capacity have not yet been elucidated. Consequently, studies have insinuated that it originates from the high number of exploitable lithium ions [11]. Others believe the capacity has to do with oxygen losing its electrons during cycling causing manganese migration to the lithium layer and subsequent structural deterioration and voltage fade [21, 22].

1.2.1 Drawbacks of Layered Li_2MnO_3

Layered Li_2MnO_3 is classified as an active intercalation host material for LIBs and has the potential of doubling the specific capacity available in earlier LIBs with $LiCoO_2$ cathode material [23]. However, there are some drawbacks hindering its widespread applications.

The Li_2MnO_3 exhibits extensive structural defects, such as the mixing of layers and stacking faults. These defects make their precise structural analysis difficult [24]. This degradation behaviour originates from factors such as the loss of oxygen during cycling and Li^+ /H^+ exchange reaction [12], which must be conquered before their plausible use. In addition, Li_2MnO_3 in its bulk crystalline form requires electrochemical

activation in the first charge-discharge cycle. This, however, results in low coulombic efficiency and poor electrochemical properties [25, 26]. The reason for its inactivity is believed to be due to the ordered distribution of Li and Mn in the transition layers, which leads to the inability of Mn^{4+} to be further oxidized to Mn^{5+} [27, 28]. This restricts the amount of lithium that can be extracted from the Li_2MnO_3 since the removal of lithium is accompanied by the oxidation of Mn. Moreover, the capacity of the battery to store charge is also affected by the inability of Mn to be further oxidized [29]. However, activation can be achieved by leaching Li or Li_2O from the structure and these Li-deficient compounds have high intercalation capacities and good reversibility [30]. It has been reported that Li_2MnO_3 undergoes a two-step electrochemical reaction where the Li^+ ion is lost with the corresponding amount of oxygen resulting in a total loss of Li_2O and the formation of electrochemically active MnO_2 which is responsible for the intercalation/deintercalation [10].

1.2.2 Strategies to Improve Li_2MnO_3

The intrinsic drawbacks associated with the layered Li_2MnO_3 cathodes i.e. structural degradation, voltage fade and low cycle life must be addressed to realize their application in LIB technologies. Considerable research has been focused on proposed strategies to improve the performance of Li_2MnO_3 cathodes including, cationic doping to minimize the voltage fade and stabilize the structure, surface coating to surpass side reactions, introducing oxide containing Li with good conductivity to provide a Li^+ diffusion tunnel and thermal reduction to improve the capabilities [16, 25].

Considering that activation is required prior operation of the Li_2MnO_3 in its crystalline form, it was found that when synthesized in a nanocrystalline form, Li_2MnO_3 requires no activation and yields capacities up to 200 mAh.g^{-1} and excellent capacity retention over multiple cycles [31]. To elucidate the mechanism behind this activation, a study instituted that the nanosized Li_2MnO_3 comprises manganese defects which are absent on the bulk. These defects then act as a scaffold holding open the Li-ions during the charge/discharge process thus preventing the structure from collapsing [17]. In addition, fully activated Li_2MnO_3 nanoparticles were prepared through a chemical oxidation reaction and delivered a charge capacity of 302 mAh.g^{-1} above 4.5 V and a discharge capacity of 236 mAg^{-1} during the first cycle [32]. In another study, hydrothermal synthesis was used in the fabrication of well-crystallised Li_2MnO_3

4

nanoparticles with a reversible capacity of 243 mAh.g^{-1} charge/discharge between 2.0 - 4.3 V [33].

The electrochemical performance of Li_2MnO_3 was investigated by doping the Mn site with aluminium, doping exhibits an enhancement in the rate capability and cycling stability [34]. It was also established that doping Al on the Mn site enhanced the Li content and the favourable isovalent dopants were found to be Si^{4+} and Ge^{4+} [35]. Furthermore, partially substituting one of the Li_2MnO_3 elements is another way of enhancing the cycle stability which ascribes to reduced deintercalation barriers of Li ions and also improved the transference of electrons within the material [25].

Layered-layered oxide composite cathodes of composition Li_2MnO_3 (1−x) $LiMO_2$ (M = Ni, Mn, etc.), are capable of doubling the capacity available in the earlier generation of Li-ion batteries based on $LiCoO_2$ [23]. The layered component plays a significant role in storing excess lithium, proving stability against oxygen loss and securing the high voltage and specific capacity [16]. However, the difficulty in synthesis, characterisation and selection of a compatible combination of phases remains a challenge [36].

Embedding the spinel $LiMn_2O_4$ into Li_2MnO_3 is another strategy that can improve the structural instability during the charging of the Li_2MnO_3 cathode [25]. For example, a composite structure with the spinel $LiMn_2O_4$ was formed by mechanical milling displaying its initial discharge capacity at approximately 400 mAh.g^{-1} and its 50th discharge capacity to be more than 70% of the initial discharge capacity. The spinel in the composite help restricts the emission of oxygen from the Li_2MnO_3 [37]. In addition to the strategies mentioned above, thermal reduction has also been considered for enhancing the electrochemical properties of Li_2MnO_3 cathodes. The ion exchange and oxygen reaction using $Na_{0.44}MnO_2$ nanobelts precursor were used in generating Li_2MnO_3 nanobelts. The low temperature reduced Li_2MnO_3 nanobelts and showed improved electrochemical performance compared to the pristine Li_2MnO_3 and also revealed a high level of structural defects such as oxygen vacancies, stacking faults and the presence of orthorhombic $LiMnO_2$ morphology [25].

Simulated amorphisation and recrystallisation (A+R) based on classical molecular methods have been used in generating models with ever-increasing structural

complexity. This method allows for the spontaneous crystal growth of materials displaying microstructural features observed experimentally, such as grain boundaries, point defects and dislocations. Consequently, the same method was used in simulating the synthesis of the Li_2MnO_3 [17].

1.2.3 Structural Description

Li_2MnO_3 constitute a layered structure and can be written as $Li[Li_{1/3}Mn_{2/3}]O_2$, with a space group C2/m and lattice parameters a = 4.937 Å, b = 8.532 Å, c =5.030 Å and β =109.46º. It is an O3-type structure where Li-ions occupy the interslab octahedral sites and Li/Mn occupy slab octahedral sites in a ratio of 1:2 to minimise strain [38, 39]. Each Mn atom forms a local octahedral structure with six neighbouring oxygen atoms (MnO_6) and its oxidation number is 4^+ in the pristine structure [11].
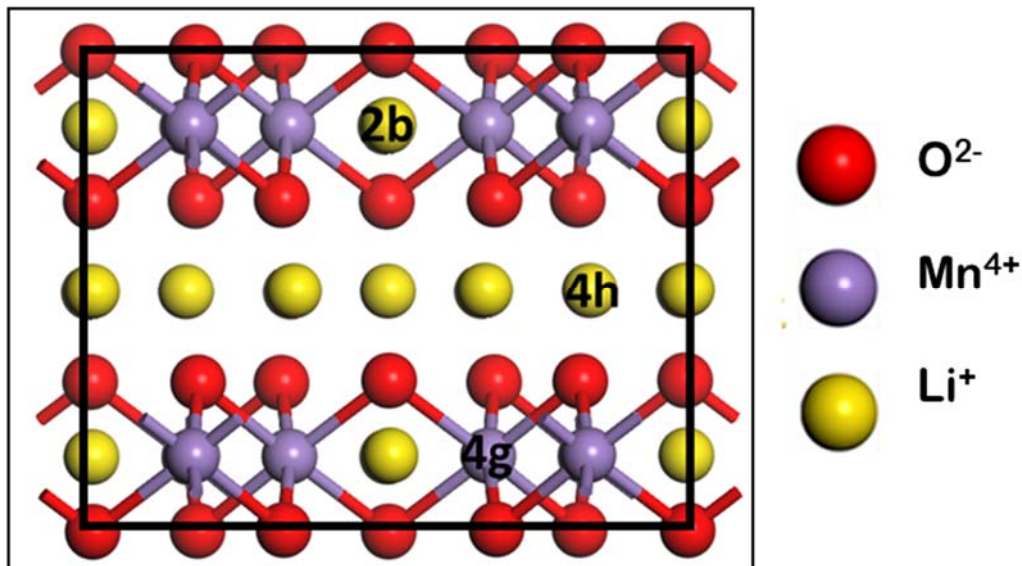
Figure 1.2: Li_2MnO_3 conventional unit cell showing the occupancy of manganese on the 4g sites, lithium atoms on 2b and 4h sites. The red, yellow and purple spheres represent oxygen, lithium and manganese atoms respectively.

1.3   Intentions of the Study

The inadequacy of fossil fuels and their effect on global warming has become the driving force behind renewable and sustainable energy technologies. Despite the progress made in LIB technology, there are still some critical issues that need to be addressed, such as energy density, rate capability, cycling performance and safety problems [13]. The cathode is one component of a LIB that plays a significant role in determining its performance [40] and as such, considerable research has been

focused on various kinds of lithiated transition metal oxides for their possible use as cathode materials in advanced LIBs [41]. Amongst these materials, lithium-rich layered cathodes take the lead due to their high capacity. However, they suffer from inferior rate capability resulting from the intrinsic poor electronic conductivity and slow lithium diffusion [40]. Various strategies have been considered to improve these drawbacks including cationic doping, surface coating and thermal reduction [16, 25]. Also, nanosizing has been highly recommended especially on other Li-M-O electrodes, owing to the immense influence of the particle size and surface morphology on the overall performance of the battery [42, 43]. Moreover, nanostructured electrodes can be a viable route to quickly deliver the power required for Li-ion electric vehicles [20]. Particularly, nanoporous structures contribute to superior electronic performance and highly crystallised facets exposed to the surface which contributes to the structural stability of electrode materials [44].

The primary goal of the proposed study is to simulate the synthesis of nanosized Li_2MnO_3 lithium-ion battery cathode materials using large-scale atomistic simulation technique amorphisation and recrystallisation (A+R). This technique is based on classical molecular dynamics simulations and is capable of the spontaneous nucleation and crystal growth of nanomaterials as simulated previously for other binary electrodes such as MnO_2 [43, 45], TiO_2 [46, 47], ternary Li_2MnO_3 [17] and $LiMn_2O_4$ [48] for LIB applications. Furthermore, models produced using this technique display microstructural features such as grain boundaries, dislocations and point defects similar to those observed experimentally. The generation of the Li_2MnO_3 nanostructures will be followed by the doping of sodium ions into the Li_2MnO_3 lattice in an attempt to enhance the electrochemical performance of the host material. Introducing sodium ions enlarges the lithium layer spacing, allowing for smooth lithium diffusion and also improved structural stability by mitigating structural transformation during the cycling process [18, 49].

Firstly, Li_2MnO_3 nanoarchitectures i.e. nanoparticles, nanoporous and bulk material with a large number of atoms in order to capture their complex structures will be simulated and their structural properties investigated. Secondly, the charging mechanism involving the concurrent removal of oxygen and lithium ions will be carried out. The removal of oxygen upon charging is motivated by the lattice oxygen loss

7

reported previously, which results in the migration of manganese into lithium layers that contribute to structural degradation during the cycling of Li_2MnO_3 [25]. Furthermore, reversible oxygen redox in the solid-state particularly can enable high energy density as it can deliver excess capacity beyond the theoretical transition metal redox capacity at high voltage [50]. Lastly, sodium ions will be introduced into the lithium sites of the generated Li_2MnO_3 nanosphere, generating structures of the form $Li_{2-x}Na_xMnO_3$ ($0 \le x \le 2$), to explore the effect of sodium doping on both the structure and electrochemical performance during the cycling process. Again, the charging process will be carried out similarly, through the simultaneous removal of lithium and oxygen to mitigate capacity fade.

Characterisations of the simulated nanoarchitectures will be based on their internal microstructures, atomic arrangements, detailed structural analysis and morphological components which evolved as a result of recrystallisation. These will be precisely interpreted utilising the radial distribution (RDF), x-ray diffraction patterns (XRD) and microstructural analysis via internal structure cutting. The diffusion coefficients will be evaluated as an electrochemical performance factor that will help diagnose the severity of oxygen loss and also the effect of sodium ions which acts as pillars in stabilizing the structure during the charging process. The ability to potentially explain the underlying relationship between atomic arrangement and electrochemical behaviours will contribute significantly to the design and performance predictions of the new generation of advanced LIBs.

1.3.1 Objectives

The objectives of the study are to :

i. employ the amorphisation and recrystallisation method to systematically synthesize the layered $Li_{2-x}Na_xMnO_3$ ($0 \le x \le 2$) nanoarchitectures (i.e. nanosphere, nanoporous with different lattice sizes) and the bulk material.

ii. investigate the host capability of $Li_{2-x}Na_xMnO_3$ nanostructures during systematic lithium extraction i.e. during the charging process of a LIB.

iii. characterize structural properties using the radial distribution functions (RDFs), simulated x-ray diffraction (XRD) patterns, and microstructural analysis to

explore the structural features and phases formed during the recrystallisation process.

iv. Investigate the diffusion coefficient at varying temperatures as an electrochemical performance contributing factor.

1.4 Hypothesis

The electrochemical performance of electrode materials can be enhanced by generating nanosized materials of different morphologies and crystallinity properties exhibiting high surface areas. Introducing sodium ions on the Li_2MnO_3 lattice enlarges the lithium layers and facilitates lithium-ion kinetics during the charging process. The diffusion coefficient of lithium ions increases with increasing temperatures.

1.4.1 Research Questions

The study will address the following issues:

i. Which Li_2MnO_3 morphology will exhibit improved electrochemical and structural properties during the charging process?

ii. Can the structural instability and poor electrochemical performance be addressed by incorporating sodium ions in the Li_2MnO_3 lithium lattice?

iii. What structural transitions take place during the cycling of both the Li_2MnO_3 and $Li_{2-x}Na_xMnO_3$ nanostructures?

iv. How is the diffusion coefficient of lithium ions affected at elevated temperatures?

1.2 Outline of the Study

Chapter 1 covers the introduction and general background of the study. The literature review including the drawbacks, strategies for improving Li_2MnO_3 cathode material and structural description are also considered along with the intentions and objectives of the study. Finally, the hypothesis and research questions are detailed.

Chapter 2 provides details on the computational and theoretical methods employed in the simulated synthesis of Li_2MnO_3 and $Li_{2-x}Na_xMnO_3$ nano-architectures. In chapter 3, the simulated synthesis and characterisation of the nanostructured Li_2MnO_3 nanoparticles, nanoporous with different cell sizes and the bulk material are discussed.

Chapter 4 unveils the effect of Li/O leaching on the nanosphere and porous nanoarchitectures and also explores their electrochemical and structural properties. The amorphisation and recrystallisation effect on Na-incorporated $Li_{2-x}Na_xMnO_3$ systems of varying Na content is outlined in chapter 5. Chapter 6 details the charging of the Na-doped nanospheres ($Li_{2-x}Na_xMnO_3$) involving the leaching of Li/O. The concluding remarks and recommendations for future studies will be outlined in chapter 7.

CHAPTER 2

Research Methodology

This chapter introduces the theoretical methods employed throughout the study. The simulation codes used for carrying out the molecular dynamics simulations along with the pair potentials that describe interactions between the Li,Mn,O,Na components will be discussed.

2.1. Computational Modeling

Computational methods play a substantial role in today's technology, they serve as an alternative and effective route to carrying out experiments that are difficult, expensive, time-consuming or impossible in the laboratory. These methods have also been characterised as reliable tools for interrogating the structural properties of nano-scaled materials due to the ability to provide atomic-level images along with the macroscopic collective behaviour comparable to experimental results [51]. There are two types of simulation techniques namely molecular dynamics (MD) and Monte Carlo (MC). The techniques are on the minimisation of the interatomic potential [52]. However, in this study, much focus will be on the time-dependent MD simulations.

2.2. Molecular Dynamics

Molecular dynamics (MD) is an n-body computational simulation technique used in studying the physical movement of atoms and molecules, particularly the identification of their structural, dynamic, and thermodynamic properties at the desired pressure and temperature conditions [53]. This technique serves as a complementary tool to conventional experiments and enables predictions of properties that are beyond experiments [54]. However, it is limited by the time and length scale. In MD a set of interacting atoms is allowed to develop gradually in time by solving the laws of motion. Molecular dynamics is based on solving the classical equations of motion numerically for a set of atoms [55]. The approach of this method starts with a model consisting of N-ions where each ion is assumed to obey Newton's laws of motion, in particular, Newton's second law of motion:

$$F_i = m_i a_i \qquad\qquad (2.1)$$

where F_i is the force acting upon the mass (m_i) and a_i is the acceleration of the system. MD uses assumptions such as Born-Oppenheimer approximation [56] where it is assumed that the nuclei are stationary.

2.2.1 Simulation Code

The DL_POLY [57] code is a general-purpose classical molecular dynamics (MD) simulation software developed at Daresbury laboratory. The code can carry out simulations of up to 30,000 with good parallel performance on up to 100 processors and can be used for force field and molecular description. Due to utilizing three-dimensional periodic boundary conditions, this is used in simulating different systems such as solids, ionic liquids, simple liquids, polar and nonpolar systems, bio- and synthetic polymers, ionic polymers, glasses solutions, simple metals and alloys. The DL_POLY requires three mandatory input files; CONTROL, FIELD and CONFIG, to assist in carrying out calculations.

2.2.2 Amorphisation and Recrystallisation

Amorphisation and recrystallisation (A+R) technique can be defined as an isa transformatory simulation in which compression or tension is applied to the system to displace atoms from an equilibrium position. The charge neutrality in this study was maintained through charge compensation, and the short-range interaction was described by the Buckingham potential [58]. When amorphisation takes place in a system, the system is heated to temperatures above its melting point in order to obtain an amorphous configuration and this results in ions that have high mobility, similar to those within a molten system in experiments [45]. The amorphous configuration is then allowed to recrystallise allowing the movement of ions into low energy configuration. Microstructural features observed experimentally i.e. grain boundaries, dislocations, surface structures point defects and morphologies evolve upon crystallisation [59]. Amorphisation and recrystallisation is thus an appropriate simulation tool to for exploring systems with complex microstructures. This technique require no proposition or generation of realistic structure that includes all the microstructural features before simulating with dynamical or static methods.

2.3. Analytical Procedure

2.3.1 Radial Distribution Functions

The radial distribution function (RDF), is a type of correlation function which describes the atomic distribution in a particular system. It determines the probability of finding a particle at a distance r away from any chosen reference particle as follows:

$$g(r) = 4\pi r^2 \rho\ (r), \qquad\qquad (2.2)$$

Where $g(r)$ represents the probability of finding an atom a distance r from another, ρ is the number density and r is the radial distance between the atoms. The RDFs serves as an effective way of describing the average structure of disordered systems like liquids. It can also be used in distinguishing between solids, liquids and gases. Figure 2.1 illustrates the radial distribution function g(r) against the radial distance r (nm) for the amantadine phases i.e. liquid, solid and gas. The gas (450K) and liquid (350K) phases depict broader and few peaks and short-range interactions due to the ability of their molecules to move dynamically. In contrast, solids have regular and periodic structures and depict multiple sharp peaks whose separation and heights are characteristic of the lattice structure [55, 60, 61].
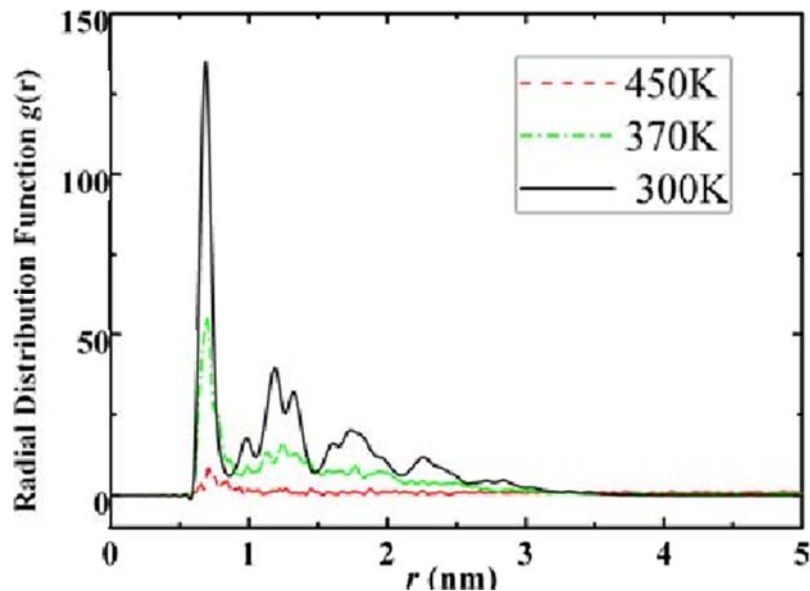
Figure 2.1: Radial distribution functions of amantadine at 450 K, 370 K and 300 K for gas, liquid and solid [62].

13

2.3.2 X-Ray Diffraction Patterns

X-ray diffraction analysis (XRD) is an analytical technique for characterizing the crystallographic structure of a material. This technique is used to explore the structural composition, to identify phases, spacing between the lattice plane, grain size, stains and the preferred orientation [63]. The keystone in understanding x-ray diffraction is the Bragg law:

$$n\lambda = 2d \sin(\theta), \hspace{3cm} (2.3)$$

where n represents an integer which defines the order of the diffraction peak, λ is the wavelength of the X-rays, d stands for the interplanar spacing responsible for the diffraction, and θ is the diffraction angle of the X-ray beam. Bragg's law correlates the wavelength of electromagnetic radiation to the diffraction angle and the lattice spacing in a crystalline sample. When x-rays are scattered from a crystalline solid, they can constructively interfere, resulting in a diffracted beam. The diffraction beam corresponds to the following conditions: The angle of incident must be equal to the angle of scattering and the distance, d is equal to an integer number of wavelengths. When the two conditions are not satisfied, destructive interference occurs. Figure 2.2 is the schematic representation of the conditions of Braggs law. The figure shows that the reflected angle θ is indeed equal to the angle of incident θ. The two waves will remain in phase provided the path length CBD is a whole number of wavelengths. But, CB and BD are equal to each other and the distance d sin θ, which satisfies Braggs law [64, 65, 66].
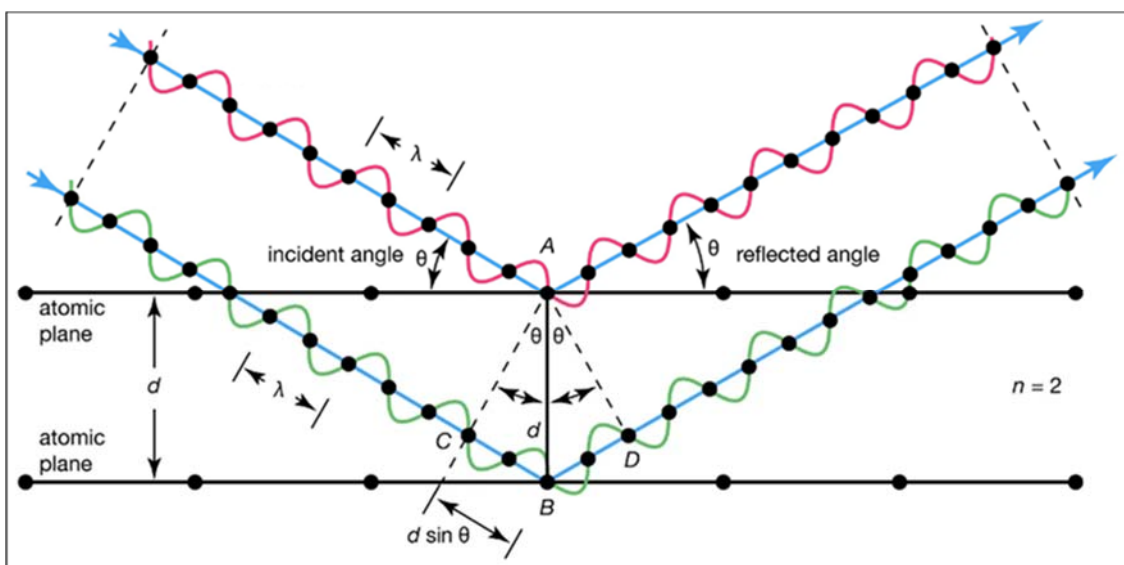
2.3.3 Diffusion Coefficient

Diffusion coefficient also known as the diffusivity, is the proportionality constant between the molar flux due to molecular diffusion and the gradient value in the concentration of species. The diffusion concept play a significant role in the kinetics of different microstructural changes that take place during the processing of metals, alloys, ceramics, semiconductors, glasses, and polymers. Typical examples are nucleation of new phases, diffusive phase transformations, precipitation and dissolution of a second phase, recrystallization, high-temperature creep, and thermal oxidation [68]. The diffusivity definition is derived from Fick's law and plays a role in various other significant equations. Fick's law states that the mass of a substance diffusing in time over a surface normal to the diffusion direction is proportional to its concentration gradient.

$$J(x,t) = D \frac{\partial C(x,t)}{\partial x} \tag{2.4}$$

The above equation is Fick's first law, where J(x,t) is the diffusion flux, it measures the amount of substance that will flow through a unit area during a unit time interval. D is the diffusion coefficient, C represents the concentration and x is the distance [69]. Diffusion in this type of molecular dynamics simulation is calculated as the slope of the graph of mean square displacement as a function of time. The Arrhenius equation can be used to simulate temperature-dependent diffusion coefficients and other thermally-induced reactions or processes and is given by:

$$D = D_0 e^{-EA/RT} \tag{2.5}$$

where D is the diffusion coefficient $(cm^2 \ s^{-1})$, D_0 is the maximal diffusion coefficient at infinite temperature $(cm^2 \ s^{-1})$, E_A is the activation energy for diffusion (J/mol), T is the absolute temperature (K) and R is the universal gas constant 8.31446 J/(mol.K). [69].

2.4. Crystallographic Defects

The arrangement of atoms in crystalline materials comprises imperfections (defects) which immensely affect the properties of materials. These defects are a result of structural deformation, rapid cooling from high temperatures or an effect of exposure to high-energy radiation. Defects are of central importance in dictating properties such

as the diffusion of atoms, mechanical stress and also the evolution of microstructures within the materials [64].

2.4.1 Point Defects

Point defects are 0-dimensional (0-D) defects that occur as a result of a missing or misplaced atom at or around a single lattice point. These particular defects can be classified into two categories, namely intrinsic and extrinsic. The intrinsic defect occurs as a result of an atom missing from a position that ought to be filled hence creating a vacancy, or when an atom occupies an interstitial site, Frenkel and Schottky's defects are two common examples of these types of defects. Frenkel defects occur as a result of an ion displaced from its lattice point and shifting to a nearby interstice. When two ions of opposite sign exit the lattice point it results in Schottky defect formation. Due to the interstitial site being small in most crystalline solids, vacancies are the most dominant point defects for solids. The presence of these vacancies allows for the diffusion of atoms from one lattice point to another. Extrinsic defects, on the other hand, occur as a result of foreign objects which are added intentionally (solute) or not intentionally (impurities) [71, 72].
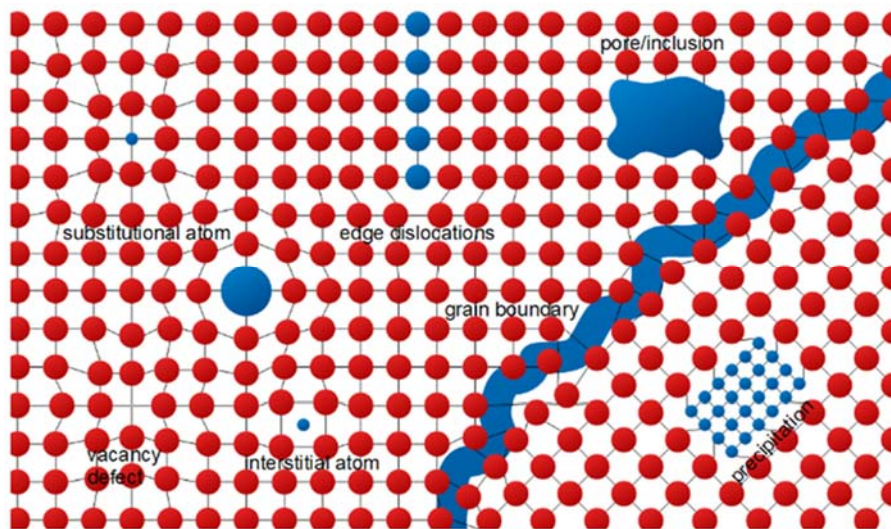
Figure 2.3: Schematic diagram depicting the microstructural features including, grain boundaries, interstitial atoms, dislocations and vacancies found in real crystalline solids [73].

2.4.2 Grain Boundaries

Grain boundaries defects are defined as the interface between two grains or crystallites in a crystalline solid. These are internal defects that are caused by the long-range orientation disruption within the solids. Grain boundaries are usually the result

of uneven growth when the solid is crystallizing and their sizes vary from 1 μm to 1 mm. Knowledge of grain boundary properties is crucial for many applications in materials science. Most grain boundaries are preferred sites for the onset of corrosion and the precipitation of new phases from the solid. However, grain boundaries disrupt the motion of dislocations through a material, so reducing crystallite size is a common way to improve the strength of a material. There are two types of grain boundaries namely low-angle grain boundaries and high-angle grain boundaries [73].

2.5. The Potential Model

Potential models are used in describing the interactions between two or more species. It affects the reliability and quality of the simulated results since it plays a significant role in determining the variation in the energy of the molecule or solid as a function of atomic co-ordinates and interactions between two or more species. Therefore, the accuracy of the calculations and results highly depends on the authenticity of the potential model.

2.5.1 Born-Model of Solids

In Born model of Solids, the energy and its derivatives can be defined as the simulation of all interactions between the atoms in the system which gives rise to the total interaction and total net force acting on each atom due to others [74]. The interaction energy is given by:

$$U_{ij} = \frac{1}{4\pi\epsilon_0} \frac{q_i q_j}{r_{ij}} + \phi(r_{ij}) . \tag{2.4}$$

With U_{ij} representing the long-range coloumbic interactions, ϵ_0 the permittivity of vacuum, q_i and q_j are the ionic charges and r_{ij} is the interatomic distance, $\phi(r_{ij})$ describes short-range interactions between ions, which includes the repulsion between the electron charge clouds and the van der Waals attraction forces.

2.5.2 Buckingham Potential

Buckingham potential is a formula that describes the Van der Walls energy $\Phi_{ij}(r)$ for the interaction of two atoms that are indirectly bonded as a function of the interatomic distance. The general form of the Buckingham potential is given by:

$$\Phi_{ij} = A_{ij} . \exp^{\frac{r_{ij}}{p_{ij}}} - \frac{c_{ij}}{r_{ij}^6} \tag{2.5}$$

where A_{ij} represents the size of the ions, ρij is the hardness and C_{ij} is the dispersion parameter and are fitted to experimental data. The first term represents the repulsive interaction between the ions while the second term represents the van der Waals attractive interaction of the ions [58].

Chapter 3

Simulated Synthesis of Nanostructured and Bulk Li_2MnO_3 Cathode Materials

3.1. Introduction

Nanomaterials are of significant importance in the development of advanced energy storage materials with high energy and power. Owing to their unique characteristics such as diffusion path reduction, better accommodation of strain during cycling and exposure to a large surface area [14], nanoscaled cathodes are being pursued. In this chapter, the amorphisation and recrystallisation technique is used in carrying out the simulated synthesis of the nanosized sphere, porous and bulk Li_2MnO_3 structures involving a large number of atoms, in a quest to investigate their electrochemical behaviour and structural characterisation, during the cycling process. This technique requires one to generate an amorphous configuration, which is then allowed to nucleate and recrystallise under material-specific conditions, resulting in the spontaneous growth of crystals, exhibiting microstructural features observed experimentally, such as grain boundaries, point defects, and dislocations [45]. Several nanostructured electrode materials such as MnO_2 [43, 45], TiO_2 [46, 47] and $LiMn_2O_4$ [75] have been previously generated via this technique. Despite the high theoretical capacity, Li_2MnO_3 cathodes suffer from structural fading and performance deterioration [76]. Studying the atomistic synthesis of these materials could shed insights into their structural and microstructural behaviour.

3.2. Method

This section unfolds the methods used in generating the Li_2MnO_3 atomistic models. The potential models that were used in describing the interactions of the Li^+, Mn^{4+}, and O^{2-} ions, the amorphisation and recrystallisation technique and the simulation codes responsible for the molecular dynamics simulations will also be discussed.

3.2.1 Potential Models

Molecular dynamics calculations presented herein are based on the Born model of ionic solids where the components in Li_2MnO_3 (Li^+, Mn^{4+}, O^{2-}) interact via short-range and long-range coupled coulombic interactions. The Li_2MnO_3 potential parameters

used for describing the Li_2MnO_3 interactions were obtained from Syle, et al. [17], and are presented in table 3.1 below. These potential parameters are capable of reproducing the lattice parameters of pyrolusite and ramsdellite polymorphs of MnO_2, to within 3% and 4%. The DL_POLY code [57] was used to perform all the molecular dynamics simulations and the fundamental input files (CONFIG, FIELD, CONTROL) were generated through the METADISE [77] code.

Table 3.1: Potential parameters obtained from a previous study [17] describing the short-range potential terms between the component ion species of Li_2MnO_3.

Interaction	A (eV)	ρ (Å)	C (eV Å^6)	Charge (e)
Li^+–Li^+	270000.0	0.1430	0.0000	0.55
Li^+-$O^{-1.1}$	30000.0	0.1542	0.0000	
Mn^{4+}- Mn^{4+}	23530.5	0.1560	16.0000	2.20
Mn^{4+}- $O^{-1.1}$	15538.2	0.1950	22.0000	
$O^{-1.1}$ - $O^{-1.1}$	11782.8	0.2340	30.2200	-1.10

3.2.2 Generation of the Li_2MnO_3 Atomistic Models

Nanosphere

The fundamental step was to generate an amorphous nanosphere configuration, which then acted as a 'building block' for the desired nanoporous and bulk atomistic models. Accordingly, a nanosphere with a radius of 40 Å was cleaved from the Li_2MnO_3 parent bulk material. In order to maintain the stoichiometry of the system, lithium and oxygen ions were randomly extracted from the outer surface of the sphere to facilitate charge neutrality. The cleaved sphere consisted of 32148 atoms i.e. 10716 Li^+ ions, 5358 Mn^{4+} ions and 16074 O^{2-} ions. The nanosphere (9.73 nm) was then placed at the centre of a simulation cell, with dimensions sufficiently high (in all directions) to prohibit neighbouring nanoparticles from, first, attracting one another and, then, agglomerating upon contact. An amorphous configuration was achieved by heating the spherical system to 1850 K [17], within the NVE (constant number of

atoms, constant volume, and constant energy) ensemble, as this temperature was sufficient to overcome the forces of attraction within the Li_2MnO_3 system. The amorphous nanoparticle was then used as a building block for generating the nanoporous and bulk architectures.

Nanoporous and Bulk

The amorphous nanosphere's cell size was then reduced in all three dimensions (3D), in order to enable the nanoparticles to agglomerate in all three spatial directions, to facilitate the formation of nanoporous structures of different cell sizes (7.30 and 7.50 nm) and the bulk model (6.78 nm), as previously attained for MnO_2 and $LiMn_2O_4$ electrodes [43, 45, 78]. These were carried out for 6 ns, with time steps set to 0.001 ps and Ewald precision of 5, while the Nosé–Hoover thermostat was used to maintain the 1850 K temperature and 50 Gpa under the NPT (constant number of atoms, constant pressure and constant temperature) ensemble. These conditions were sufficient to assist with the inter-nanocrystal attraction for ultimate agglomeration, within the time scale accessible to the MD simulations. To achieve amorphous models, MD simulations were performed at 1850K under the NVE ensemble, recrystallisation was also carried out at the same temperature under the NVT (constant number of atoms, constant volume, and constant temperature) ensemble. In order to achieve low energy models, the systems were allowed to cool systematically by gradually decreasing the temperature from 1850 K to 5 K.

A schematic illustration of the Li_2MnO_3 synthesis procedure is presented in figure 3.1 indicating (a) the spherical Li_2MnO_3 with 32148 atoms cleaved from the parent bulk, a portion is magnified in (b) revealing the atomic arrangement conforming to a monoclinic structure with C2/m symmetry, (c) is the amorphous precursor used and the building block for (d) nanoporous architectures.
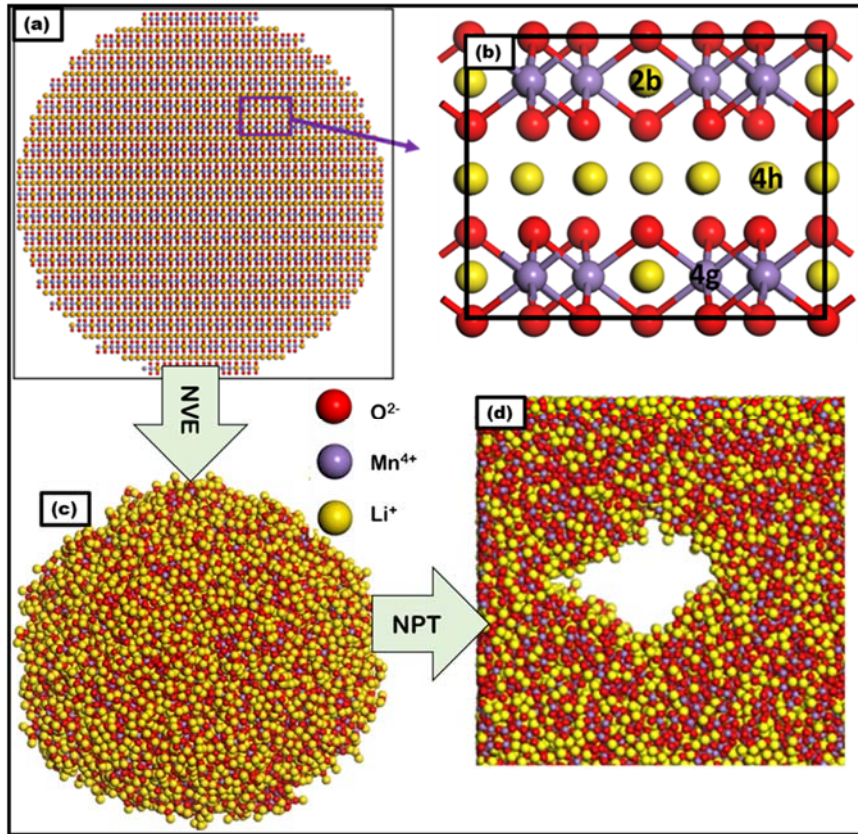
Figure 3.1: Schematic diagrams representing (a) the spherical layered Li₂MnO₃, (b) the magnified portion of (a) revealing the atomic arrangement of Li, Mn O, (c) amorphous nanosphere and (d) amorphous nanoporous configurations.

3.3. Results

3.3.1 Total Energy

Figure 3.2 presents the total energy for the Li_2MnO_3 nanosphere, calculated at a temperature range of 1000 to 1900 K to determine the temperature at which phase transition occurs. In (a), the total energy increases linearly as the temperature of the system increases. A magnified portion of (a), is illustrated in (b), showing points from 1800 to 1900 K. From the magnified portion, a plateau at around 1845 K is observed, suggesting the transformation from solid to molten phase. The graph retains its linear trend at temperatures above 1845 K.
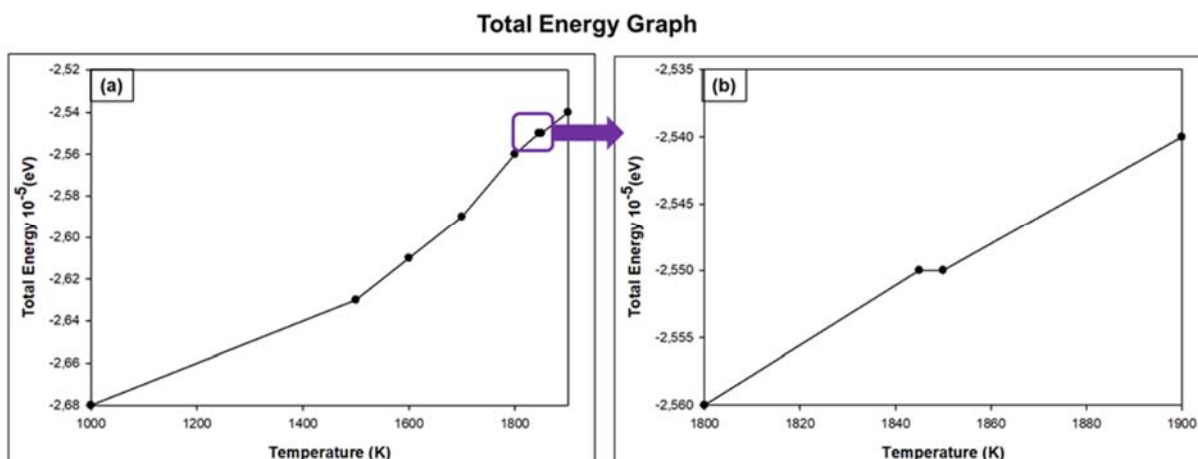
Total Energy Graph

Figure 3.2: Total energy graph for the Li₂MnO₃ nanosphere at (a) 1000-1900 K and (b) magnified portion of (a) from 1800-1900 K revealing phase transition from crystalline to amorphous state at ~1845 K.

3.3.2 Radial Distribution Functions (RDFs)

The snapshots representing the spherical Li₂MnO₃ nanocluster with corresponding radial distribution functions at 1000 K, 1700 K, 1800 K, 1845 K, 1850 K and 1900K, to verify the amorphisation temperature are illustrated in figure 3.3 below. These RDFs were plotted over a radial distance of 10 Å for the Mn-O, Mn-Mn and O-O pair distributions with the first peak indicating the interatomic bond length between the reference atom and the first nearest neighbouring atom in all pairs.

At 1000 K, the system is in a crystalline form with lithium, manganese and oxygen ions well-arranged as supported by the evident patterns on the Li₂MnO₃ snapshot. Moreover, multiple sharp peaks are observed for all the Mn-O, Mn-Mn and O-O pairs indicating strong bonds with a high possibility of locating the nearest neighbouring atom within a 10 Å radial distance. As the temperature increase, the number of sharp peaks gradually decreases and patterns start fading indicating the minimal possibility of locating the nearest neighbouring atom. A slight change in the arrangement of atoms at 1800 K is observed, suggesting that the structure is partially amorphous with some peaks starting to broaden. At temperatures above 1800 K, few broad peaks are observed with only peaks from 2-4 Å being well defined, strongly suggesting the transformation from crystalline to amorphous phase. The transition is also observed in the snapshots as the temperature increase. The Mn-O pair distribution first peak

23

around 1.9 Å remains strong at all temperatures, with a slight decrease in intensity as the temperature was increased.
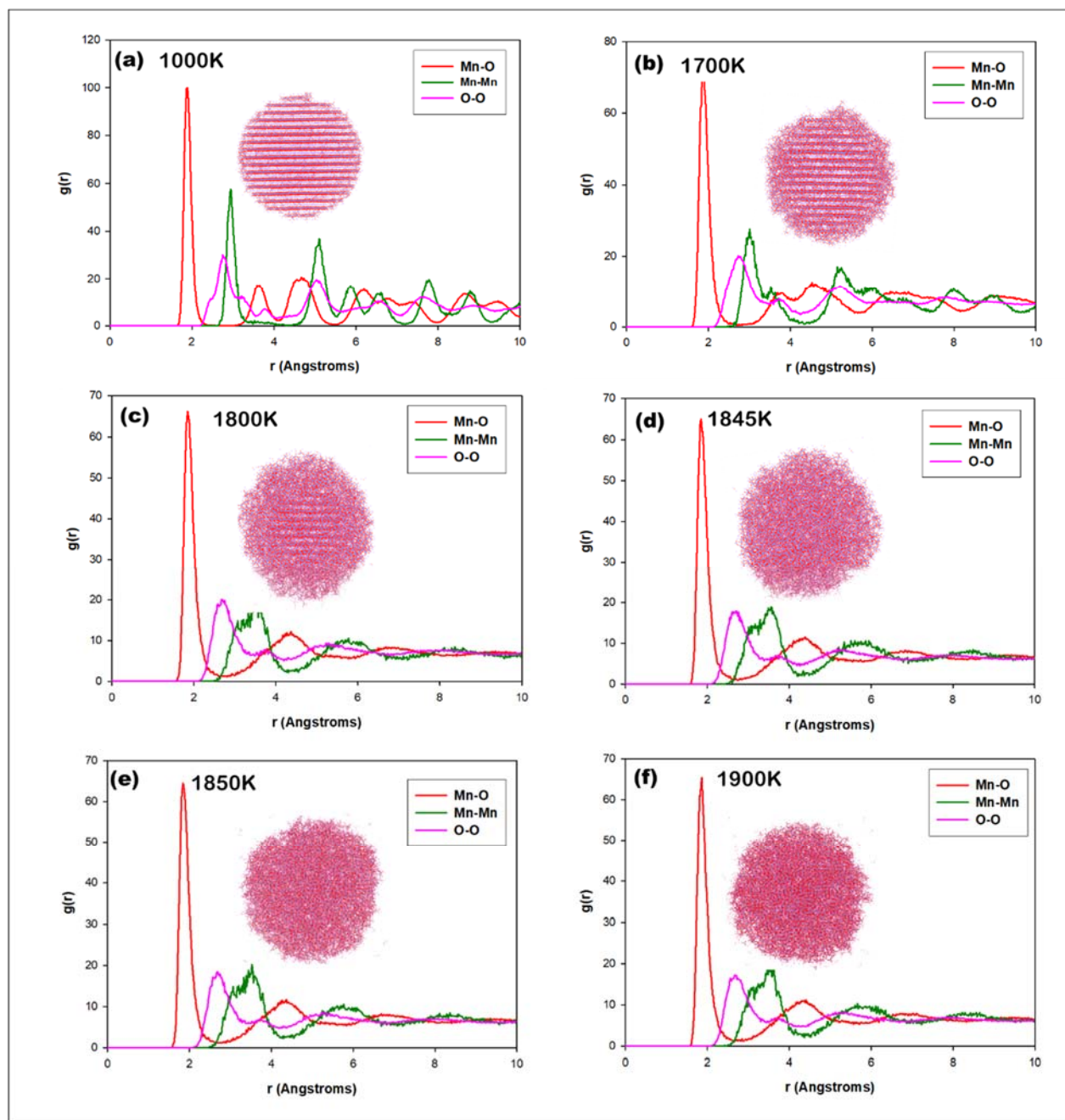
Figure 3.3: Radial distribution functions of the Li_2MnO_3 nanosphere with corresponding structures for the Mn-O, Mn-Mn and O-O pair distribution at (a) 1000 K, (b) 1700 K, (c) 1800 K, (d) 1845 K, 1850 K and 1900 K during amorphisation calculations.

Figure 3.4 illustrates the RDFs associated with the Mn-Mn (red), O-O (green) and Mn-O (pink) interactions for the nanosphere configuration, calculated at 1850 K. The amorphous configuration is depicted in (a), with the first peaks at approximately 1.9,

2.5 and 3.5 Å for the Mn-O, O-O and Mn-Mn interactions with the Mn-O exhibiting the highest g(r) value. The peaks at radial distances beyond 5 Å are broader, suggesting the disordering of the atoms and minimal possibility of locating the nearest neighbouring atom within the radial distance.

The recrystallised RDFs depicted in (b), reveal frequent sharp peaks with increased intensity for all three interactions i.e., Mn-Mn (red), O-O (green) and Mn-O (pink) indicating long-range ordering of the atoms. This increment in the number of sharp peaks is an indicative measure of the recrystallisation of the nanosphere structure.
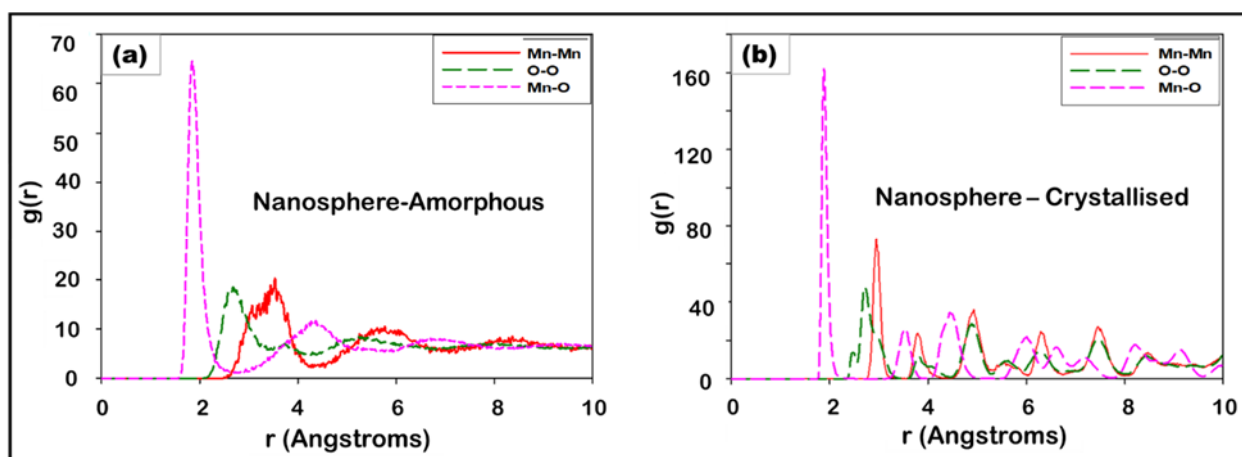
Figure 3.4: Radial distribution plots for the Mn-Mn (red), O-O (green) and Mn-O (pink) Li$_2$MnO$_3$ amorphous (a) and recrystallised (b) nanosphere at 1850 K.

RDFs for the nanoporous and bulk structures are illustrated in figure 3.5, showing the Mn-Mn (red), O-O (green) and Mn-O (pink) pair distributions. The amorphous pair distribution plots for the nanoporous (a) and bulk (c) systems depict broader peaks that are associated with weak bonds and minimal possibility of locating the nearest neighbouring atom in relation to the reference atom. Recrystallisation was confirmed by the narrowing of peaks with elevated g(r) values indicating that the atoms are at their lowest energy and have a high possibility of locating the nearest neighbouring atom within the radial distance (r).
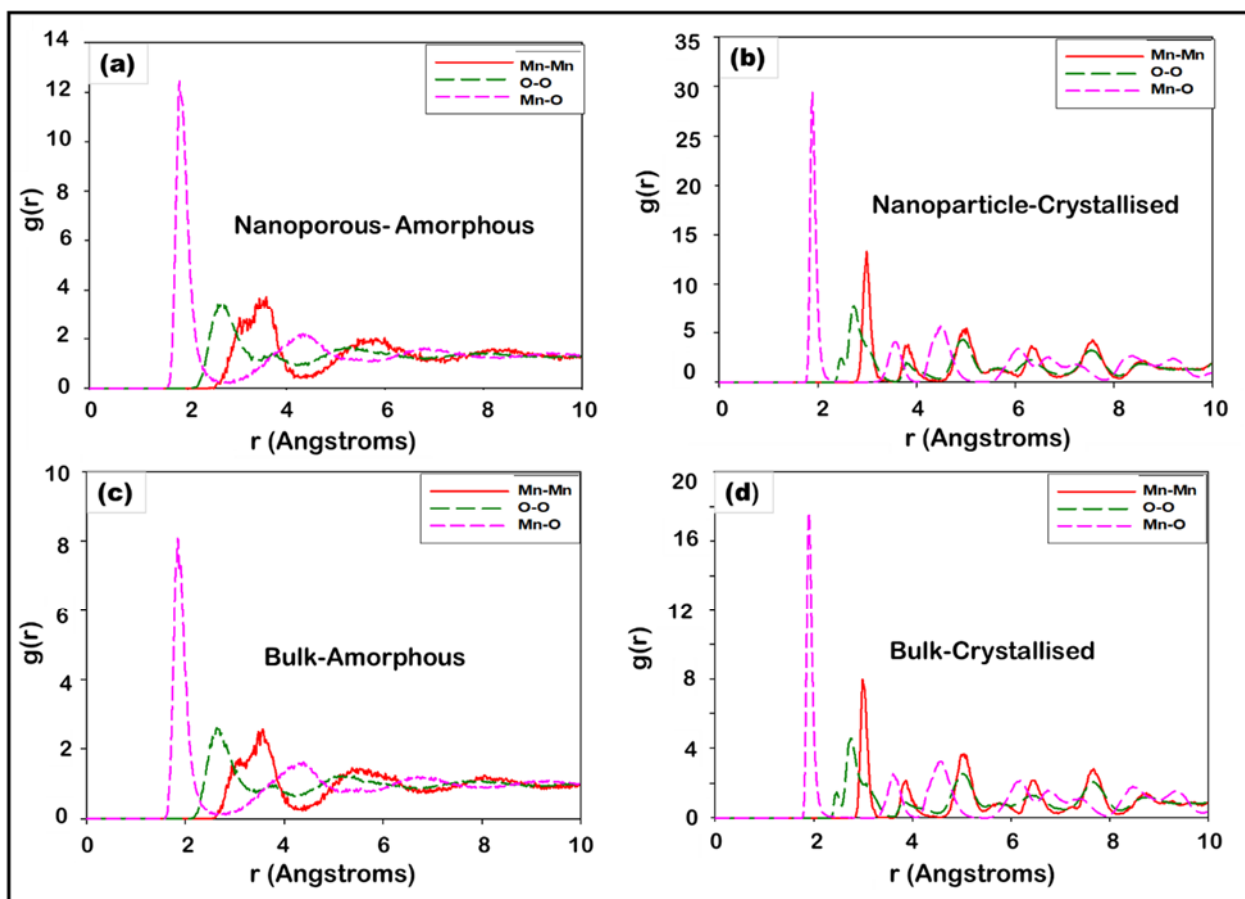
Figure 3.5: Radial distribution functions for the Li₂MnO₃ nanoporous (a-b) and bulk (c-d) during amorphisation and recrystallisation performed at 1850 K.

3.3.3 X-Ray Diffraction Patterns (XRDs)

Diffraction peaks for the simulated Li_2MnO_3 nanostructures are superimposed in figure 3.6, where the nanosphere, nanoporous and bulk configurations are indicated by red, green and pink traces respectively. The nanosphere depicts broader peaks as compared to the nanoporous and bulk, with less shifting of the peaks at 2Θ~38 and 68º to the right. The emergence of peaks associated with the Li/Mn ordering in the transition metal layers is more prominent for the nanosphere. The partial shift to the right is observed for all structures, but the sphere shifts further to the right, suggesting more mixed layers in the nanosphere structure.
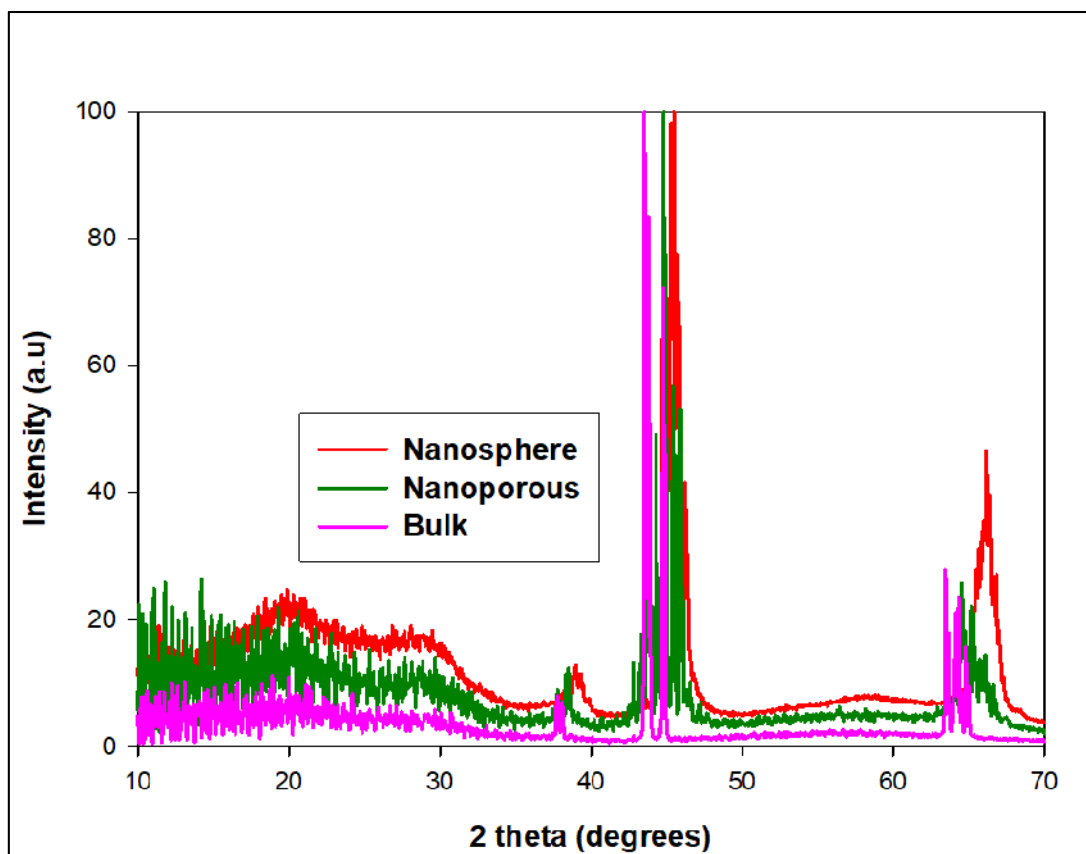
Figure 3.6: Comparison between the simulated Li₂MnO₃ X-ray diffraction patterns for the nanosphere (red), nanoporous (green) and bulk (pink).

To validate the simulated Li_2MnO_3 model systems, XRDs were calculated and compared with the ones from the literature. Figure 3.7 (a) illustrates XRDs for the simulated Li_2MnO_3 nanosphere (this work), superimposed with (b) experimental Li_2MnO_3 bulk (black trace), simulated nano-Li_2MnO_3 (blue trace) [17] and bulk Li_2MnO_3 [33]. Our model reveals characteristic peaks conforming to the C2/m layered structure, all the peaks are comparable to the ones obtained experimentally. There is a shoulder peak observed at lower angles (2Θ~18-35⁰) accompanied by a partial shift to the right of the 2Θ~38⁰ peak (red arrow) as attained in the previous study by Syle et al [17]. The peaks around 2Θ~65-70⁰ merge and become one broad peak as a result of cation mixing [4].
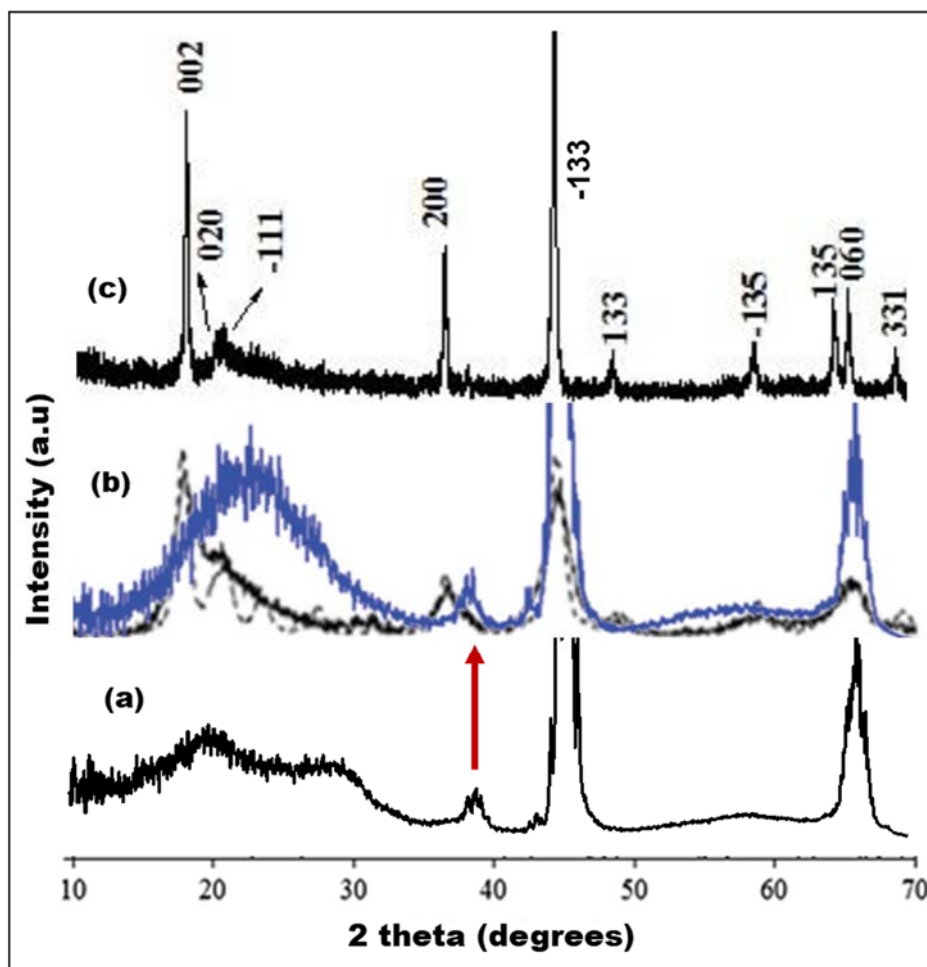
Figure 3.7: XRD patterns for (a) the simulated Li₂MnO₃ nanosphere (this work), compared with (b) experimental Li₂MnO₃ bulk (black trace), simulated nano-Li₂MnO₃ (blue trace) [20] and (c) experimental Li₂MnO₃ [36].

Figure 3.8 below depicts XRD patterns for (a) the simulated Li_2MnO_3 nanoporous with a cell size of 75 Å, comparable with (b) the experimental Li_2MnO_3 bulk (black trace), simulated nano-Li_2MnO_3 (blue trace) [17] and (c) bulk Li_2MnO_3 [33]. In comparison to the bulk Li_2MnO_3 in (c), the nanosized simulated Li_2MnO_3 exhibits wider and less intensive peaks with some peaks (133, 135 and 331) not displayed, this may be caused by the size difference and stress in the materials. Again, the nanoporous conforms to the layered Li_2MnO_3 C2/m. The peaks related to the Li/Mn ordering in the transition layers (2Θ~18-35º) are deflated. A partial shift to the right of peak 2Θ~38º is also observed, however, the peak is not as broad as the one for the nanosphere above. We also observe the narrowing and spitting of the peak at 2Θ~45º and 65º.

28
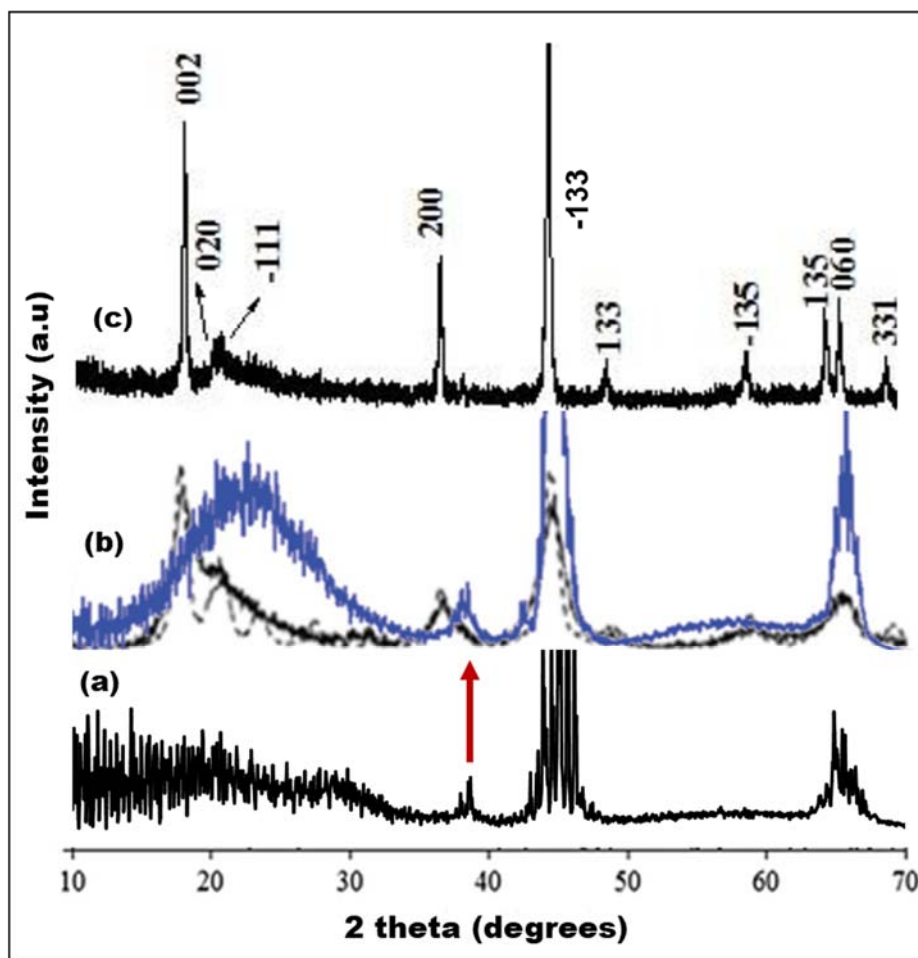
Figure 3.8: XRD patterns for (a) the simulated Li₂MnO₃ nanoporous (this work), compared with (b) experimental Li₂MnO₃ bulk (black trace), simulated nano-Li₂MnO₃ (blue trace) [17] and (c) experimental Li₂MnO₃ [33].

The XRDs representing (a) the simulated Li_2MnO_3 bulk compared with the XRDs from previous work (b) experimental Li_2MnO_3 bulk (black trace), simulated nano-Li_2MnO_3 (blue trace) [17] and bulk Li_2MnO_3 [33] are shown in figure 3.9 below. At lower angles i.e. 2Θ~18-35º, the peaks have reduced in intensity. The partial shifting of the 2Θ~38º peak is still observed along with the splitting of the peaks at 2Θ~45º into a doublet and at 65º into multiple peaks.
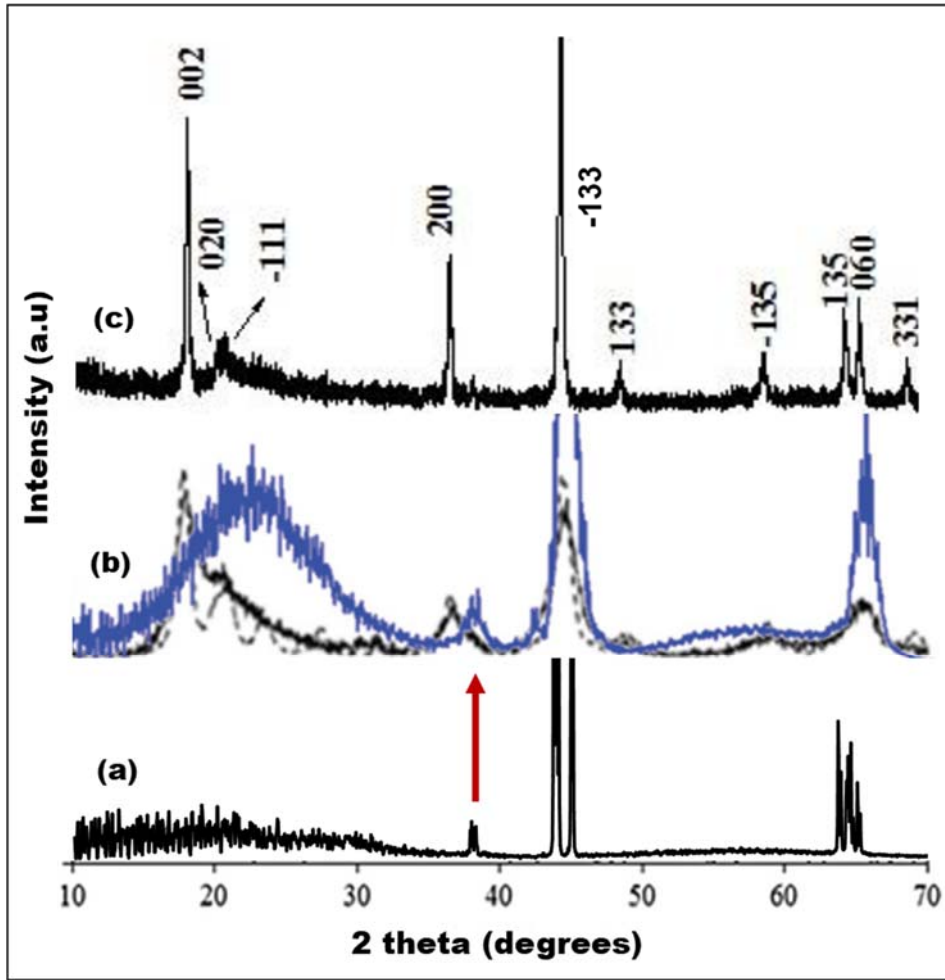
Figure 3.9: XRD patterns for (a) the simulated Li₂MnO₃ bulk (this work), compared with (b) experimental Li₂MnO₃ bulk (black trace), simulated nano-Li₂MnO₃ (blue trace) [17] and (c) experimental Li₂MnO₃ [33].

3.3.4 Microstructures

In order to explore the crystallographic features that evolved during the recrystallisation of the generated Li_2MnO_3 models, the models were cut through into segments, to better view their atomic arrangement. Accordingly, figure 3.10 illustrates a slice cut through the Li_2MnO_3 nanosphere, where a portion is magnified in (b), showing the Li_2MnO_3 phase. The magnified portion reveals the presence of vacancies (orange circles) and cation mixing (green squares). The atomic arrangement of the magnified portion conforms to a distorted Li_2MnO_3 phase comparable to the perfect model presented in (c). Our model also compares very well with the experimental SAED patterns [25] which reveal the Mn ions (bright) and Li arrangements.
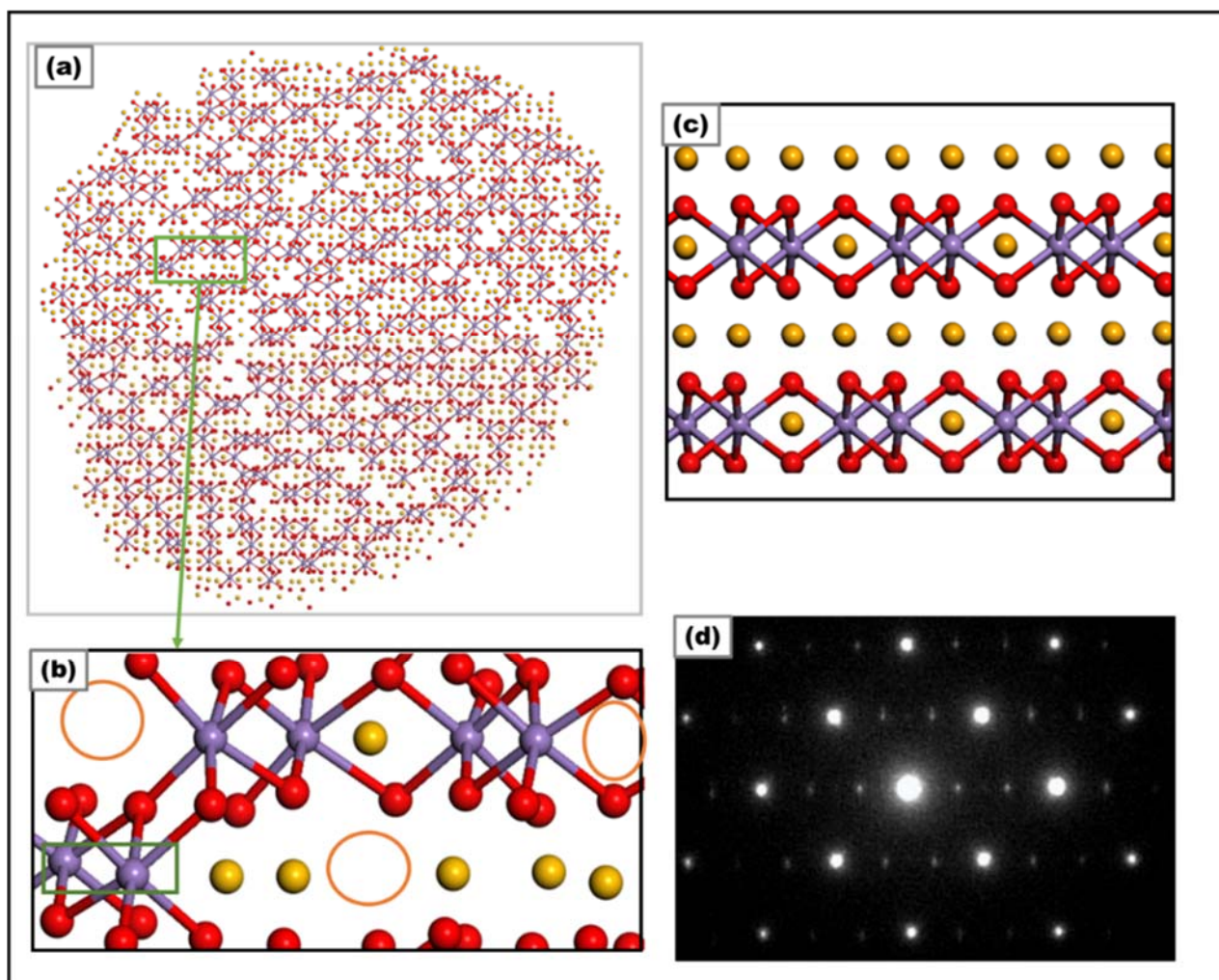
Figure 3.10: Schematic presentation of (a) slice cut through simulated Li₂MnO₃ nanosphere, (b) magnified section of (a) comparable with (c) slice cut through Li₂MnO₃ perfect model and (d) Li₂MnO₃ SAED experimental patterns [25].

Molecular graphics representing the Li_2MnO_3 nanoporous 75 Å are depicted in figure 3.11(i), in which (a) exhibits no grain boundaries implying that the model crystallised into a single-grained crystal. A portion from (a) was magnified to better view the migration of Mn ions (enclosed by the green circles) to the tetrahedral sites, blocking Li-ions pathways. The cut-through Li_2MnO_3 nanoporous 75 Å, confirms the mixing of layers upon recrystallisation, with a magnified portion (b) showing the Li_2MnO_3 accompanied by cation mixing, as indicated by the pink circles. Another enlarged portion (d) depicts a high level of Li, Mn and O vacancies within the nanoporous structure. The slice cut through the perfect model of Li_2MnO_3 is illustrated in (c) for comparison.
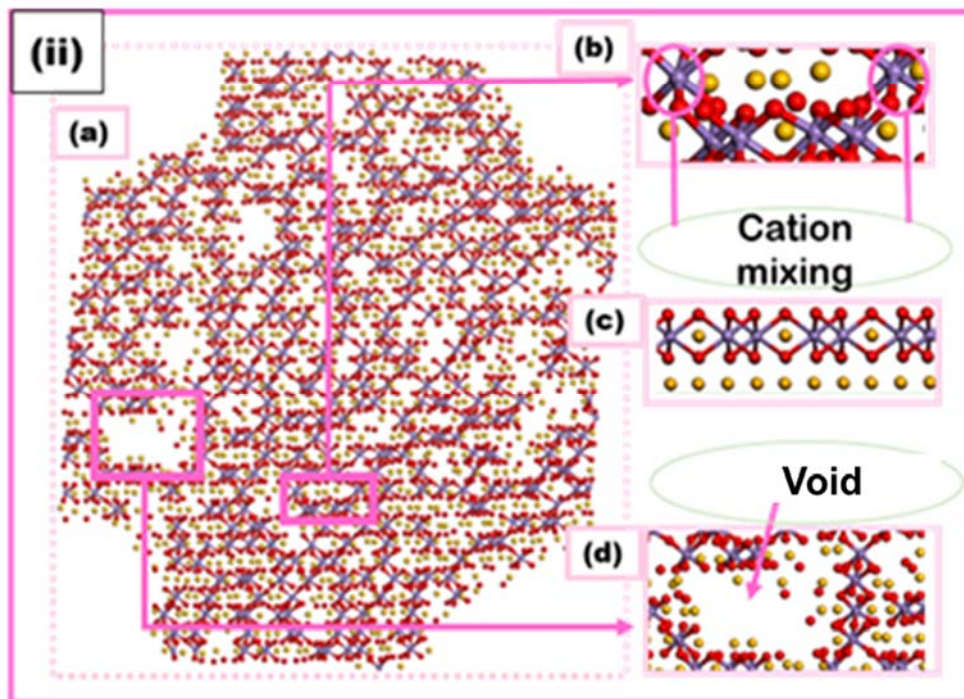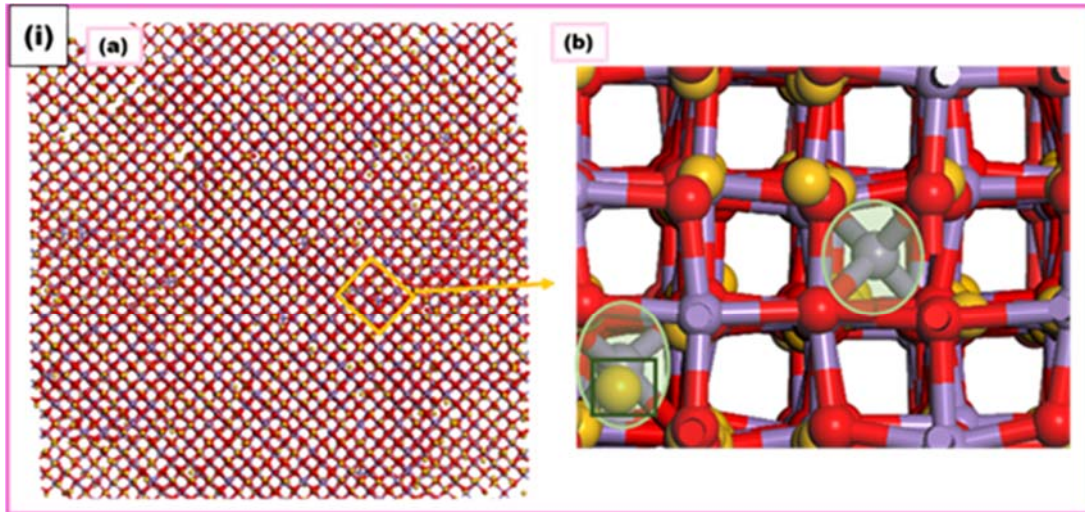
Figure 3.11: (i)(a) Simulated Li₂MnO₃ nanoporous 75 (b) magnified potion revealing manganese ions in tunnels. (ii)(a) A slice cut through Li₂MnO₃ nanoporous 75, (b) magnified portion of (a), comparable with (c) Li₂MnO₃ perfect model, (d) magnified portion of (a) revealing a void.

Figure 3.12 (a), illustrates the slice cut-through Li_2MnO_3 bulk material, with (b) a magnified portion of (a) revealing a distorted Li_2MnO_3 phase comprising Li, Mn and O vacancies along with cation mixing. Despite the presence of defects in the simulated bulk model as a result of inconsistency in the Li-Mn-O atom arrangements, the system still conforms to the Li_2MnO_3 structure comparable to the Li_2MnO_3 perfect model depicted in (d). In order to compare the simulated model with the experimental, the

Li$_2$MnO$_3$ SAED patterns [25] are presented in (e) and compared very well with simulated structures. The arrangement of the atoms in the simulated bulk is shown in (d), revealing inconsistency in the Li and TM/Li layers.
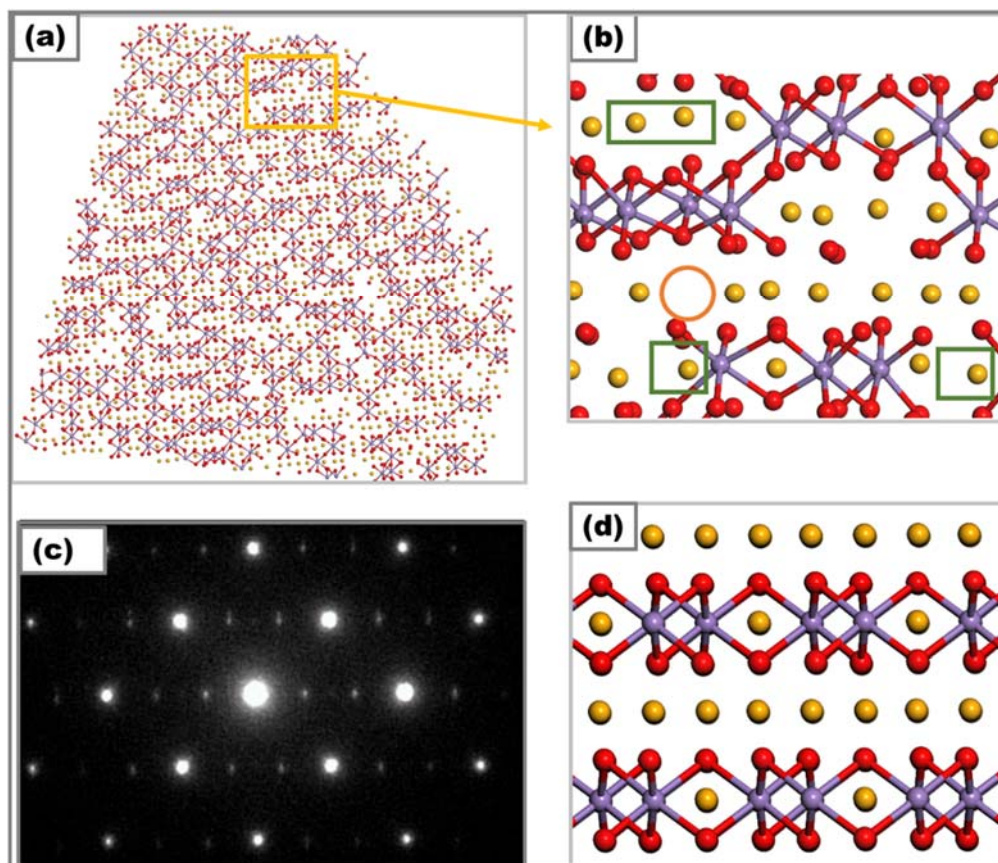
Figure 3.12: Li$_2$MnO$_3$ bulk (a) slice cut through, (b) magnified portion of (a), (c) Li$_2$MnO$_3$ perfect model, (d) magnified portion of (a) with deleted bonds to better view the Li$_2$MnO$_3$ layers and (e) is the SAED experimental patterns for comparison [25].

3.3.5 Diffusion Coefficient

The diffusion coefficient of Li-ions as a function of temperature is illustrated in figure 3.13, indicating the Li$_2$MnO$_3$ systems i.e nanosphere (black trace), nanoporous 75 (red trace), nanoporous 73 (blue trace) and the bulk material (pink trace). Li-ions in the nanosphere depict the highest mobility in comparison to the nanoporous and bulk configurations. Accordingly, at 100 K, the nanosphere starts with a diffusion coefficient value of approximately 0.2 nm^2.s^{-1}, increases to 0.58 nm^2.s^{-1} and decreases to 0.44 nm^2.s^{-1} at 300 K, the graph then rapidly increases to 1.42 nm^2.s^{-1} at 500 K and reduce

to 0.62 nm^2.s^{-1} at 600 K, then exponentially increases until its maximum value at 1000 K. Though the nanosphere exhibit excellent Li-ion mobility, the graph trend alternate, which may be attributed to the shape of the sphere and also the increased level of defects within the structure. Figure 3.13 (b) has been magnified from (a) to better view the Li-ion diffusion from 500-1000 K, and it can be noted that the nanoporous 73 Å diffuses second to the nanosphere, followed by the nanoporous 75 Å and lastly the bulk material. The nanoporous 75 Å, nanoporous 73 Å and bulk material start diffusing at around 500 K and gradually increase until 1000 K.
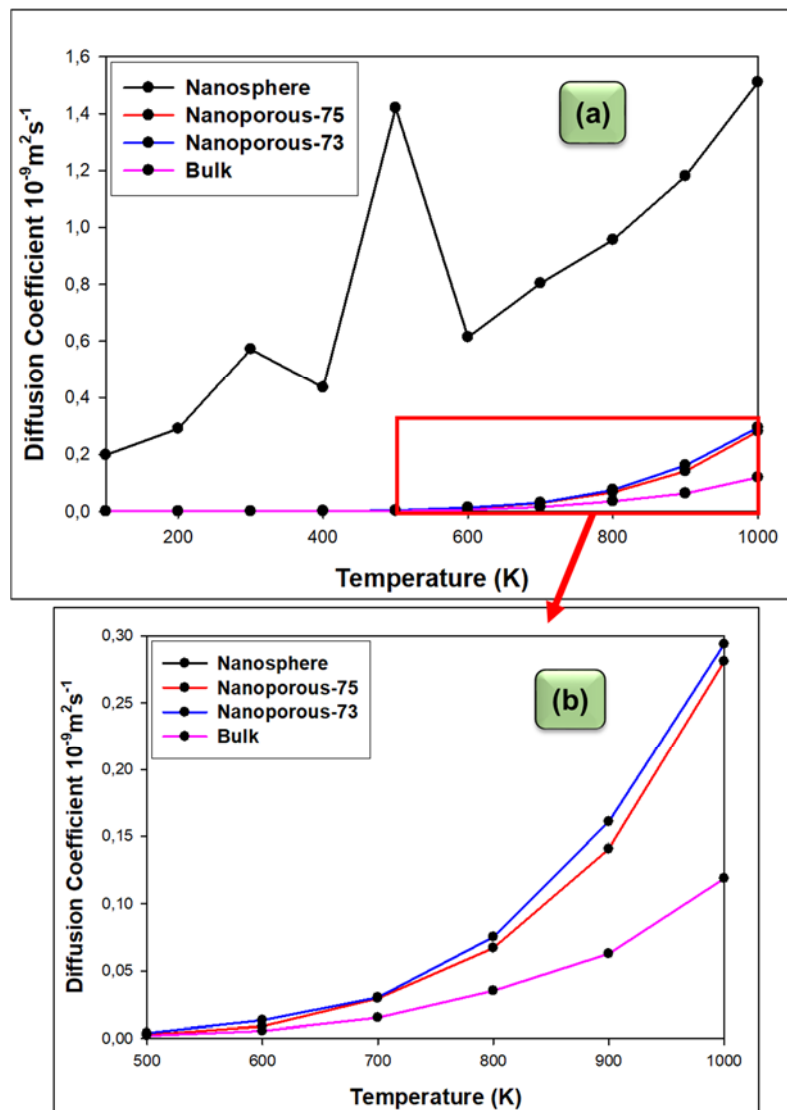
Figure 3.13: (a) Diffusion coefficient graphs for lithium ions against temperature for the Li$_2$MnO$_3$ nanosphere (black), nanoporous 75 (red), nanoporous 73 (blue), and the bulk material (pink). (b) A magnified portion from (a) captured from 500 to 1000 K.

3.4. Summary

The amorphisation and recrystallisation process was used in generating atomistic models of the complex layered Li_2MnO_3. Specifically, the simulated synthesis of Li_2MnO_3 nanosphere, nanoporous and bulk architectures with a significant number of atoms (32148) was carried out at 1850 K, employing the DL_POLY code. The amorphisation temperature was guided by previous studies and verified by the RDFs calculated at different temperatures which depicted phase transformation from crystalline to molten at temperatures above 1800 K. Moreover, the total energy against temperature graph also revealed the melting temperature to be around 1845 K. Recrystallisation of the generated models was confirmed by the presence of sharp peaks observed on the RDFs calculated over a radial distance of 10 Angstroms. All the generated models crystallised into single-grained materials with no formation of new phases. It was observed from the microstructures that the $Li_{1/3}Mn_{2/3}$ cationic planes are never perfectly stacked along the c-axis as they should be when the structure is described using the C2/m space group [39]. Thus resulting structures showed no lithium-only layers within the structures but revealed a high level of defects including Li, O and Mn vacancies along with cationic mixing. Simulated XRDs depicted peak broadening at lower angles, associated with the change in the ordering of Li/Mn in the transitional metal layers. The partial shifting of the peak at 2Θ~38º to the right is due to the cation mixing of Li and Mn [17]. The simulated nanosphere as compared to the nanoporous and bulk depicts broader peaks, with most of the peaks merging to form a single peak. This broadening of peaks may be attributed to a large amount of stacking faults in the structures as observed on the microstructures.

Chapter 4

The Effect of Lithium and Oxygen Extraction from Li_2MnO_3 Nanoarchitectures

4.1. Introduction

Capacity degradation and voltage fade of Li_2MnO_3 during cycling are the limiting factors for its practical use as a high-capacity lithium-ion battery cathode [11]. These poor cycling behaviours are a result of complex phenomena such as irreversible oxygen loss and phase transformation due to lattice reconstruction [10, 12]. Significantly, the role of oxygen in the cycling process of Li_2MnO_3 is one factor that has received research interest recently. Oxygen release upon cycling can prompt thermal runaway, and also, result in gas formation which put the battery at risk of deformation and performance degradation. Again, it was established that charge compensation in Li_2MnO_3 is maintained by partial oxidation of oxygen and oxygen loss during the first cycle [79]. Despite substantial research being made in enhancing this material, there are a lot of uncertainties regarding the structural and electrochemical features displayed by the layered Li_2MnO_3 [13]. This chapter reports on the effect of the simultaneous removal of oxygen lithium (Li/O) on the structural transitions taking place during the charging of Li_2MnO_3.

4.2. Method

The charging process was carried out for the nanosphere and nanoporous systems generated from the previous chapter. Accordingly, lithium and oxygen ions were randomly extracted from the outer surface of the amorphous configurations, resulting in the generation of models with varying Li/O content. Charge neutrality was maintained by reducing the oxygen ions from $O^{-1.10}$ to $O^{-1.28}$. This facilitated for four systems with different lithium and oxygen contents i.e. $Li_{1.75}MnO_{2.75}$, $Li_{1.50}MnO_{2.50}$, $Li_{1.25}MnO_{2.25}$ and $Li_{1.00}MnO_{2.00}$. Table 4.1 indicates the number of lithium and oxygen ions that were removed from the outer surface and also the total number of ions in each system. Since the extraction of Li/O was not done sequentially, the resulting nanoparticle structures displayed a huge number of atoms scattered at the surface. To surpass this, a short simulation (1000 steps) had to be run at 1850 K under the NVE ensemble to facilitate the relaxation of the perturbed ions. Molecular dynamics

simulations under the NPT ensemble were performed for the four nanoparticle systems to generate the nanoporous structures associated with each concentration. To recrystallise the systems, MD calculations with the NVT ensemble were carried out for five million steps at 1850 K. The pressure was set to zero with the cut-off of 10 Å and Ewald precision of 2. The systems were then allowed to cool systematically by reducing the temperature gradually from 1850 to 5 K allowing for the systems to be at their lowest energy.

Table 4.1: $Li_{2-x}MnO_{3-x}$ systems indicating the number of oxygen and manganese ions that were extracted from the pristine Li_2MnO_3 system which had 32148 atoms i.e. 10716 Li^+ ions, 5358 Mn^{4+} ions and 16074 O^{2-} ions.

Li-Mn-O concentrations	Total # of lithium ions extracted.	Total # of oxygen ions extracted.	Total # of atoms In the system
$Li_{1.0}MnO_{2.0}$	5358	5358	21432
$Li_{1.25}MnO_{2.25}$	4018	4018	24112
$Li_{1.50}MnO_{2.50}$	2679	2679	26789
$Li_{1.75}MnO_{2.75}$	1339	1339	29470

4.3. Results

4.3.1 Molecular Graphics during the Charging of $Li_{2-x}MnO_{3-x}$

Figure 4.1 illustrates molecular graphics for the nanosphere (a-e), nanoporous 75 (f-j), and nanoporous 73 (k-o) during the leaching of lithium and oxygen ions. For the nanosphere system, the pristine Li_2MnO_3 recrystallised into a single-grain crystal with a distorted rock-salt structure similar to the nanoparticle simulated at 1845 K in a previous study [17]. The presence of patterns suggests that the systems are in their crystalline phases. For the $Li_{1.75}MnO_{2.75}$, grain boundaries (yellow dotted line) evolved as a result of crystallographic defects that disrupt the regular Li_2MnO_3 lattice arrangement. The grain boundaries increased with decreasing Li/O content and the $Li_{1.00}MnO_{2.00}$ revealed severe defects, evidenced by the loss of patterns.

For the nanoporous with lattice size 75 Å, the pore size increased along with grain boundaries as the Li/O concentration was decreased. The pristine Li_2MnO_3 nanoporous 73 Å (k) pore is blocked on one side upon crystallisation, however, during the removal of Li/O, the pore opens from all sides of the model. Again, the pore size increases as charging progress, with the $Li_{1.00}MnO_{2.00}$ showing considerable lithium ions located within the pore.
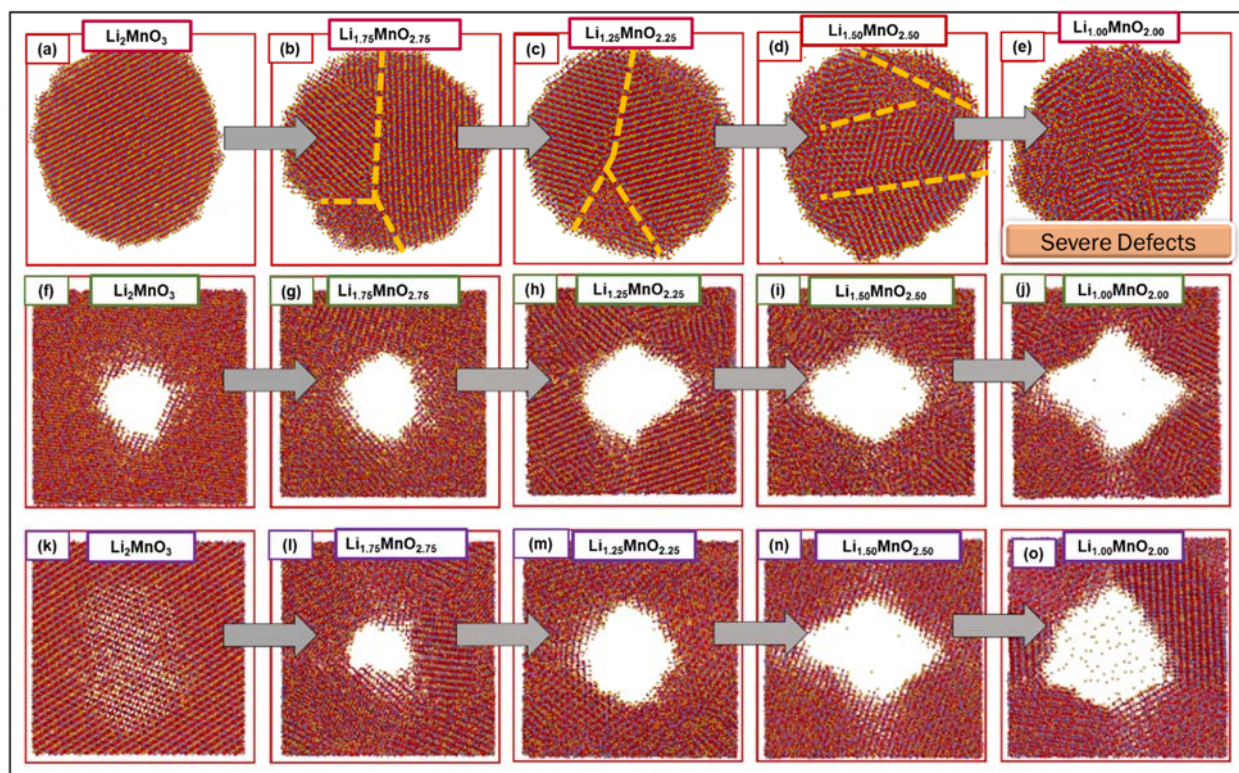
Figure 4.1: Snapshots representing the crystallised $Li_{2-x}MnO_{3-x}$ (a-e) nanosphere, (f-g) nanoporous 75 Å and (k-o) nanoporous 73 Å with varying Li/O concentrations.

4.3.2 Radial Distribution Functions (RDFs)

The RDFs for the Mn-O interactions are illustrated in figure 4.2 below to better view the distribution of atoms on the amorphous and recrystallised $Li_{2-x}MnO_{3-x}$ systems. In (a) the amorphous nanoporous for $Li_{1.75}MnO_{2.75}$ (red), $Li_{1.50}MnO_{2.50}$ (blue), $Li_{1.25}MnO_{2.25}$ (pink) and $Li_{1.00}MnO_{2.00}$ (green) systems reveal the first peak at 1.9 Å which represents the Mn-O bond length. The peaks from 6 -10 Å are broader indicating weak bonds and minimal possibility of locating the nearest neighbouring atom within the radial distance r as a result of scattered atoms. In (b) the recrystallised systems show an increased number of peaks due to strong bonds and a high probability of

locating the nearest neighbouring atom within the radial distance. The sharp peaks are an indication that the systems are in their crystalline state.

The amorphous nanoporous depicted in (c) also shows the presence of broader peaks with the probability $g(r)$ approaching one at longer radial distances. The peaks beyond 5 Å are broader with minimal possibility of locating the nearest neighbouring atom within the radial distance. In (d) the peaks have increased in quantity with the $Li_{1.00}MnO_{2.00}$ concentration revealing the highest $g(r)$ value compared to the other concentrations.
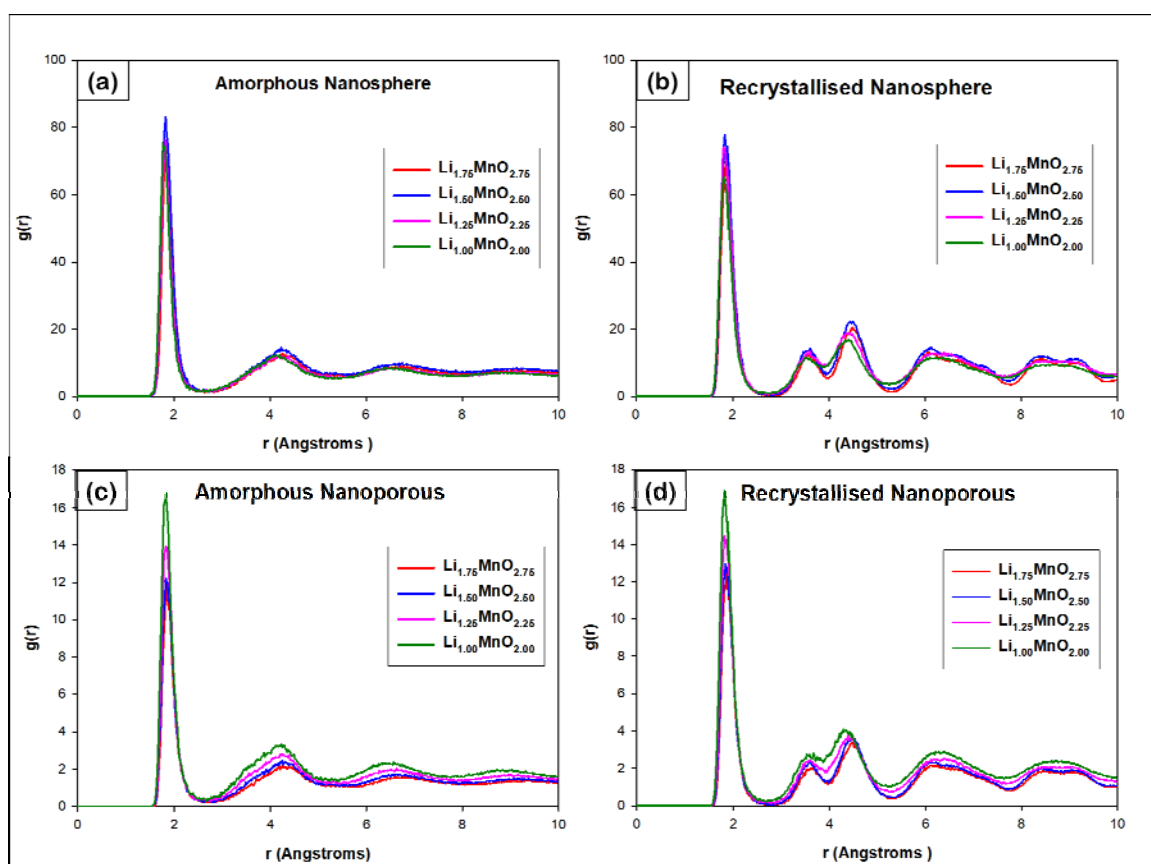
Figure 4.2: Mn-O pair distribution for (a) amorphous nanosphere, (b) recrystallised nanosphere, (c) amorphous nanoporous 75 Å and (d) recrystallised nanoporous 75 Å as an indicative measure for the amorphisation and recrystallisation state of the structures, where $Li_{1.75}MnO_{2.75}$, $Li_{1.50}MnO_{2.50}$, $Li_{1.25}MnO_{2.25}$ and $Li_{1.00}MnO_{2.00}$ concentrations are presented by red, blue, pink and green.

4.3.3 X-Ray Diffraction Patterns

The diffraction patterns for the Li_2MnO_3 systems were calculated during the simulated charge process and compared with the ones from the literature to consider whether structural features corresponding to that in known metal oxides may have evolved. Figure 4.3 (a) illustrates the diffraction peaks for the simulated $Li_{2-x}MnO_{3-x}$ nanoparticle systems with different concentrations, superimposed with experiments (b) Li_2MnO_3 [80], (c) $LiMn_2O_4$ [81] (d) $LiMnO_2$ and (e) MnO_3 [82] for comparison. The simulated nanoparticles depict a broadening of peaks indicating that the charging mechanism results in highly distorted structures [10]. There is an emerging shoulder peak around $2\Theta\sim18\text{-}25^o$ associated with both the Li_2MnO_3 and MnO_3 peaks. This shoulder peak monotonously increases with a decrease in Li/O content. The peak emerging at $2\Theta\sim29^o$ indicates the increasing number of tetrahedral sites that are occupied by the Mn ions. Again, peaks at $2\Theta\sim37^o$ and 48° increase while the peak at $2\Theta\sim68^o$ broadens.

Figure 4.4 displays the diffraction patterns for the simulated nanoporous 75 Å (a) Li_2MnO_3, (b) $Li_{1.75}MnO_{2.75}$, (c) $Li_{1.50}MnO_{2.50}$, (d) $Li_{1.25}MnO_{2.25}$ and (e) $Li_{1.00}MnO_{2.00}$ systems, compared with experiments (f) Li_2MnO_3 [80], (g) $LiMn_2O_4$ [81] (h) $LiMnO_2$ and (i) MnO_3 [82]. Similarly to the nanoporous systems, emerging shoulder peaks at $2\Theta\sim18\text{-}20^o$ and $2\Theta\sim24\text{-}35^o$ are observed due to Li/O ordering in the transition metal layer [25]. Also an emerging peak at $2\Theta\sim37^o$ increases with a decrease in Li/Mn content. The multiple peaks at $2\Theta\sim47^o$ and $2\Theta\sim68^o$ merge into a broader peak that shifts to the right as the Li/O content decrease, these peaks correspond to the spinel phase. The level of peak broadening is more extreme for the $Li_{1.00}MnO_{2.00}$ concentration thus the more we extract Li/O the more grains forms within the material. The diffraction peaks for the simulated nanoporous 73 Å (a-e), superimposed with the experimental XRDs (e-f) are shown in figure 4.5 respectively. The nanoporous 73 Å systems behave differently from both the nanosphere and nanoporous 75 Å. At lower angles, a peak associated with the layered $LiMnO_2$ emerges as the Li/O content decreases, however, the peak decreases drastically at $Li_{1.25}MnO_{2.25}$ and re-emerges again at $Li_{1.00}MnO_{2.00}$. The same is observed at $2\Theta\sim37^o$ where the peak increases but decreases for the $Li_{1.00}MnO_{2.00}$ concentration. All the simulated peaks show peak broadening upon Li/O extraction, but the peaks become narrow for the $Li_{1.00}MnO_{2.00}$, this concentration has also revealed fewer grain boundaries during recrystallisation.

The peak at 2Θ~47º and 2Θ~68º become broad for all concentrations however, at Li$_{1.00}$MnO$_{2.00}$ multiple peaks emerges with reduced intensity.
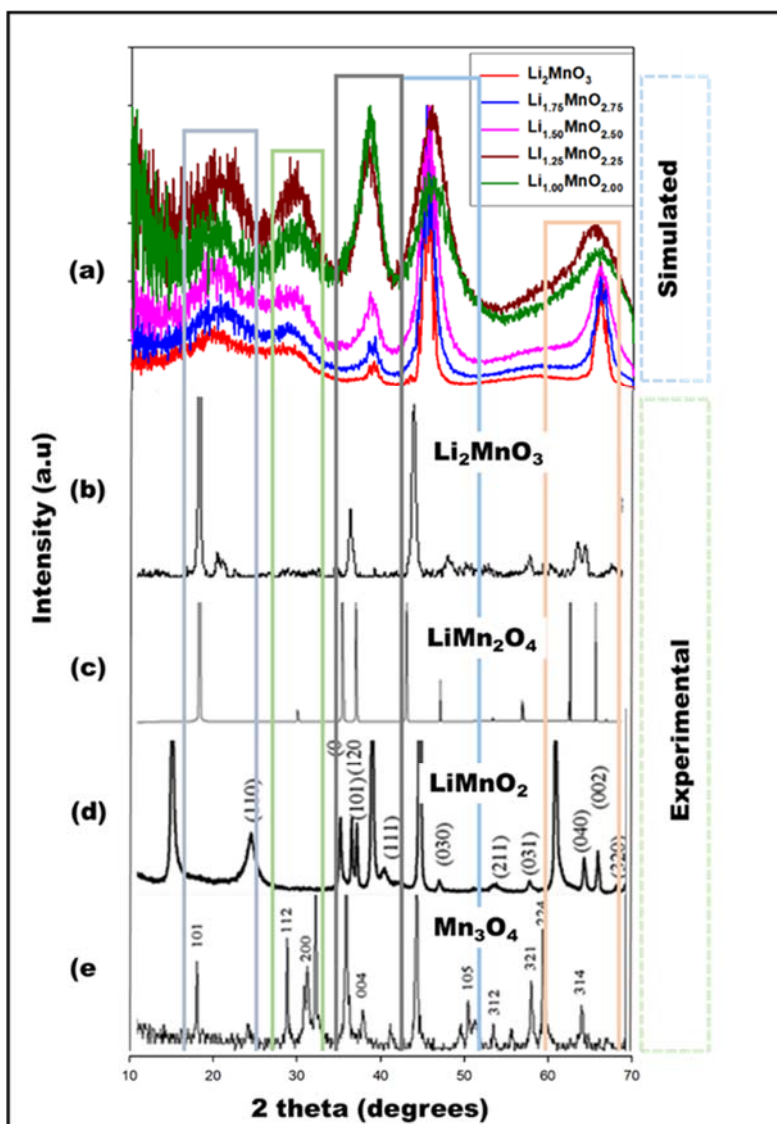
Figure 4.3: (a) Simulated XRDs for the Li$_{2-x}$MnO$_{3-x}$ nanospheres at various concentrations Li$_2$MnO$_3$ (red), Li$_{1.75}$MnO$_{2.75}$ (blue), Li$_{1.50}$MnO$_{2.50}$ (pink), Li$_{1.25}$MnO$_{2.25}$ (brown) and Li$_{1.00}$MnO$_{2.00}$ (green)] superimposed with (b) Li$_2$MnO$_3$ [80], (c) LiMn$_2$O$_4$ [81] (d) LiMnO$_2$ and (e) MnO$_3$ [82].
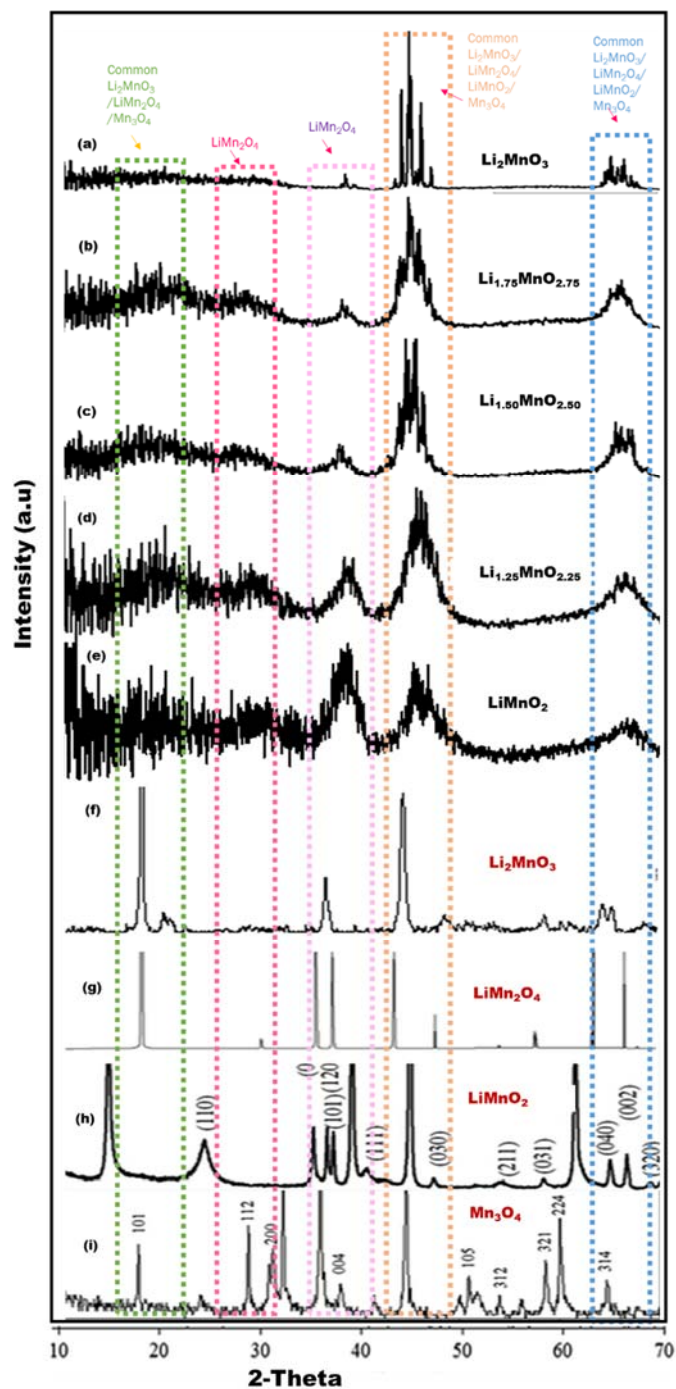
Figure 4.4: *Diffraction patterns for the simulated Li$_{2-x}$MnO$_{3-x}$ nanoporous 75 Å simulated nanoporous 73 Å (a) Li$_{1.75}$MnO$_{2.75}$ (b) Li$_{1.75}$MnO$_{2.75}$, (c) Li$_{1.50}$MnO$_{2.50}$, (d) Li$_{1.25}$MnO$_{2.25}$ and (e) Li$_{1.00}$MnO$_{2.00}$ superimposed with (b) Li$_2$MnO$_3$ [80], (c) LiMn$_2$O$_4$ [81] (d) LiMnO$_2$ and (e) MnO$_3$ [82].*
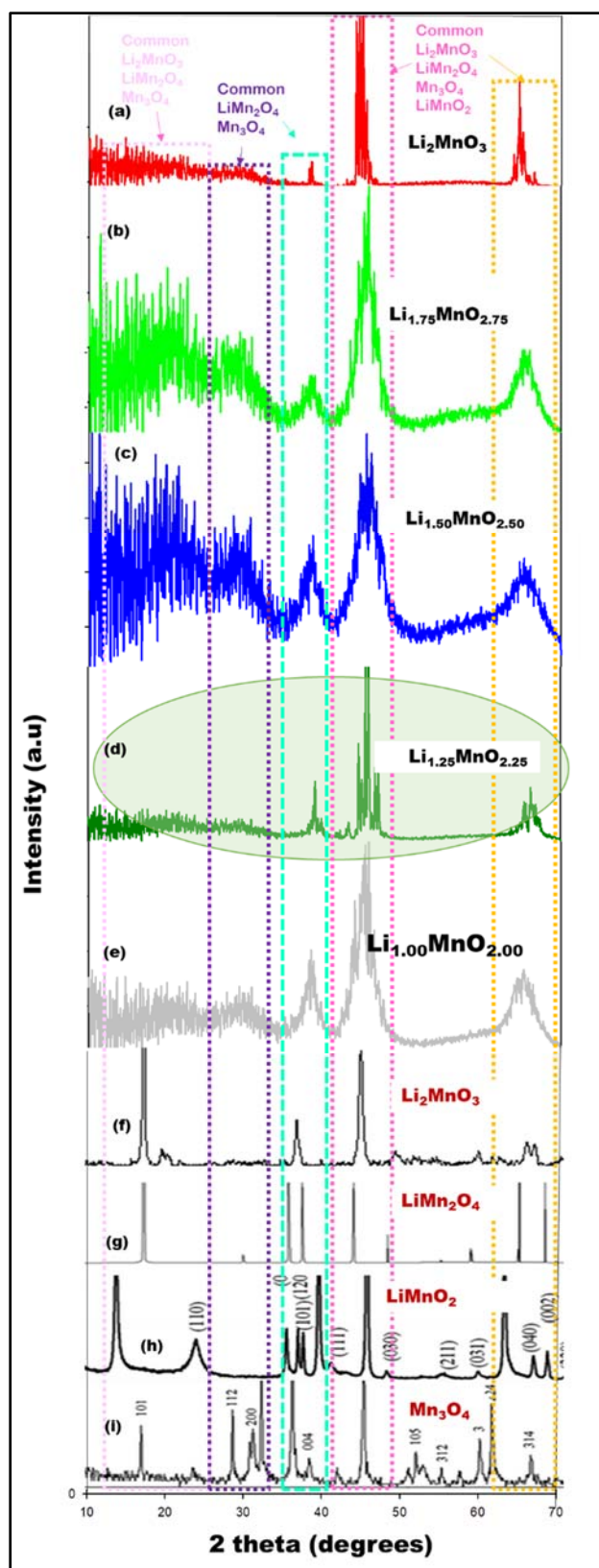
Figure 4.5: XRDs for the simulated nanoporous 73 Å Li$_{2-x}$MnO$_{3-x}$ systems (a) Li$_{1.75}$MnO$_{2.75}$ (b) Li$_{1.75}$MnO$_{2.75}$, (c) Li$_{1.50}$MnO$_{2.50}$, (d) Li$_{1.25}$MnO$_{2.25}$ and (e) Li$_{1.00}$MnO$_{2.00}$, superimposed with (b) Li$_2$MnO$_3$ [80], (c) LiMn$_2$O$_4$ [81] (d) LiMnO$_2$ and (e) MnO$_3$ [82].

4.3.4 Microstructures

Nanosphere

The crystallographic features that evolved during the charging mechanisms of the nanostructured $Li_{2-x}MnO_{3-x}$ systems obtained from cutting through each model are presented below. Figure 4.6 illustrates the microstructural analysis for the $Li_{1.75}MnO_{2.75}$ nanosphere respectively. The slice cut through $Li_{1.75}MnO_{2.75}$ nanosphere (a) shows that the structure crystallised into a multi-grained crystal, the structure also depicts a lot of defects and vacancies. To better view the structural transitions within (a), a small portion is magnified in (b) revealing the Li_2MnO_3 phase with cationic mixing as observed in chapter 3, (c) is the Li_2MnO_3 perfect model for comparison. We also observed the formation of a distorted cubic spinel phase $LiMn_2O_4$ (d) with lithium vacancies (blue oval) and lithium ions occupying manganese vacancies (red square), (e) is the $LiMn_2O_4$ perfect model comparable with the formed spinel phase in (d).
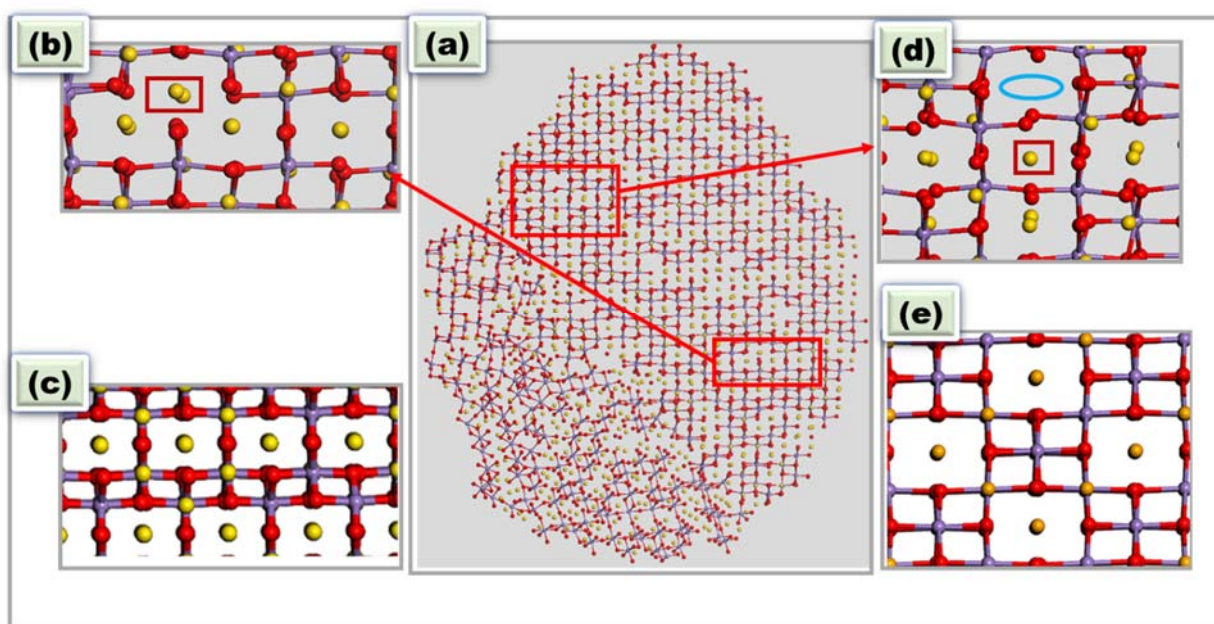
Figure 4.6: (a) Slice cut through $Li_{1.75}MnO_{2.75}$ nanosphere, (b) magnified portion of (a) revealing formation of Li_2MnO_3 comparable with (c) Li_2MnO_3 perfect model, (d) magnified portion of (a) revealing a distorted $LiMn_2O_4$, comparable with (e) the $LiMn_2O_4$ perfect model.

Figure 4.7 depicts (a) a slice cut through the $Li_{1.50}MnO_{2.50}$ system with magnified sections displaying the evolution of misoriented (b) Li_2MnO_3 and (d) $LiMnO_2$ phases. These were compared with perfect models of both the Li_2MnO_3 and $LiMnO_2$ depicted

in (c) and (e). The simulated structure is dominated by defects such as cation mixing and vacancies which triggers the formation of these polymorphs.
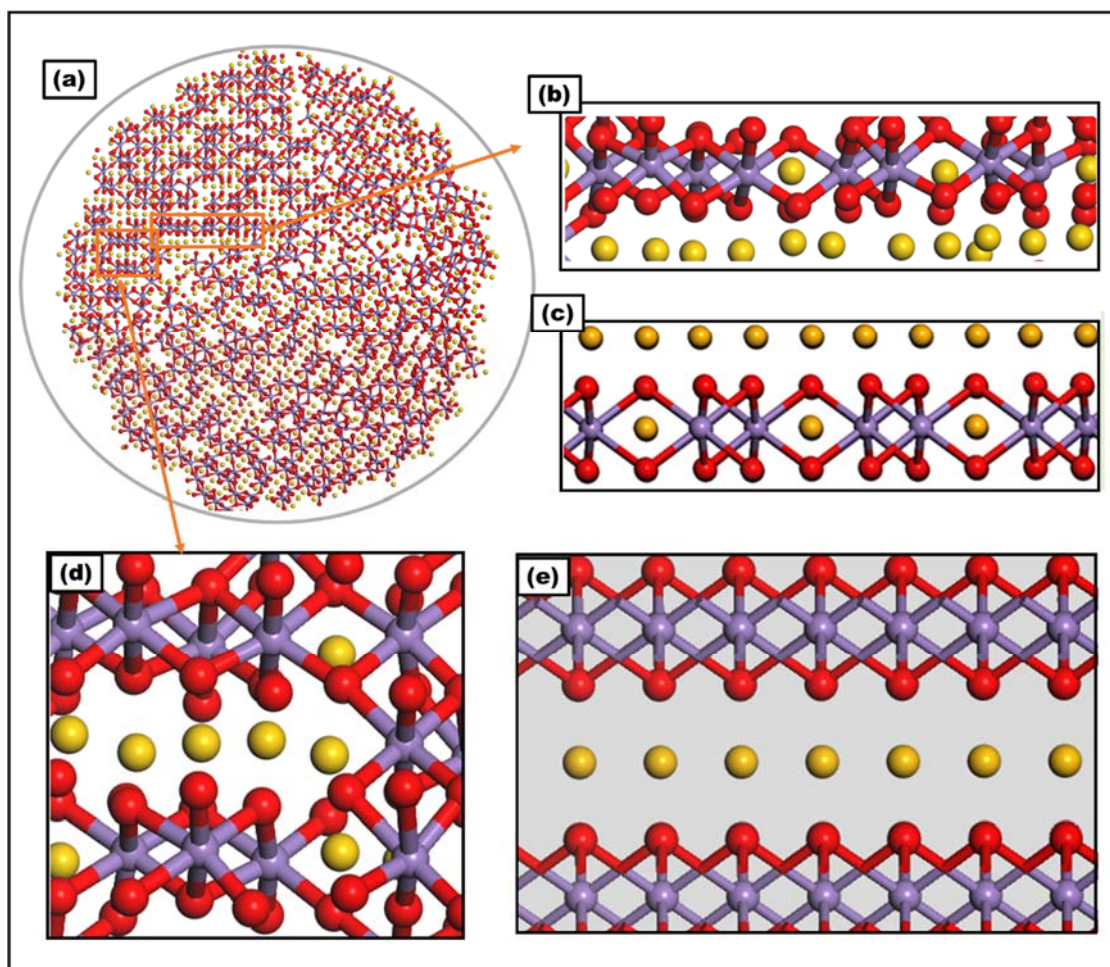
Figure 4.7: (a) Slice cut through $Li_{1.50}MnO_{2.50}$ nanosphere with (b) magnified portion of (a) showing the co-existence of Li_2MnO_3 and $LiMnO_2$ morphologies comparable with (c) the perfect models of Li_2MnO_3 and (d) another magnified portion of (a) depicting the $LiMnO_2$ phase which compares well with (e) $LiMnO_2$ perfect model.

Figure 4.8 illustrates the microstructural analysis for the $Li_{1.25}MnO_{2.25}$ nanosphere where (a) is the slice cut through with magnified portion (b) revealing the layered $LiMnO_2$ phase with Li mixing in Mn layers (red squares) comparable with the perfect model (c). The Li_2MnO_3 phase is also observed in (d) with Mn ions in Li layers. We note from the microstructure that the $Li_{1.25}MnO_{2.25}$ system depicts more grains making it difficult to analyse the microstructural features within the structure.
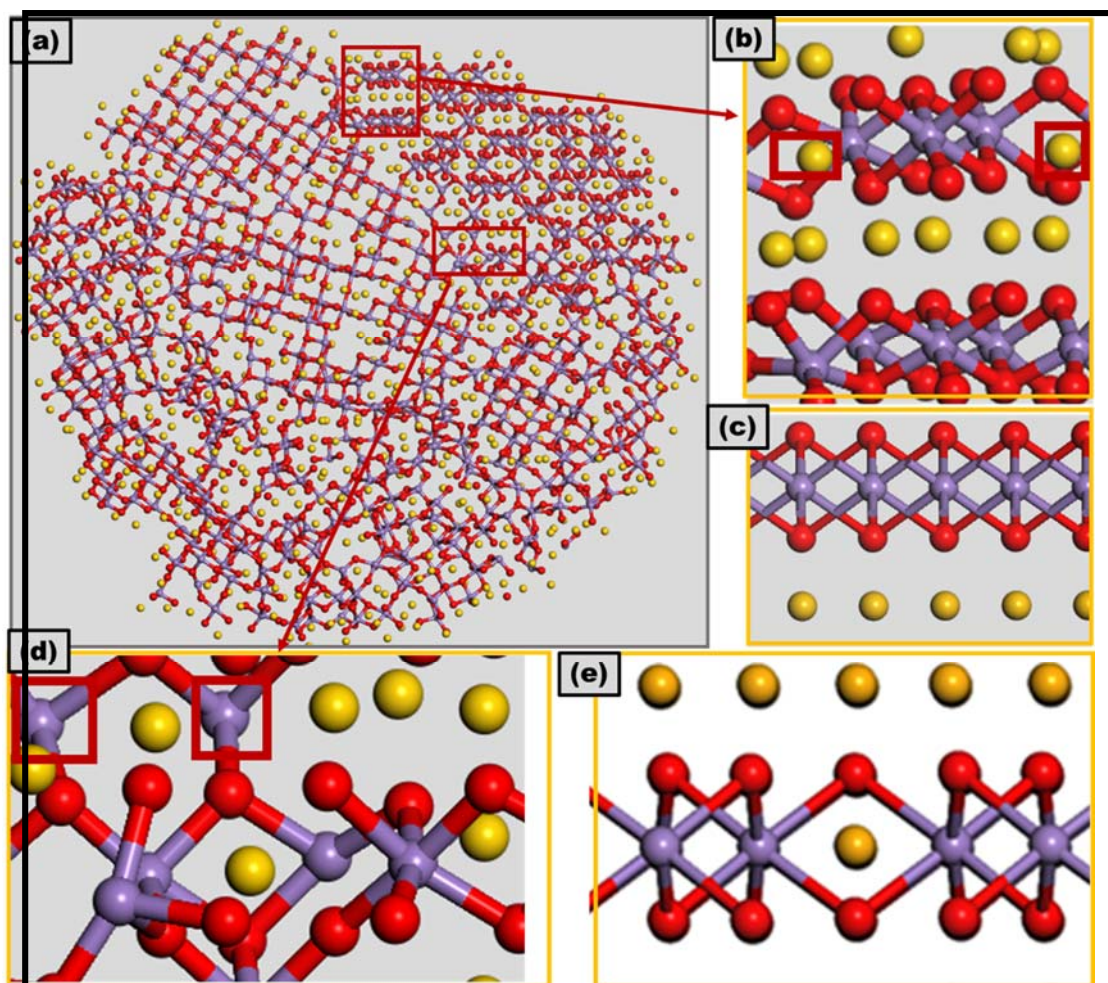
Figure 4.8: (a) Slice cut through Li$_{1.25}$MnO$_{2.25}$, (b) magnified portion of (a) showing the formation of layered LiMnO$_2$ comparable with (c) LiMnO$_2$ perfect model, (d) magnification of (a) revealing the distorted Li$_2$MnO$_3$ comparable with (d) Li$_2$MnO perfect model.

The slice cut through Li$_{1.00}$MnO$_{2.00}$ is displayed in figure 4.9, with (b) the magnified portion revealing the distorted LiMnO$_2$. Three layers are illustrated in (b), the lithium layer with the presence of Mn ions, Mn layer showing Li-ions occupying Mn vacancies and the third layer is the Li layer which is dominated by Mn ions. The structure reveals that all of the layers are mixed upon crystallisation.
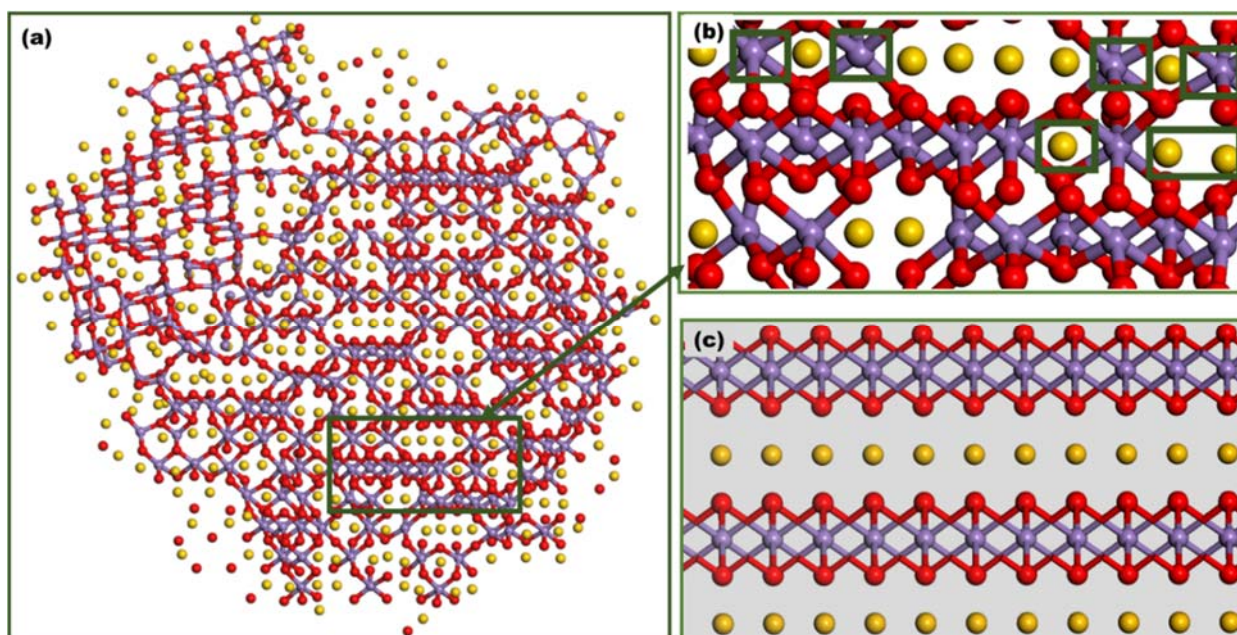
Figure 4.9: Microstructures of Li$_{1.00}$MnO$_{2.00}$ nanosphere showing (a) slice cut through, (b) magnification of (a) indicating the LiMnO$_2$ morphology with the mixing of Mn and Li layers and (c) the perfect model of LiMnO$_2$.

Nanoporous 75 Å

Figure 4.10-4.13 illustrates the microstructural analysis for the simulated nanoporous 75 Å with various concentration.

In figure 4.10 the slice cut through Li$_2$MnO$_3$ depicted in (a) is magnified in (b) and (c) revealing the presence of distorted layered Li$_2$MnO$_3$ comprising cation mixing (i) and vacancies (ii), the simulated model compares with the Li$_2$MnO$_3$ perfect model in (d). Figure 4.12 illustrates the Li$_{1.75}$MnO$_{2.75}$ concentration showing the presence of distorted LiMn$_2$O$_4$ (b) and (d-c) Li$_2$MnO$_3$ morphologies. A slice cut through the Li$_{1.50}$MnO$_{2.50}$ system is depicted in figure 4.12 and also reveals the (b) layered Li$_2$MnO$_3$ and (d) spinel LiMn$_2$O$_4$ morphologies. We also note from this concentration that the structure crystallised into multi-grains which are responsible for the phase transitions observed. In figure 4.13 the Li$_{1.00}$MnO$_{2.00}$ slice cut through the nanoporous also reveals the coexistence of the Li$_2$MnO$_3$ and LiMnO$_2$ phases.
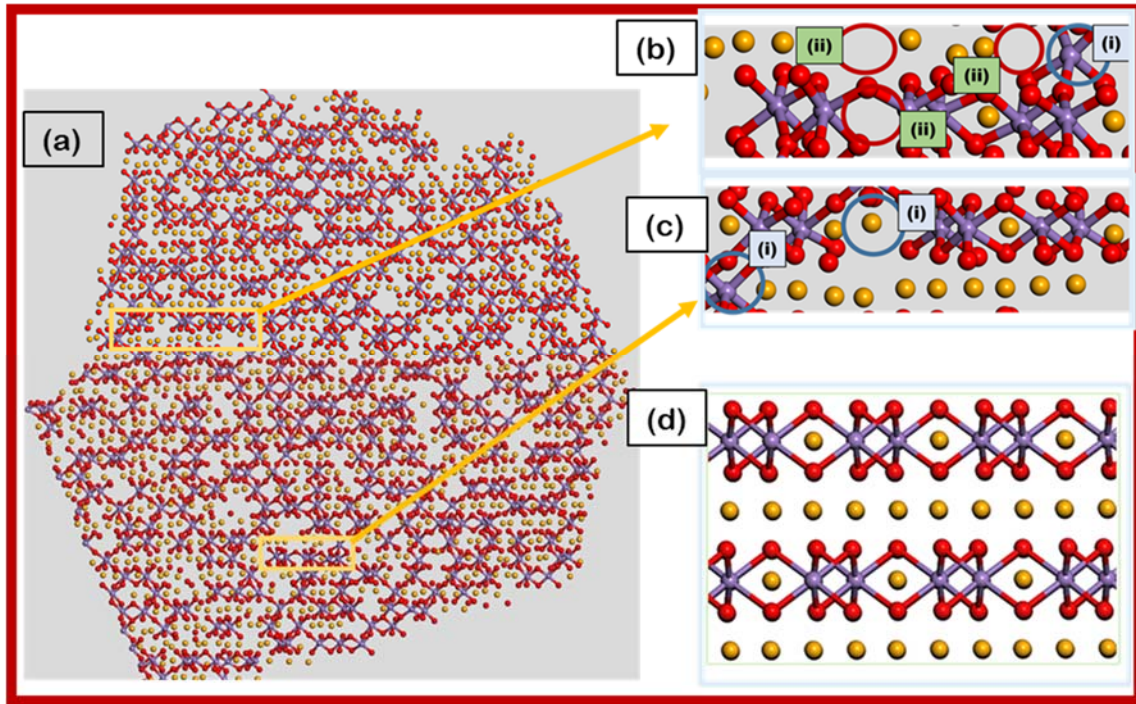
Figure:4.10: Li₂MnO₃ Nanoporous 75 Å microstructures where (a) indicates a slice cut through (b-c) magnified portion of (a) comparable with (d) Li₂MnO₃ perfect model.
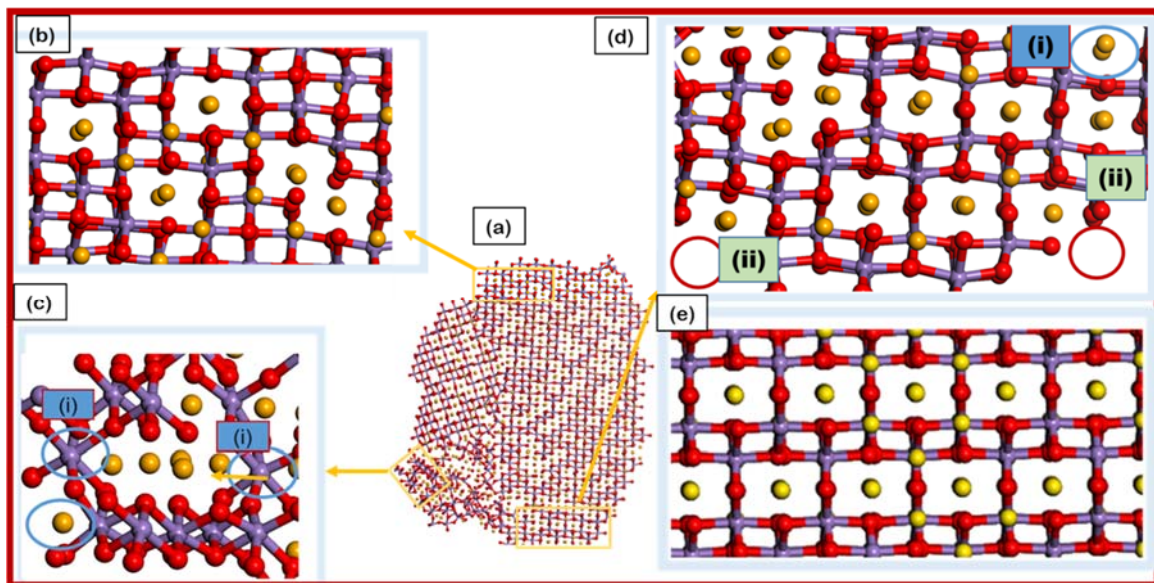
Figure 4.11: (a) Slice cut through Li₁.₇₅MnO₂.₇₅ nanoporous 75 Å with magnified portions (b) revealing the formation of LiMn₂O₄, (d, c) formation of layered Li₂MnO₃, compared with (e) perfect model of Li₂MnO₃,
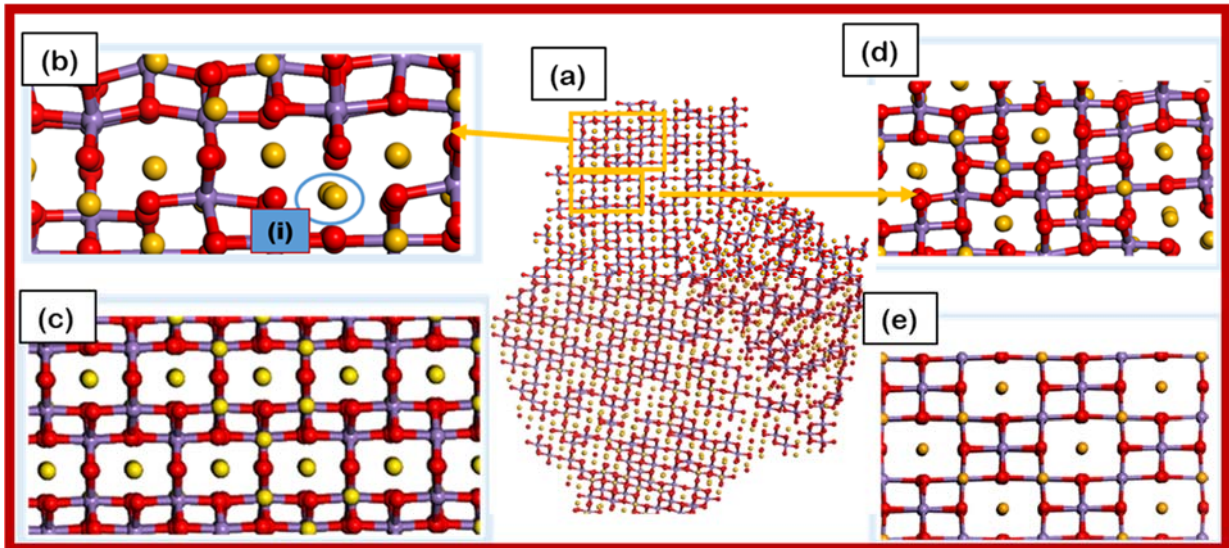
Figure 4.12: (a) Slice cut through Li$_{1.50}$MnO$_{2.50}$ nanoporous 75 Å with (b) magnified portion of (a) revealing the formation of Li$_2$MnO$_3$, comparable with (c) Li$_2$MnO$_3$ perfect model and (d) magnified portion of (a) showing the presence of LiMn$_2$O$_4$ comparable with (e) LiMn$_2$O$_4$ perfect model.
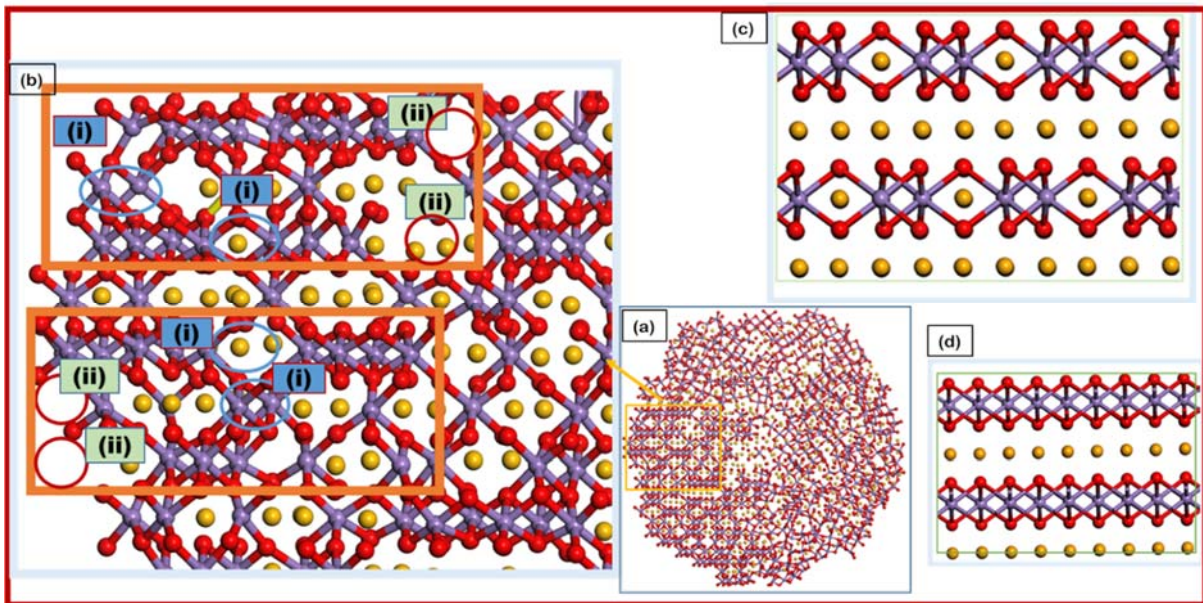
Figure 4.13: (a) Slice cut through Li$_{1.00}$MnO$_{2.00}$ nanoporous 75 Å with (b) magnified portion of (a) showing the coexistence of the layered Li$_2$MnO$_3$ and cubic spinel LiMn$_2$O$_4$ morphologies comparable with (c) Li$_2$MnO$_3$ perfect model and (d) LiMn$_2$O$_4$ perfect model.

Nanoporous 73 Å

The simulated nanoporous 73 Å $Li_{1.75}MnO_{2.75}$ is illustrated in figure 4.14 where (i) indicate that the structure recrystallised into a multi-grained crystal as evidenced by the presence of grain boundaries (blue). The presence of patterns is an indicative measure of the crystallisation state of the structure. In (ii), the microstructural analysis is illustrated where (a) is the slice cut through the $Li_{1.75}MnO_{2.75}$ layers to show the atomistic arrangement within the structure. A portion of (a) is magnified in (b) revealing the Li_2MnO_3 phase, depicting Li vacancy (red oval) and Mn/Li substitution (yellow square). The formed phase is comparable to the Li_2MnO_3 perfect model in (c).
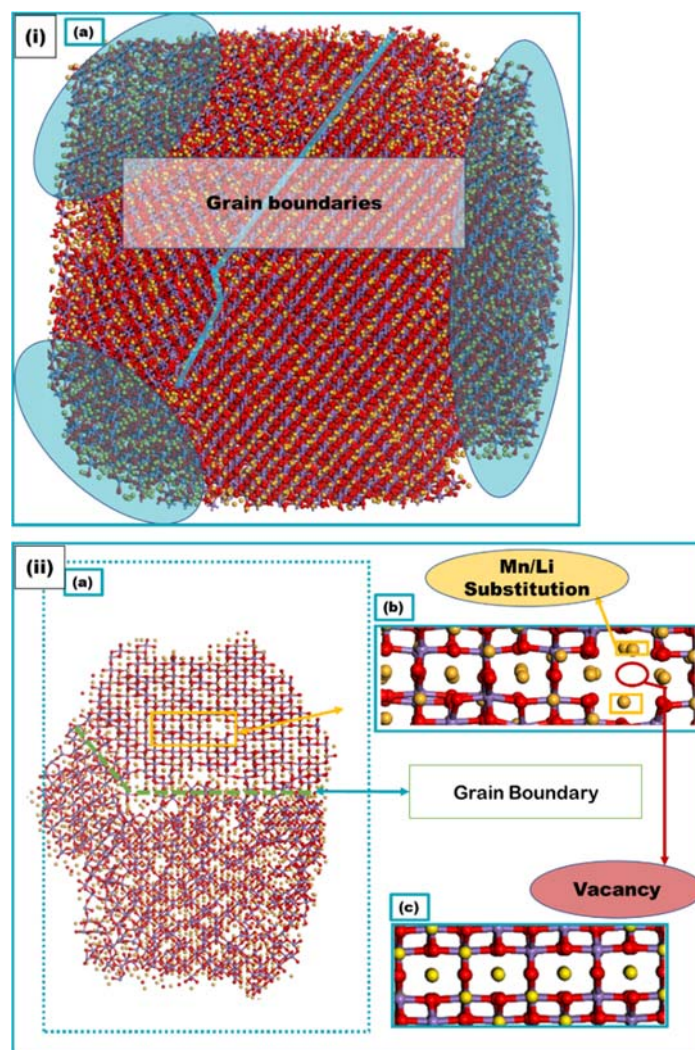
Figure 4.14: (i) (a) The simulated $Li_{1.75}MnO_{2.75}$ revealing grain boundaries, (ii)(a) a slice cut through the simulated nanoporous 73 Å $Li_{1.75}MnO_{2.75}$ with the magnified portion (b) indicating the layered Li_2MnO_3 phase compared with the perfect Li_2MnO_3 model (c).

Figure 4.15 below illustrates the simulated molecular graphics of $Li_{1.50}MnO_{2.50}$ revealing (i) (a) the grain boundaries evolved during crystallisation of the porous material. Again the structure has crystallised into a multi-grained structure. The slice cut through the $Li_{1.50}MnO_{2.50}$ layers is magnified in (b) showing the coexistence of the layered phases Li_2MnO_3 and $LiMnO_2$ comparable with (c) Li_2MnO_3 and (d) $LiMnO_2$ perfect models.
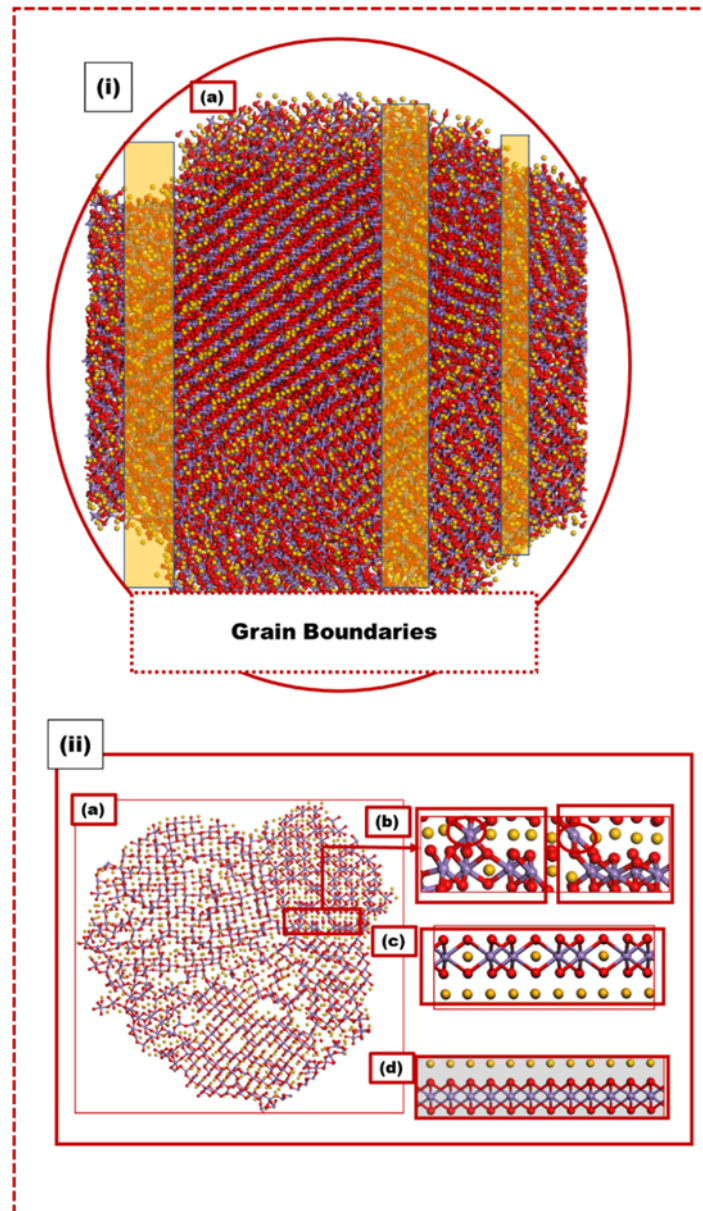
Figure 4.15: (i) Nanoporous $Li_{1.50}MnO_{2.50}$ molecular graphics revealing the grain boundaries, (ii)(a) slice cut through, (b) magnified portion of (a) showing co-existence of Li_2MnO_3 and $LiMnO_2$ comparable to their perfect models (c,d).

Figure 4.16 illustrates the simulated nanoporous $Li_{1.25}MnO_{2.25}$ concentration. In (i) the snapshot is magnified in (b) to better view the occupancy of Mn ions in tetrahedral sites arranged correspondingly as in spinel MnO_3 (c). The slice cut through is illustrated in (ii) where (b) is magnified to show the cubic spinel phase $LiMn_2O_4$ comparable with (c) $LiMn_2O_4$ perfect model. A magnified portion (d) reveals the layered Li_2MnO_3 with Li-ion substituting Mn ion (red circle), comparable with (e) Li_2MnO_3 model
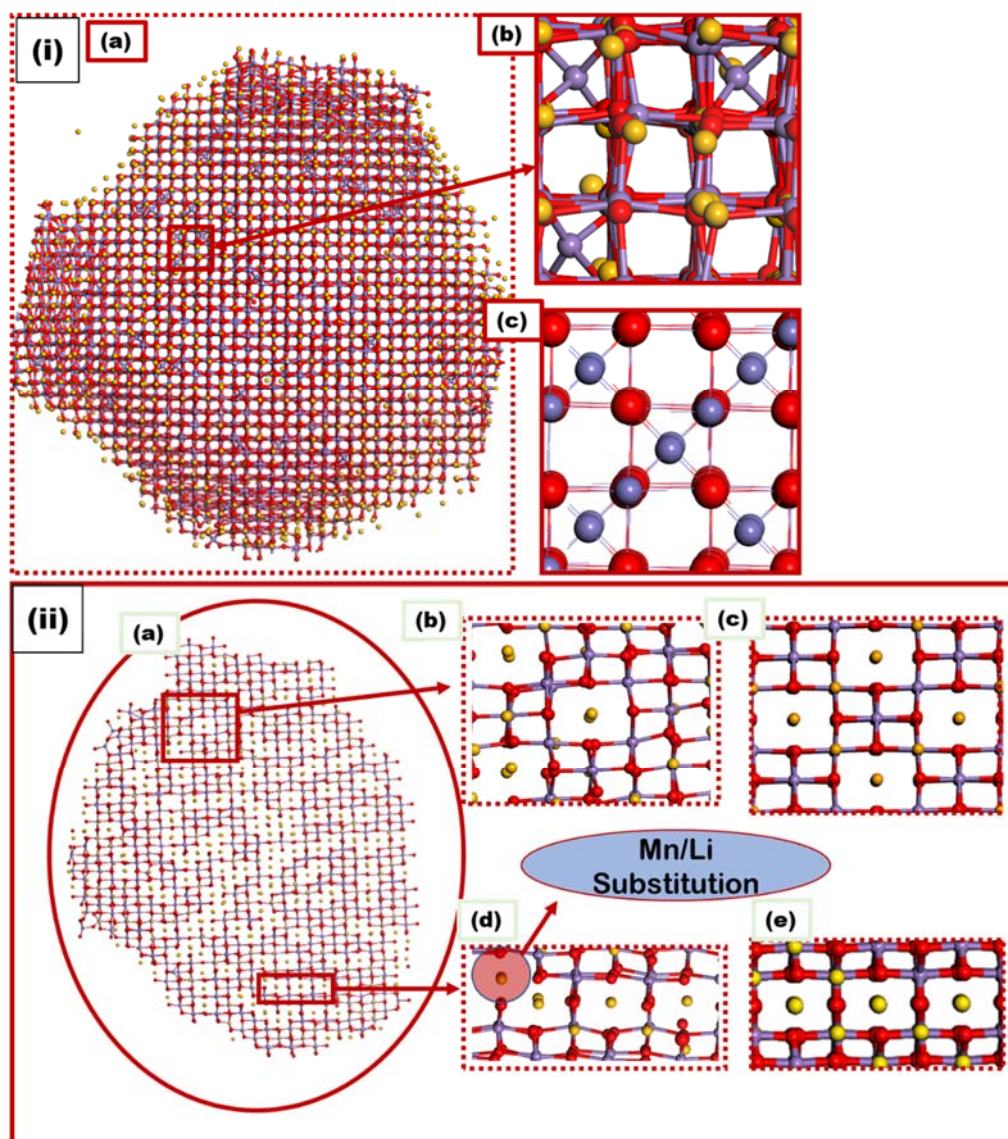
Figure 4.16: (i)(a) Nanoporous $Li_{1.25}MnO_{2.25}$ graphics revealing (b) spinel Mn_3O_4 comparable with (c) Mn_3O_4 perfect model. (ii) (a) Slice cut through $Li_{1.25}MnO_{2.25}$ depicting (b) $LiMn_2O_4$ and (d) Li_2MnO_3 phases comparable to their perfect models (c,e).

Figure 4.17 below depicts (i)(a) the simulated nanoporous $Li_{1.00}MnO_{2.00}$ snapshot revealing that the structure crystallised into a multi grained crystal, grain boundaries are depicted (blue). The microstructural features that evolved during crystallization are depicted in (ii) with (a,e) illustrating the slice cut through the $Li_{1.00}MnO_{2.00}$ layers viewed in a different orientation for better analysis. The magnified portions (b) shows the presence of the Li_2MnO_3 phase comparable to (c) the perfect model, (d) shows the presence of $LiMn_2O_4$ comparable to (e) perfect $LiMn_2O_4$ and (f) depict the presence of $LiMnO_2$ phase also comparable to (g) $LiMnO_2$ perfect model.
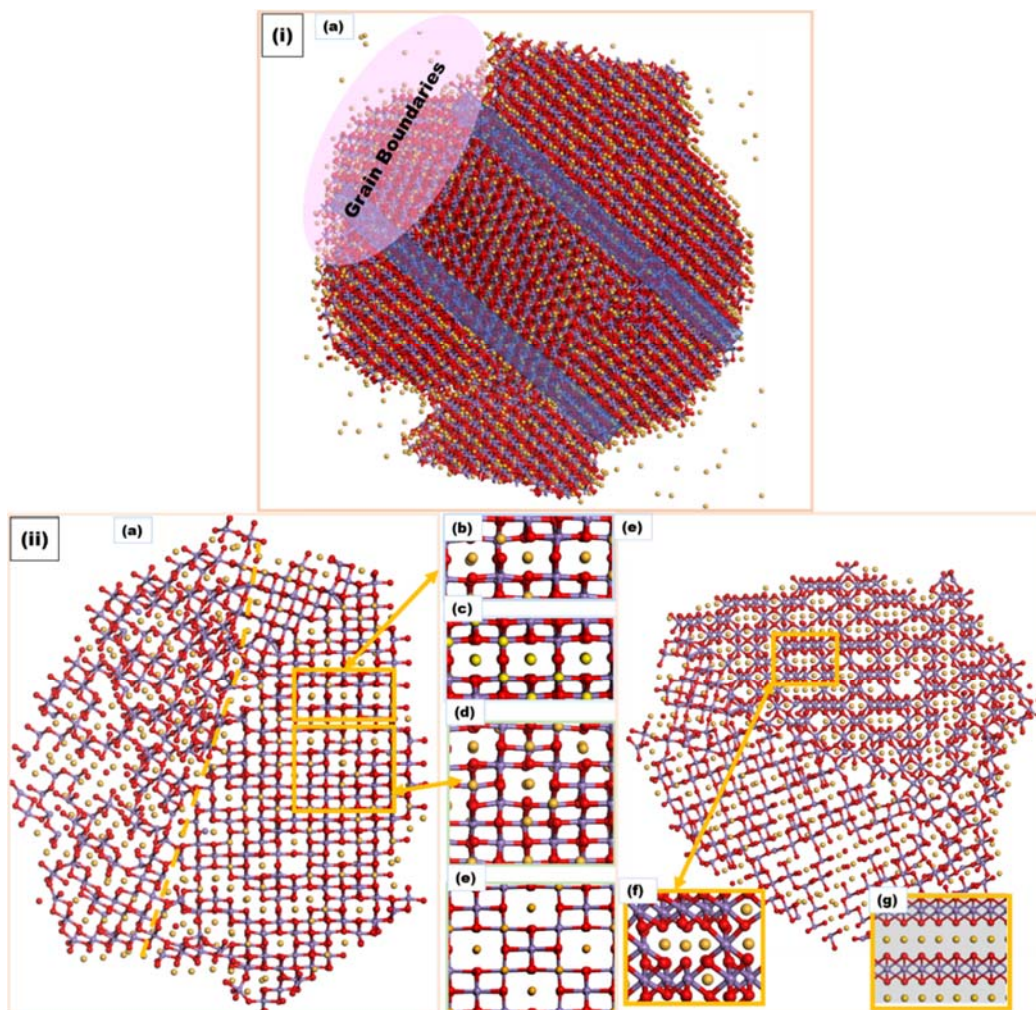
Figure 4.17: (i)(a) Snapshot representing the simulated nanoporous $Li_{1.00}MnO_{2.00}$ showing the presence of grain boundaries, (ii) (a) slice cut through $Li_{1.00}MnO_{2.00}$ revealing the (b) Li_2MnO_3, (e) $LiMn_2O_4$ and $LiMnO_2$, morphologies comparable to their perfect models (c, e, g).

4.3.5 Diffusion Coefficient

The diffusion coefficient plots calculated at various temperatures for the $Li_{1.75}MnO_{2.75}$ and $Li_{1.50}MnO_{2.50}$ systems are illustrated in figure 4.18, where the nanosphere, nanoporous 75 and nanoporous 73 configurations are indicated by black, red and blue lines. From the $Li_{1.75}MnO_{2.75}$ concentration depicted in (a), it can be noted that the nanosphere diffuses extremely better than the nanoporous configurations. Lithium ions in the nanosphere start diffusing from approximately 0.2 $nm^2.s^{-1}$ and move linearly until it reaches the maximum diffusion at 1000 K with a value of 3.4 nm^2s^{-1}. The graph was magnified in (b) to observe how the nanoporous systems diffuse. From (b), the nanoporous 73 diffuses slightly higher than the nanoporous 75, however, both systems had diffusion coefficient values of less than 0.2 $nm^2.s^{-1}$. Figure 4.18 (c), indicates the $Li_{1.50}MnO_{2.50}$ system, again, the nanosphere diffuses better, however, there is a slight disruption in the linear motion of the lithium ions at 500 K, and the graph continues with the linear motion at 700 K. The magnified portion of (c), is depicted in (d), to explore lithium kinetics in the nanoporous systems. Again, the nanoporous 73 diffuses better than nanoporous 75 which showed a decline to zero in diffusion coefficient at 700 K.

Figure 4.19 illustrates the diffusion coefficient plots calculated for the $Li_{1.25}MnO_{2.25}$ and $Li_{1.00}MnO_{2.00}$ configurations. Accordingly, (a) represents the $Li_{1.25}MnO_{2.2}$ system revealing that the nanosphere diffused better with the highest diffusion coefficient value of 38 $nm^2.s^{-1}$. However, the diffusion coefficient fluctuates due to factors such as phase transformation. At 400-500 K, there is a plateau, followed by an increase in diffusion to maxima at 700 K, the diffusion then decreases and increases again at 900 K. The magnified portion of (a) in (b), reveals that the nanoporous 75 diffuses better than nanoporous 73. For the fourth $Li_{1.00}MnO_{2.00}$ system depicted in (c), the nanosphere still exhibits a high diffusion coefficient of lithium, however, this concentration is dominated by the fluctuation of the peaks. The nanoporous 73 has improved in lithium kinetics for this concentration with the highest diffusion value at approximately 6.1 nm^2s^{-1}. The diffusion coefficient for the nanoporous 75 is magnified in (d) with the lowest diffusion coefficient values.
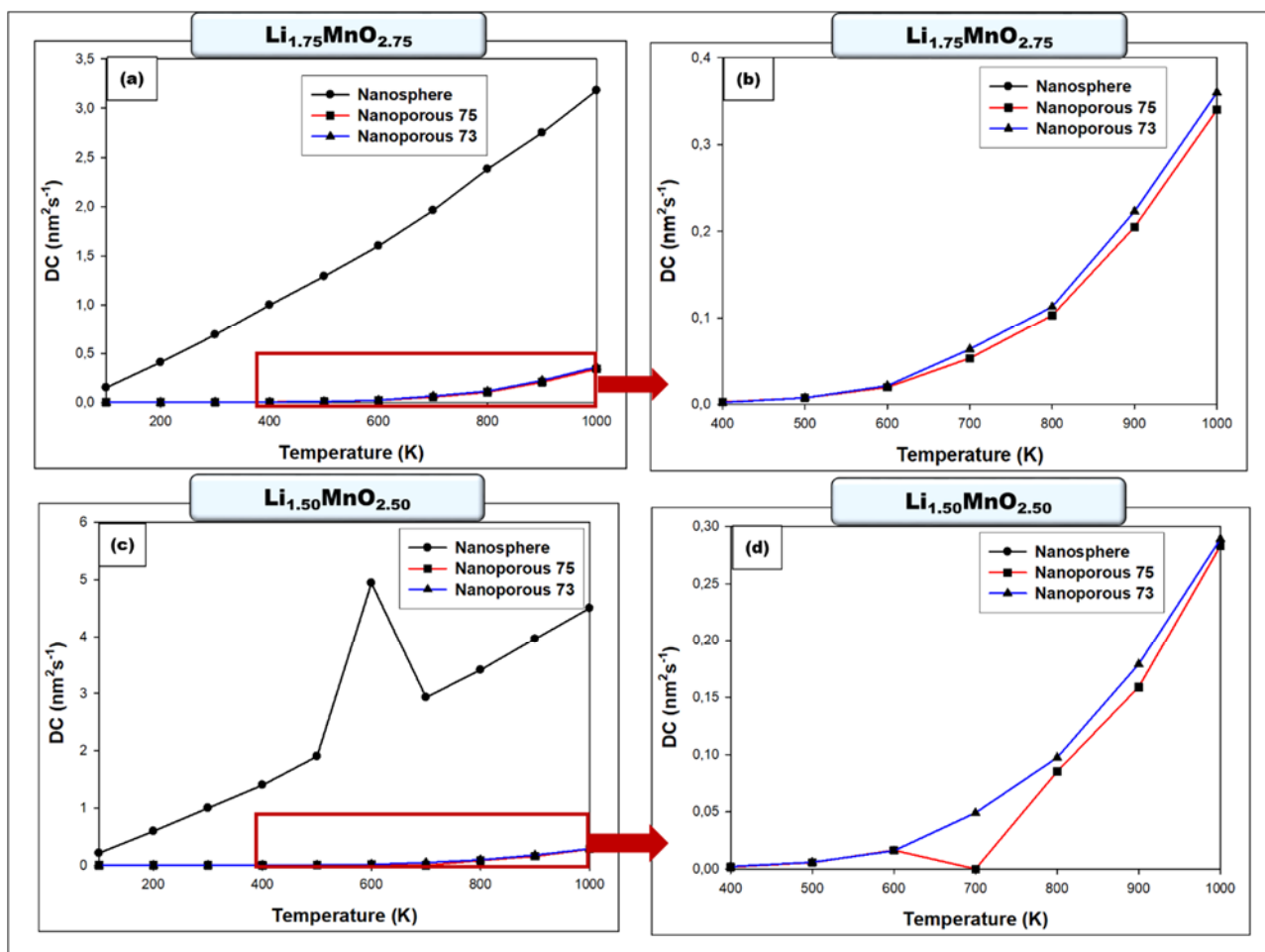
Figure 4.18: *The diffusion coefficient vs temperature graphs for the lithium ions in the nanosphere (black), nanoporous 75 (red), nanoporous 73 (blue) displaying the (a) $Li_{1.75}MnO_{2.75}$, (b) magnified portion of (a), (c) $Li_{1.50}MnO_{2.50}$ and (d) magnified portion of (c).*
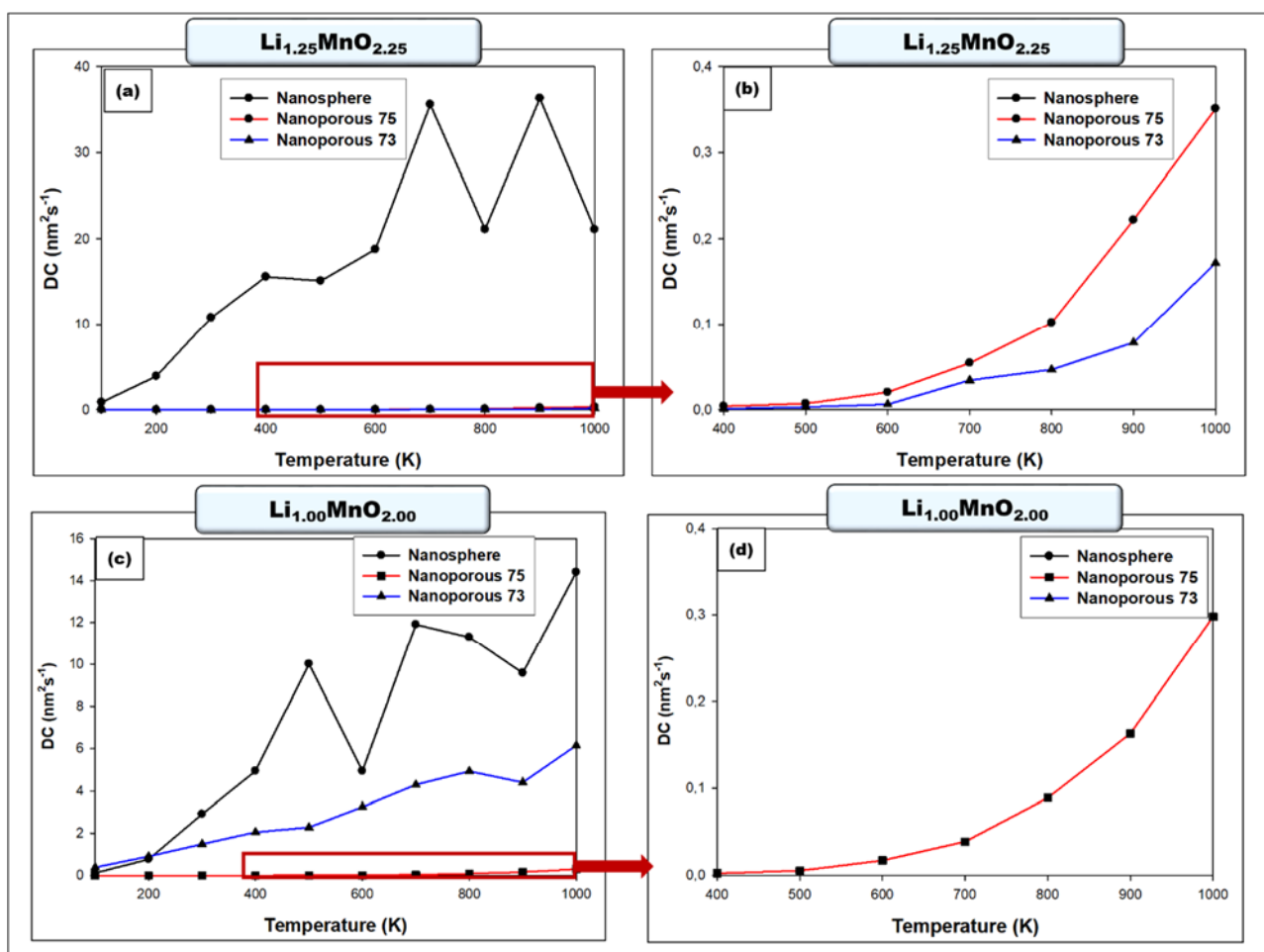
Figure 4.19: The diffusion coefficient calculated at different temperatures for the lithium ions in the nanosphere(black), nanoporous 75 (red), nanoporous 73 (blue) for the (a) Li$_{1.25}$MnO$_{2.25}$, (b) magnified portion of (a), (c) Li$_{1.00}$MnO$_{2.00}$ and (d) magnified portion of (c).

4.4. Summary

The layered Li$_2$MnO$_3$ possesses a high number of exploitable lithiums, leading to its high theoretical capacity. However, there is a pressing need for exploration of the crystallographic and electrochemical complexities for their use in high-density lithium-ion batteries [13]. Considering that lithium extraction from Li$_2$MnO$_3$ prompts the release of oxygen which attributes to structural degradation [83], oxygen was removed along with lithium ions to restrain the release of oxygen [84] during the cycling process. Consequently, Li$_{2-x}$MnO$_{3-x}$ composites i.e. Li$_{1.75}$MnO$_{2.75}$, Li$_{1.50}$MnO$_{2.50}$, Li$_{1.25}$MnO$_{2.25}$ and Li$_{1.00}$MnO$_{2.00}$ were modelled to mimic the discharge process for the nanostructured (spherical, porous) systems. The radial distribution functions plots confirm that the models crystallised as depicted by the presence of multiple sharp peaks. The resulting structures crystallised into multiple grains which increased with

decreasing Li/O content along with stacking faults and vacancies thus leading to Mn ions migrating to the Li layers. This also affects the precise structural analysis due to the level of defects formed within the crystal domains[24]. Our models reveal that all layers are mixed upon crystallisation leading to the formation of disoriented phases including the layered Li_2MnO_3, layered $LiMnO_2$ and cubic spinel $LiMn_2O_4$. Again, the models showed the presence of grains which increased along with Li/O extraction, however, for nanoporous 73 Å, the $Li_{1.25}MnO_{2.25}$ concentration depicted no grain boundaries. The XRD of the simulated systems depicts broader peaks which are more intense at lower angles corresponding to the ordering of atoms in the transition metal layers. The spinel and layered morphologies observed from the microstructures are also observed in the XRD analysis. Again the nanoporous 73 Å $Li_{1.25}MnO_{2.25}$ XRDs is narrowed compared to the other concentrations. The diffusion coefficient plots reveal that the nanosphere has better lithium-ion kinetics than the nanoporous 73 Å and 75 Å. Our results have revealed the different internal structural transitions that occur within the intermediate phases of the different morphologies and their impact on the cycling capabilities of Li_2MnO_3 cathodes and similar results were observed experimentally [37].

Chapter 5

The Effect of Sodium Substitution on Li$_2$MnO$_3$ Nano-architectures

5.1. Introduction

In the previous chapters, the charging of Li$_2$MnO$_3$ involving the removal of oxygen resulted in lattice reconstruction which led to structural transformation. Considering that the degradation of a material depends on the composition and crystal structure of a material [85], sodium (Na) substitution has been recommended for stabilizing the structures of lithium-rich cathodes [19]. Furthermore, Na possesses a slightly larger radius (1.06 Å) compared to Li (0.76 Å) which enables it to expand the lithium layer and thus promote the diffusion of lithium during cycling and also improve the battery capacity [86]. In this chapter, Na-doped models of the form Li$_{2-x}$Na$_x$MnO$_3$ (0 ≤ x ≤ 2) are investigated via the simulated A+R technique in an attempt to enhance the electrochemical performance of the nano-Li$_2$MnO$_3$. Amorphisation will be carried out at different temperatures in order to uncover the temperature at which all the long-range interactions will be lost. The resulting structures will be characterised by the XRD which will be compared with that of the simulated Li$_2$MnO$_3$ from previous chapters. Structural analysis will be carried out by comparing the molecular graphics of the sodium substituted and pristine simulated models. Finally, the diffusion coefficient will be calculated at various temperatures to determine the effect of Na substitution on the movement of Li in the Li$_{2-x}$Na$_x$MnO$_3$ host material.

5.2. Methodology

The Li$_2$MnO$_3$ nanosphere, generated from a previous study (chapter 3) through the A+R technique was used to dope sodium ions into the lithium lattice resulting in a series of systems with varying Li/Na concentrations i.e. Li$_{2-x}$Na$_x$MnO$_3$ (0 ≤ x ≤ 2). To achieve amorphous configurations, the pressure was set to zero and the temperature varied until a complete loss of long-range interaction was reached. The simulations were carried out for 0.001 ps, with Ewald precision set to 1d-5, under the NVE ensemble. Recrystallisation was carried out at the temperature range of 1600-1800 K, employing the NVT ensemble. Again, the pressure was set to zero, with 5 million steps printing RDFs every 250 steps at 10 Å cut-off and 0.003 timesteps. The diffusion

coefficients were calculated at various temperatures to study the movement of Li-ions and the effect of Na substitution on the Li_2MnO_3 structure. Figure 5.1 is a schematic illustration of the $Li_{2-x}Na_xMnO_3$ synthesis procedure indicating (a) the Li_2MnO_3 unit cell revealing the atomic arrangement conforming to a monoclinic crystal structure with C2/m symmetry, (b) the nano-spherical Li_2MnO_3 cleaved from its parent bulk and (c) is the sodium doped nanosphere ($Li_{2-x}Na_xMnO_3$) where Li ions were substituted with Na ions
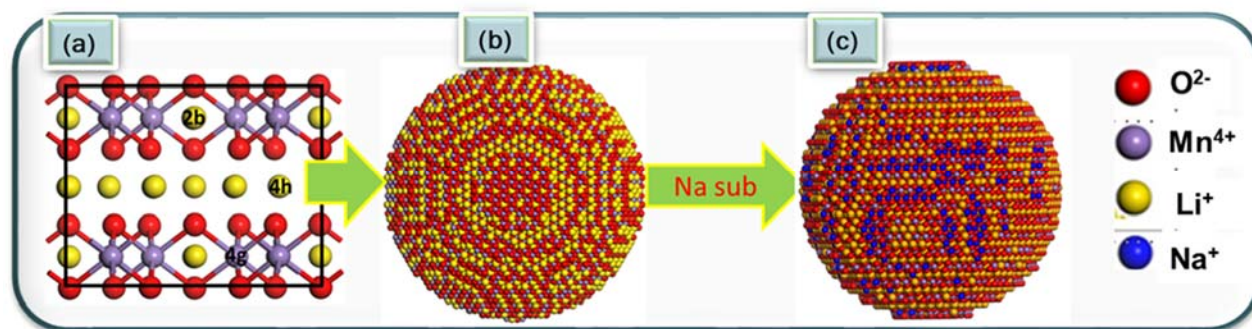
Figure 5.1: Schematic diagrams representing (a) layered Li_2MnO_3 unit cell revealing the atomic arrangement of Li, Mn, O (b) cleaved nano-spherical Li_2MnO_3 with 32148 atoms and (c) Na doped nano-spherical $Li_{2-x}Na_xMnO_3$ where the red, purple, yellow and blue spheres represent oxygen, manganese, lithium and sodium.

5.3. Results

5.3.1. Concentration Variations During A+R of $Li_{2-x}Na_xMnO_3$

Molecular graphics representing the Na_2MnO_3 nanosphere during amorphisation are illustrated in figure 5.2 below. Accordingly, amorphisation simulations were attempted at different temperatures in order to determine the temperature at which a complete loss of long-range interactions will be reached for the spherical Na_2MnO_3. The perfectly ordered Na_2MnO_3 model is shown in (a) where the blue, red and purple spheres represent Na, O and Mn ions. A temperature of 100 K applied to the system was not sufficient to amorphise the Na_2MnO_3 system as indicated in (b). The temperature was then raised to 600 K, and again, this was inadequate since the structure still maintained its crystallinity with the presence of patterns confirming the long-range interactions. In (d), the temperature was set to 1000 K and the structure thereof reveal some regions losing the long-range interactions, however, the structural morphology is lost due to the structure breaking into two parts. The same was observed for the structure subjected to a temperature of 1000 K, indicated in (e).

Further temperature increment to 1700 K led to an amorphous configuration as shown in (f), however, the structure transforms from spherical to a rod-like shape.
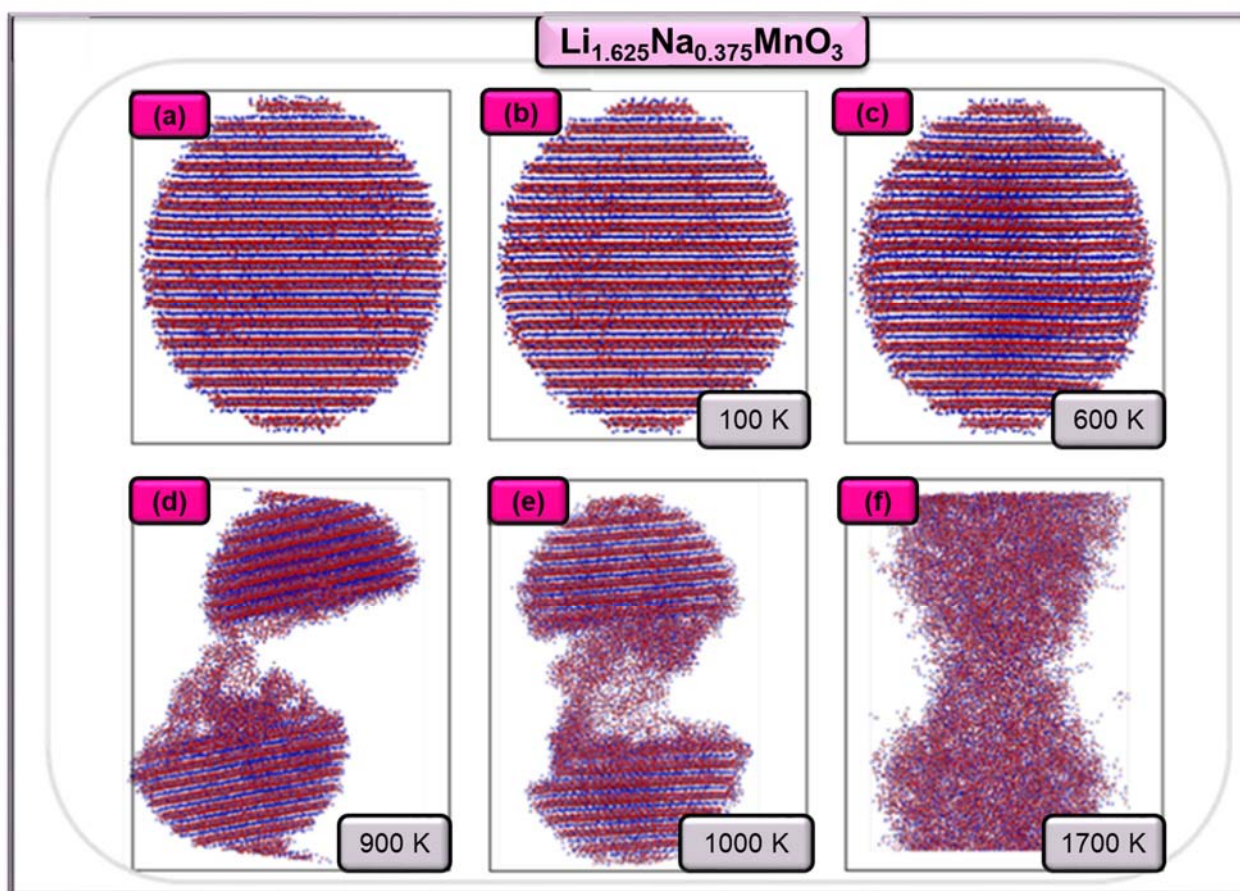
Figure 5.2: Atomistic models indicating the (a) Na₂MnO₃ system during the amorphisation process carried out at (b) 100 K, (c) 600 K, (d) 900 K, (e) 1000 K and (f) 1700 K.

The Na-incorporated $Li_{0.50}Na_{1.50}MnO_3$ nanosphere is illustrated in figure 5.3, where (a) indicates the perfectly packed crystalline $Li_{0.50}Na_{1.50}MnO_3$ configuration before amorphisation. Amorphisation was realised at 1500 K as evidenced by a complete loss of long-range interaction in (b). In (c), recrystallisation was attempted at 1500 K and the structure thereof shows no apparent phase transition, suggesting that the applied temperature might be insufficient. The temperature was elevated to 1800 K and the structure is indicated in (d). It is apparent that at this temperature (1800 K), the structure fails to recrystallise but instead transforms from spherical to rod-like morphology similar to the one observed in figure 5.2 above for the Na_2MnO_3 system during the amorphisation process.
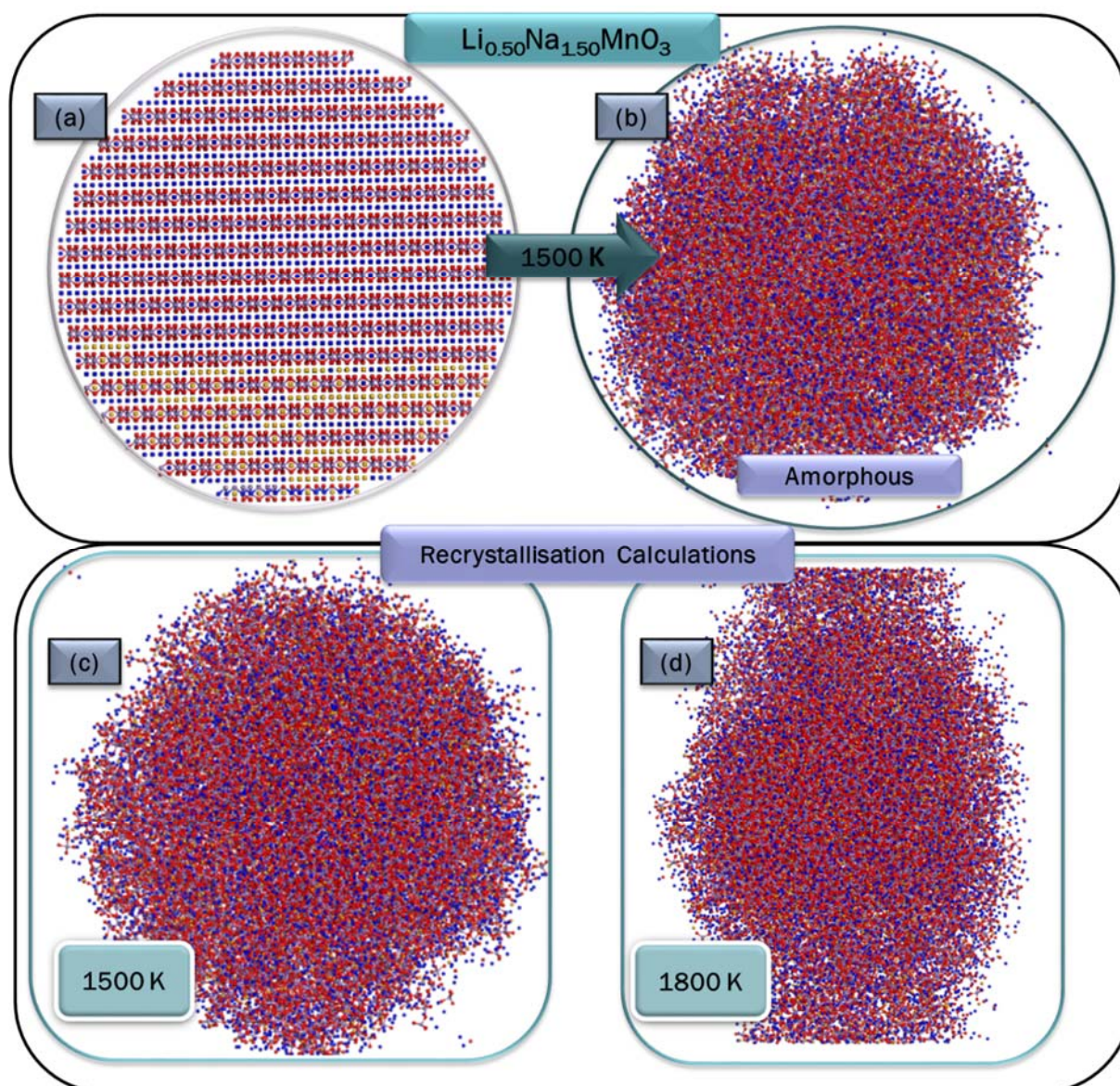
Figure 5.3: Molecular graphics of the $Li_{0.50}Na_{1.50}MnO_3$ (a) nanocluster, (b) amorphised configuration achieved at 1600 K, (c,d) recrystallisation calculations carried out at 1500 and 1800 K.

Figure 5.4 illustrates the Na-incorporated $Li_{1.00}Na_{1.00}MnO_3$ system where (a) represents the crystalline perfect structure prior to amorphisation. In an attempt to amorphise the system, a temperature of 1200 K was applied resulting in a partially amorphous $Li_{1.00}Na_{1.00}MnO_3$ configuration depicted in (b). Moreover, the structure still possesses patterns, indicated by the pink rectangle, which confirms the long-range interactions in some regions of the sphere. Also, the structure divides into two parts leading to the transformation from a spherical to a rod-like configuration. Further temperature increment to 1500 K gave rise to an amorphous configuration represented

in (c). However, the $Li_{1.00}Na_{1.00}MnO_3$ at this temperature (1500 K) amorphised into a rod-like structure instead of the initial spherical shape.
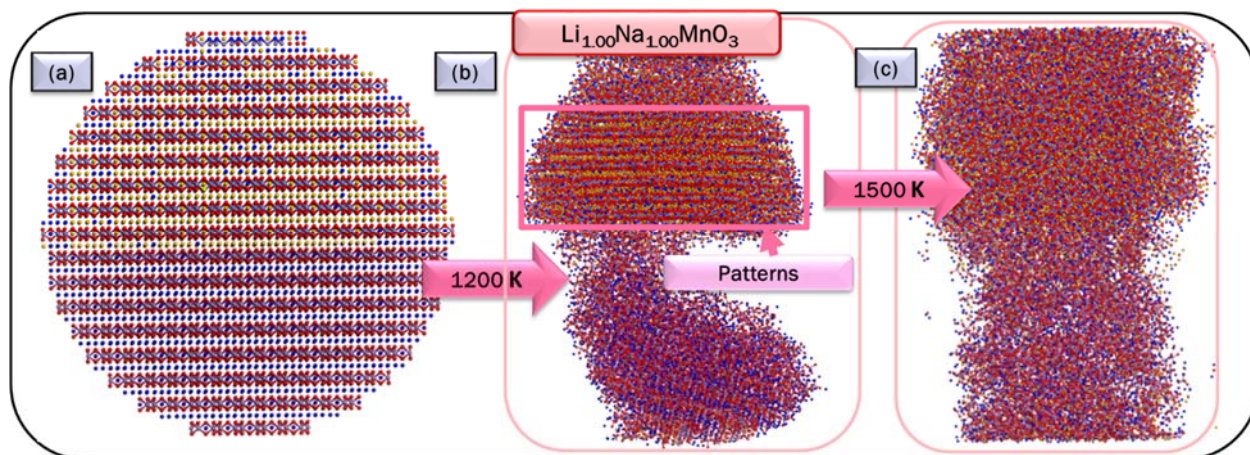
Figure 5.4: Molecular graphics for the $Li_{1.00}Na_{1.00}MnO_3$ (a) perfectly ordered model (b) partially amorphous configuration at 1200 K and (c) amorphous structure carried out at 1500 K.

The atomistic representation of the Na-doped $Li_{1.50}Na_{0.50}MnO_3$ nanosphere along with the RDF plots during the amorphisation and recrystallisation process is illustrated in figure 5.5. An orderly arranged crystalline $Li_{1.50}Na_{0.50}MnO_3$ in (a) was successfully amorphised at 1700 K. The structure has maintained its spherical structural morphology as seen in (b). Recrystallisation was performed at the same temperature (1700 K) and is evidenced by the presence of patterns. It is worth noting that the structure has recrystallised into a multi-grained structure with grain boundaries indicated by the orange dotted line in (c). In (d), the RDF plot represents the amorphous configuration and depicts broader peaks as an indicative measure of amorphisation. The recrystallised RDF graph is depicted in (c), showing an increased number of sharp peaks confirming that recrystallisation was achieved at 1700 K.
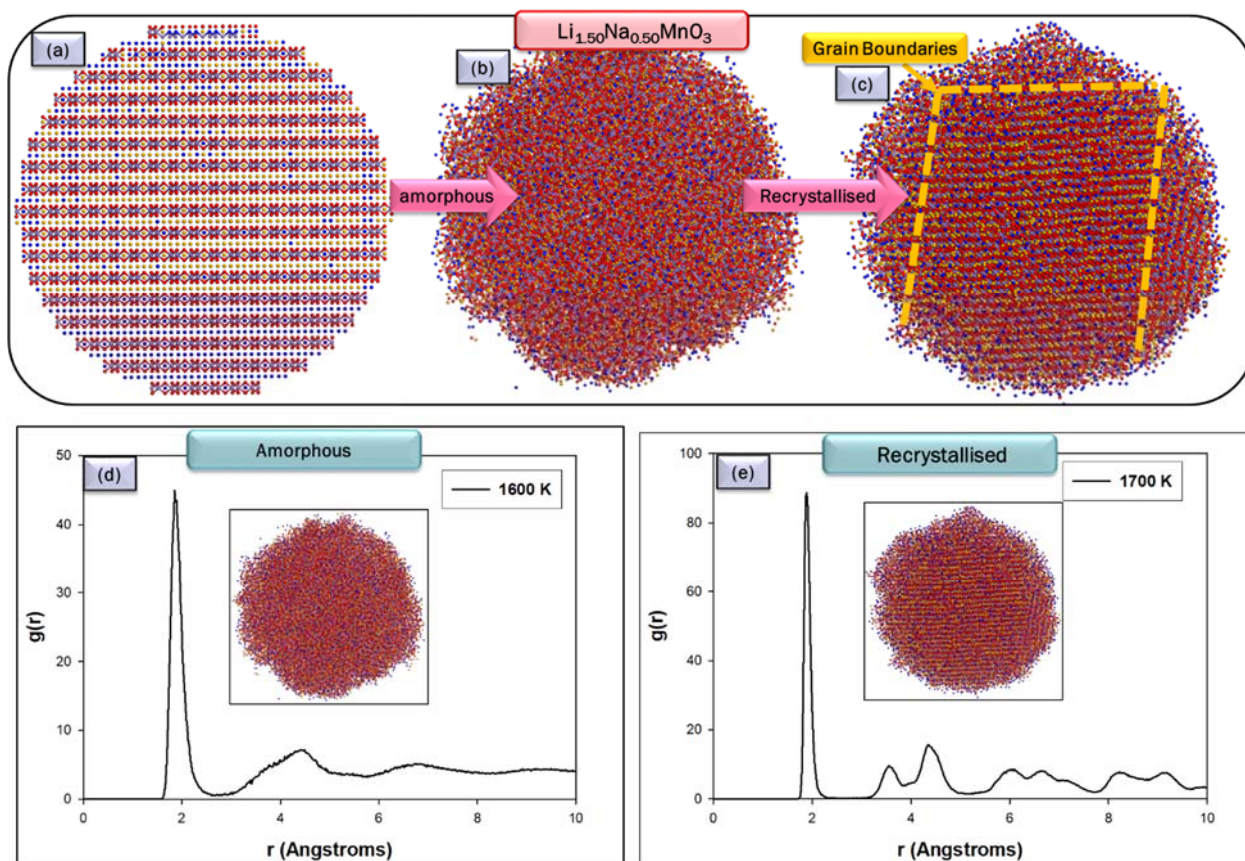
Figure 5.5: Molecular graphics representing the $Li_{1.50}Na_{0.50}MnO_3$ (a) nanocluster, (b) amorphous configuration obtained at 1700 K, (c) recrystallised configuration carried out at 1700 K, (d,e) amorphous and recrystallised RDF graphs.

In figure 5.6 below, the snapshot representation for $Li_{1.625}Na_{0.375}MnO_3$ during the amorphisation and recrystallisation calculations is depicted with (a) displaying the orderly structured $Li_{1.625}Na_{0.375}MnO_3$. Amorphisation calculations were carried out at 1700 K and the structure thereof is shown in (b). In the previous concentrations, the structures during the A+R process were either maintaining the spherical shape or transforming into rod-like structures. This concentration however behaves differently since it took a porous-like shape upon amorphisation. The calculations were tested at different temperatures but yielded the same results. This shows that the transformation was not triggered by temperature variation but by the amount of Na in the system. The structure also managed to recrystallise at the same temperature of 1700 K as indicated in (c) and this was again evidenced by the presence of patterns on the structure.

63
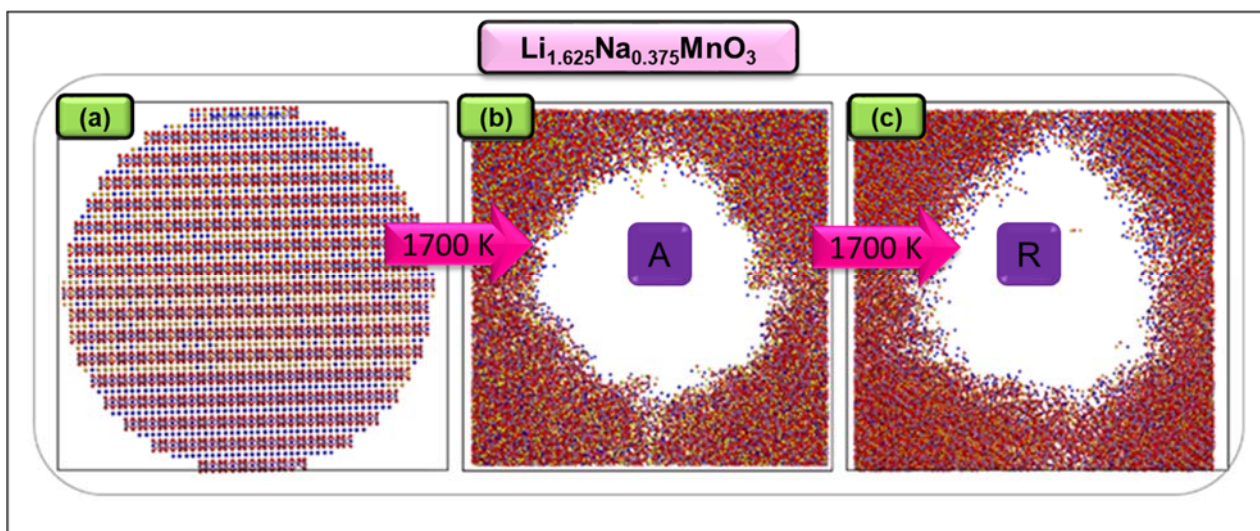
Figure 5.6: Molecular graphics for the Na-substituted $Li_{1.625}Na_{0.375}MnO_3$ showing (a) nanocluster, (b) amorphous configuration and (c) recrystallised configuration carried out at 1700K.

Structural analysis for the amorphisation and recrystallisation of (i) $Li_{1.75}Na_{0.25}MnO_3$, (ii) $Li_{1.975}Na_{0.025}MnO_3$ and (iii) $Li_{1.95}Na_{0.05}MnO_3$ concentrations is illustrated in figure 5.7 below. In (i) the perfect crystalline $Li_{1.75}Na_{0.25}MnO_3$ model in (a) was successfully amorphised at 1700 K, under the NVE ensemble. Recrystallisation was also achieved at the same temperature (1700 K) under the NVT ensemble. Figure (ii) indicates the $Li_{1.95}Na_{0.05}MnO_3$ concentration in which the perfectly ordered $Li_{1.95}Na_{0.05}MnO_3$ configuration before the A+R process is represented by (a). Amorphisation and recrystallisation calculations were successfully carried out at 1700 K as signified by the loss in patterns from (b) and the re-appearing of patterns upon recrystallisation in (c). The $Li_{1.75}Na_{0.25}MnO_3$ concentration depicted in (iii) crystallised into a multi-grained structure as indicated by the presence of grain boundaries (yellow dotted line) in (c). Again, amorphisation and recrystallisation were achieved at 1700 K.
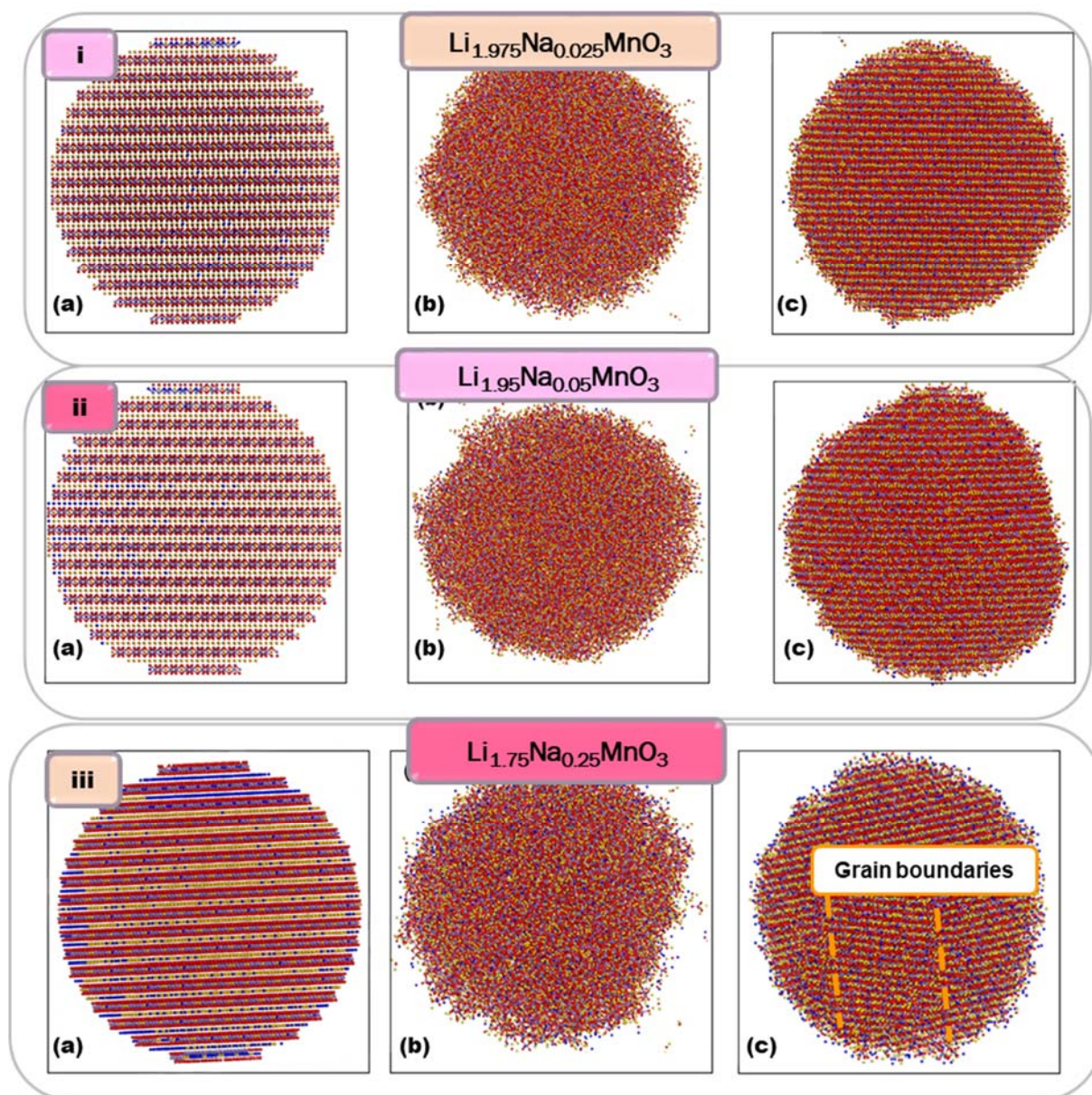
Figure 5.7: Molecular graphics for the (i) Li₁.₉₇₅Na₀.₀₂₅MnO₃, (ii) Li₁.₉₅Na₀.₀₅MnO₃ and (iii) Li₁.₇₅Na₀.₂₅MnO₃ indicating the (a) perfectly packed crystalline, (b) amorphous and (c) recrystallised configurations.

5.3.2. X-Ray Diffraction Patterns (XRDs)

Figure 5.8 illustrates the calculated XRD patterns for the pristine Li_2MnO_3 (a), compared with XRD patterns for the $Li_{2-x}Na_xMnO_3$ concentrations ($Li_{1.975}Na_{0.025}MnO_3$, (b) $Li_{1.95}Na_{0.05}MnO_3$ and (c) $Li_{1.75}Na_{0.25}MnO_3$) in the order of increasing Na content. All the diffraction peaks for the Na-incorporated systems can be indexed to the layered Li_2MnO_3 with no formation of new peaks. The diffraction peaks associated with the ordering of the Li/Mn ions in the transitional metal layers ($2\Theta\sim18\text{-}35°$) are broader,

indicating the disorderly arrangement of the ions. However, for the $Li_{1.95}Na_{0.05}MnO_3$ concentration, a superlattice peak was observed at approximately $2\Theta \sim 15\text{-}22°$ suggesting that the Li/Mn in this system are orderly arranged [5] Contrarily, the $Li_{1.75}Na_{0.25}MnO_3$ with high Na content exhibits weak diffraction peaks at lower angles indicating that the entrance of Na ions destroys the local ordered distribution of the Li/Mn in the transition metal layers [86]. A slight shift to lower angles for the peak at approximately $2\Theta \sim 38°$ was more evidenced for the $Li_{1.95}Na_{0.05}MnO_3$ system signifying the widening of the Li_2MnO_3 lattice as Na ions were introduced into the systems. The same peak $(2\Theta \sim 38°)$ splits into two peaks for the $Li_{2-x}Na_xMnO_3$ systems, suggesting that the structures are more crystalline than the pristine Li_2MnO_3 structure [86, 87].
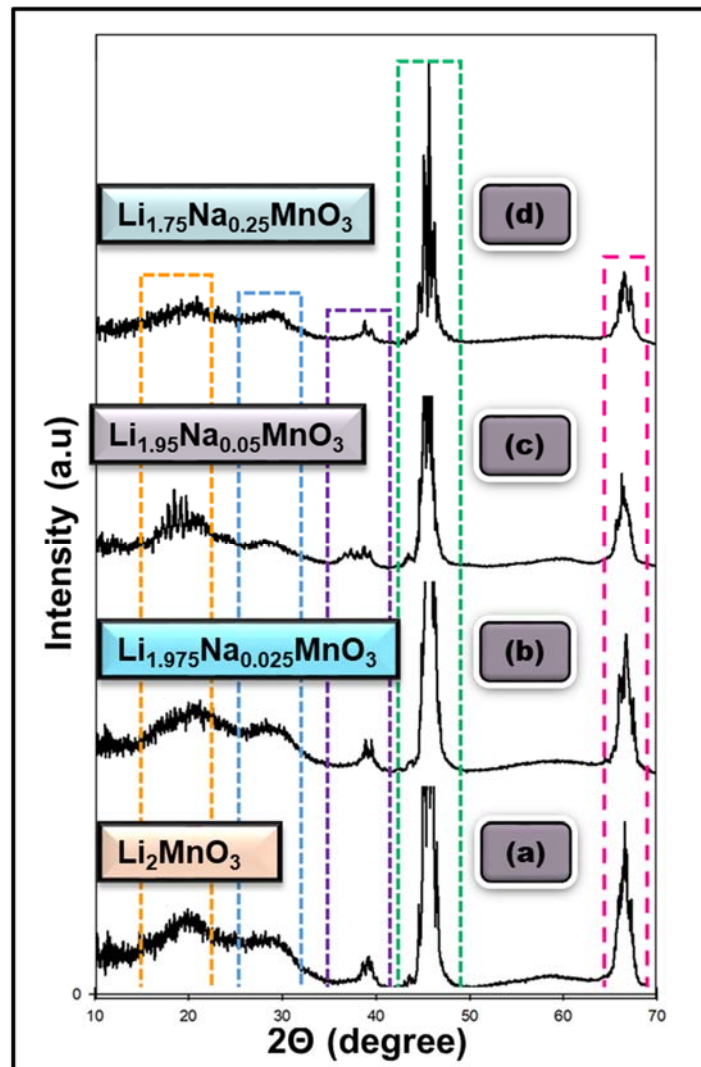
Figure 5.8: Simulated XRD plots for (a) Li₂MnO₃ compared with the Na-incorporated (b) Li₁.₉₇₅Na₀.₀₂₅MnO₃, (c) Li₁.₉₅Na₀.₀₅MnO₃ and (d) Li₁.₇₅Na₀.₂₅MnO₃.

5.3.3. Diffusion Coefficient

The diffusion coefficient plots of Li ions, calculated at different temperatures and concentrations ($Li_{2-x}Na_xMnO_3$) are illustrated in figure 5.9. The $Li_{1.975}Na_{0.025}MnO_3$ (red) system diffuses better than the rest of the other systems. Accordingly, diffusion for this system starts from 100 K and increases to approximately $3.6 \times 10^{-9} m^2.s^{-1}$ at 200 K, the diffusion coefficient then drops to $1 \times 10^{-9} m^2.s^{-1}$ at 300 K and continues increasing exponentially until 1000 K reaching a diffusion coefficient value of approximately $5.9 \times 10^{-9} m^2.s^{-1}$. The $Li_{1.75}Na_{0.25}MnO_3$ (green) system also starts diffusing from 100 K and linearly increases as the temperature of the system was elevated. For the $Li_{1.95}Na_{0.05}MnO_3$ system, the diffusion coefficient graph fluctuates at temperatures 300 and 600 K. Finally, the pristine Li_2MnO_3 (black) exhibited poor Li-ion diffusion kinetics in comparison with the Na incorporated $Li_{2-x}Na_xMnO_3$ systems. Again, for this system (Li_2MnO_3), there was a diffusion coefficient fluctuation at temperatures between 400-600 K.
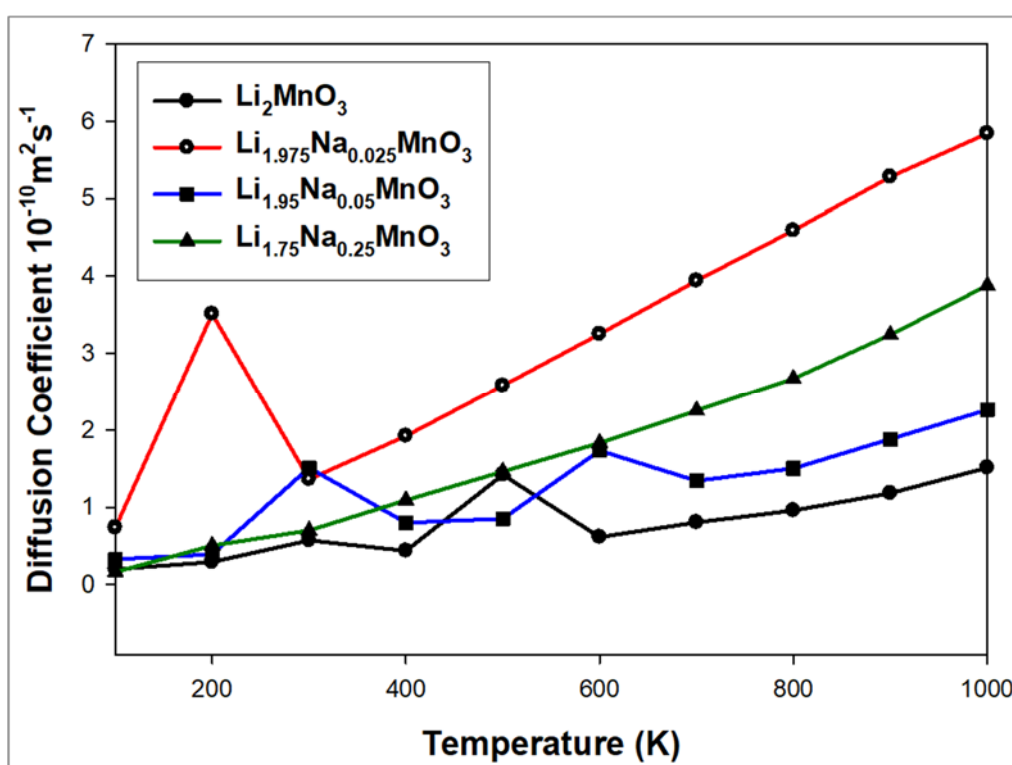
Figure 5.9: Diffusion coefficient plots illustrating the Li₂MnO₃ (black), Li₁.₉₇₅Na₀.₀₂₅MnO₃ (red), Li₁.₉₅Na₀.₀₅MnO₃ (black) and Li₁.₇₅Na₀.₂₅MnO₃ (green) systems.

67

5.4. Summary

The amorphisation and recrystallisation strategy was used to simulate the synthesis of Na-incorporated $Li_{2-x}Na_xMnO_3$ ($0 \leq x \leq 2$) nanospheres from the pristine Li_2MnO_3 configuration. Amorphisation of the Na-doped systems was carried out at temperatures between 1600 -1800 K, depending on the amount of sodium incorporated within the systems. Structural characterisation during the amorphisation of Na_2MnO_3, $Li_{0.50}Na_{1.50}MnO_3$ and $Li_{1.00}Na_{1.00}MnO_3$ involving a high concentration of sodium, revealed structural distortion. Accordingly, the structures transformed from their original spherical to rod-like shapes and this also affected the recrystallisation process. These findings suggest that doping a large amount of sodium into the Li_2MnO_3 results in unstable structures and possibly lattice shrinkage which negatively affects the Li-ion diffusion and capacity of the host material during the cycling process [19, 86]. The $Li_{1.50}Na_{0.50}MnO_3$ system managed to amorphise and recrystallise while maintaining the spherical shape and the RDF plots thereof validated amorphisation through the presence of broader peaks and recrystallisation through increased sharp peaks. Similarly, the $Li_{1.975}Na_{0.025}MnO_3$, $Li_{1.95}Na_{0.05}MnO_3$ and $Li_{1.75}Na_{0.25}MnO_3$ systems recrystallised into spherical configurations with the grain boundaries evolving for the $Li_{1.75}Na_{0.25}MnO_3$ system. However, the $Li_{1.625}Na_{0.375}MnO_3$ system exhibit a distinctive character as the spherical shape transformed into a porous material that managed to recrystallise retaining the porous structure at 1700 K. Characterization of the XRD revealed peak broadening and also the shifting to lower angles of the $2\Theta \sim 38^\circ$ due to the increase in the size of the Li lattice upon Na entrance. The same characteristic peak forms a doublet which indicates that the generated models are of high crystallinity. The presence of Na has also improved the Li/Mn arrangement in the transition metal layers, especially for the $Li_{1.95}Na_{0.05}MnO_3$ concentration which depicted sharp peaks at $2\Theta \sim 15\text{-}22^\circ$. A similar concentration of $Li_{1.90}Na_{0.10}MnO_3$ obtained through a solid-state reaction significantly improved the cycling stability of the layered Li_2MnO_3 host material [80]. The introduction of Na ions into the Li_2MnO_3 lattice has improved the Li-ion diffusion because of the enlarged Li-layers allowing for smooth Li-ion mobility. The Na substituted systems have shown both improved and degraded structures depending on the amount of sodium introduced and also the temperature at which the A+R was carried out.

Chapter 6

Exploration of Sodium-Ion Substitution During the Extraction of Lithium and Oxygen

6.1. Introduction

This chapter details the effect of Li/O extraction on sodium substituted systems, $Li_{2-x}Na_xMnO_3$ ($0 \leq x \leq 2$) generated from the previous chapter. Accordingly, three systems i.e. $Li_{1.75}Na_{0.25}MnO_3$ (12.5 % Na), $Li_{1.95}Na_{0.05}MnO_3$ (2.5 % Na) and $Li_{1.975}Na_{0.025}MnO_3$ (1.25 % Na) will be considered in order to have a broader understanding of how the amount of sodium incorporated on the layered Li_2MnO_3 structure affects its structural and electrochemical performance during the simulated charging process. The charging process will be carried out similarly to Chapter 4, where both Li^+ and O^- will be concurrently removed to study the electrochemical properties of these materials at different concentrations. Characterisation of these structures will be carried out by plotting the RDFs to confirm amorphisation and recrystallisation by analysing the Mn-O pair distribution peaks and how they are affected throughout the charging process. To uncover the internal microstructural features possessed by the respective structures upon Li/O removal, their microstructures will be investigated. The XRD will be analysed to discover the morphologies that may have evolved during the cycling process. Finally, the diffusion coefficient will be evaluated as an electrochemical performance factor that will help diagnose the severity of oxygen loss during the cycling process of the $Li_{2-x}Na_xMnO_3$ materials.

6.2. Method

The charging of the $Li_{2-x}Na_xMnO_3$ systems was carried out through the removal of both the Li^+ and O^- ions via the Material Studio interphase, a process that was implemented in chapter 4, during the charging of Li_2MnO_3 nanostructures. Accordingly, the $Li_{2-x}Na_xMnO_3$ amorphous nanospheres were placed in a cell, where Li^+ and O^- ions were randomly extracted from the outer surfaces with oxygen charge compensated. The irregular removal of Li/O ions resulted in a large number of ions scattered at the $Li_{2-x}Na_xMnO_3$ surfaces, making recrystallisation calculations implausible. A brief MD calculation to re-amorphise the systems in an attempt to relax the disturbed ions was carried out for 0.001 ps and 1000 steps, with the temperature set to 1700 K under the

NVE ensemble. Recrystallisation of the amorphous $Li_{2-x}Na_xMnO_3$ nanostructures was achieved by carrying out an MD calculation with the following conditions: 1700 K, five million steps and 0.003 ps time steps under the NVT ensemble. The resulting structures were then allowed to cool systematically by decreasing the temperature from 1700 K to 5 K, to ensure low energy structure for accurate structural diagnosis.

6.3. Results

6.3.1. Radial Distribution Functions (RDFs)

The Mn-O pair distribution plots for the $Li_{1.75}Na_{0.25}MnO_3$ system during Li/O extraction are shown in figure 6.1. In (a) $Li_{1.50}Na_{0.25}MnO_{2.75}$ (black), $Li_{1.25}Na_{0.25}MnO_{2.50}$ (red), $Li_{1.00}Na_{0.25}MnO_{2.25}$ (blue) and $Li_{0.75}Na_{0.25}MnO_{2.00}$ (pink), the amorphous configurations depict broader peaks for all the concentrations. A sharp peak is observed at approximately 1.9 Å, corresponding to the Mn-O bond length which is comparable to the 1.92 Å in literature [88]. The peaks beyond 5 Å are very broad confirming the minimal probability of locating the nearest neighbouring atom within the radial distance r. A magnified portion from (a) is depicted in (b) to better view the arrangement of the peak and confirm the amorphous state of the systems.

In figure 6.1 (c), the recrystallised RDFs for the charged $Li_{1.75}Na_{0.25}MnO_3$ with varying Li concentrations are depicted, showing a slight increase in the number of sharp peaks with increased intensity. A section from (c) was magnified in (d) for better analysis of the peaks from 3 -10 Å, and the $Li_{1.50}Na_{0.25}MnO_{2.75}$ system is more crystalline since it exhibits more sharp peaks. As charging progresses, the peaks become broader, especially for peaks beyond 5 Å. The charged $Li_{0.75}Na_{0.25}MnO_2$ (green) exhibits broader peaks from 3 Å and intensifies for peaks beyond 5 Å. This may be as a result of the formation of O^- vacancies and also the migration of Mn-ions into the tetrahedral sites as Li/O content was varied. It was also noted that the peak intensity from amorphous to recrystallised configurations partially increased, suggesting that as charging progressed, some regions within the structures may have transformed back to amorphous configurations as a result of excessive defects [89].
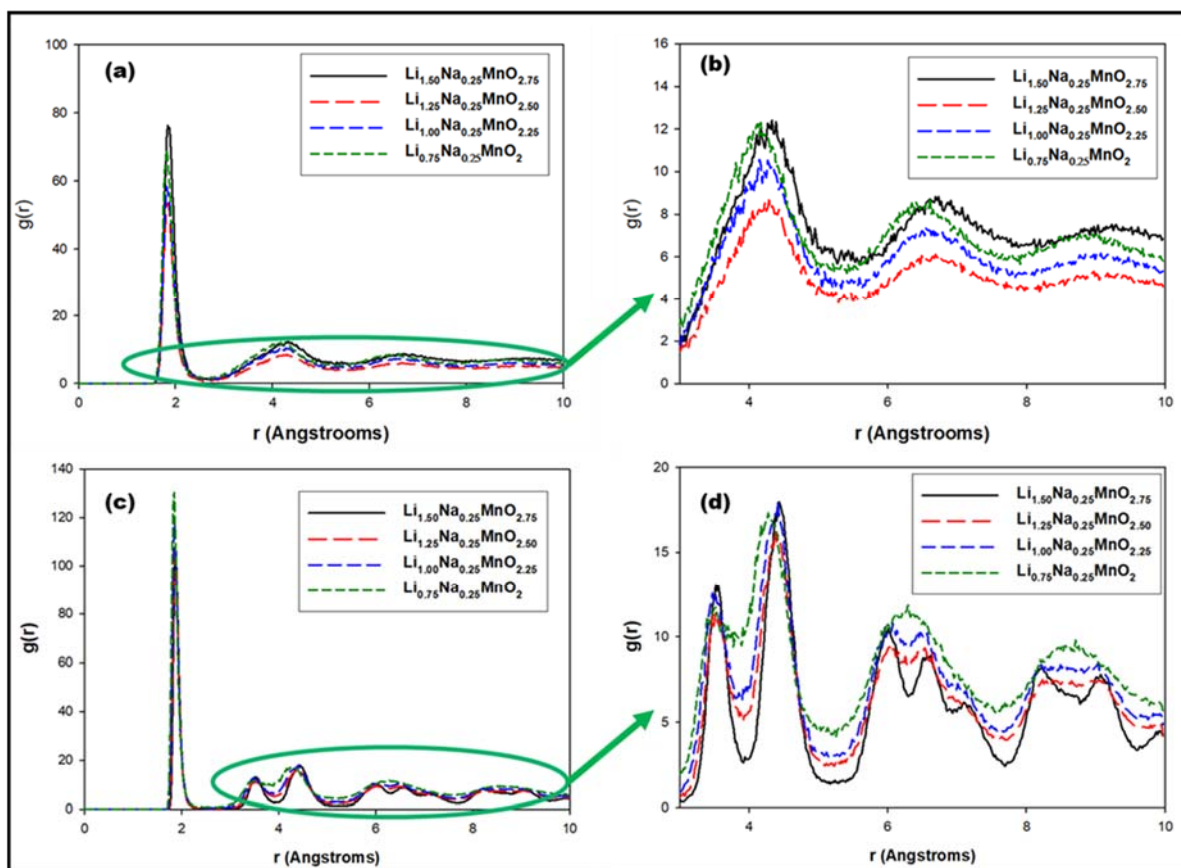
Figure 6.1: Mn-O pair distribution for the $Li_{1.75}Na_{0.25}MnO_3$ structure during the concurrent removal of Li and O, before (a.b) and after (c.d) recrystallisation, where $Li_{1.50}Na_{0.25}MnO_{2.75}$, $Li_{1.25}Na_{0.25}MnO_{2.50}$, $Li_{1.00}Na_{0.25}MnO_{2.25}$, and $Li_{0.75}Na_{0.25}MnO_{2.00}$ systems are illustrated by black, red, blue and pink plots respectfully.

In relation to the $Li_{1.95}Na_{0.05}MnO_3$ system, the RDFs are shown in figure 6.2, representing the amorphous and recrystallised plots during the removal of Li/O where $Li_{1.70}Na_{0.05}MnO_{2.75}$, $Li_{1.45}Na_{0.05}MnO_{2.5}$, $Li_{1.20}Na_{0.05}MnO_{2.25}$ and $Li_{0.95}Na_{0.05}MnO_{2.00}$ are detailed by black, red, blue and pink trace. The amorphous configurations in (a), depict broader peaks as an indication of weak Mn-O bonds, and (b) is the magnified portion of (a), revealing peak broadening. In (c), sharp peaks with increased intensity as a result of strong Mn-O bonds are observed from the recrystallised RDFs for the $Li_{1.95}Na_{0.05}MnO_3$ system. The magnified portion of (c), depicted in (d) reveals that the charged $Li_{1.45}Na_{0.05}MnO_{2.50}$ system is more crystalline, followed by the $Li_{1.70}Na_{0.05}MnO_{2.75}$ and then the $Li_{1.20}Na_{0.05}MnO_{2.25}$ system. The last concentration ($Li_{0.95}Na_{0.05}MnO_{2.00}$) exhibits broader peaks with low intensity as Li/O extraction was carried out, also indicating a high concentration of defects.
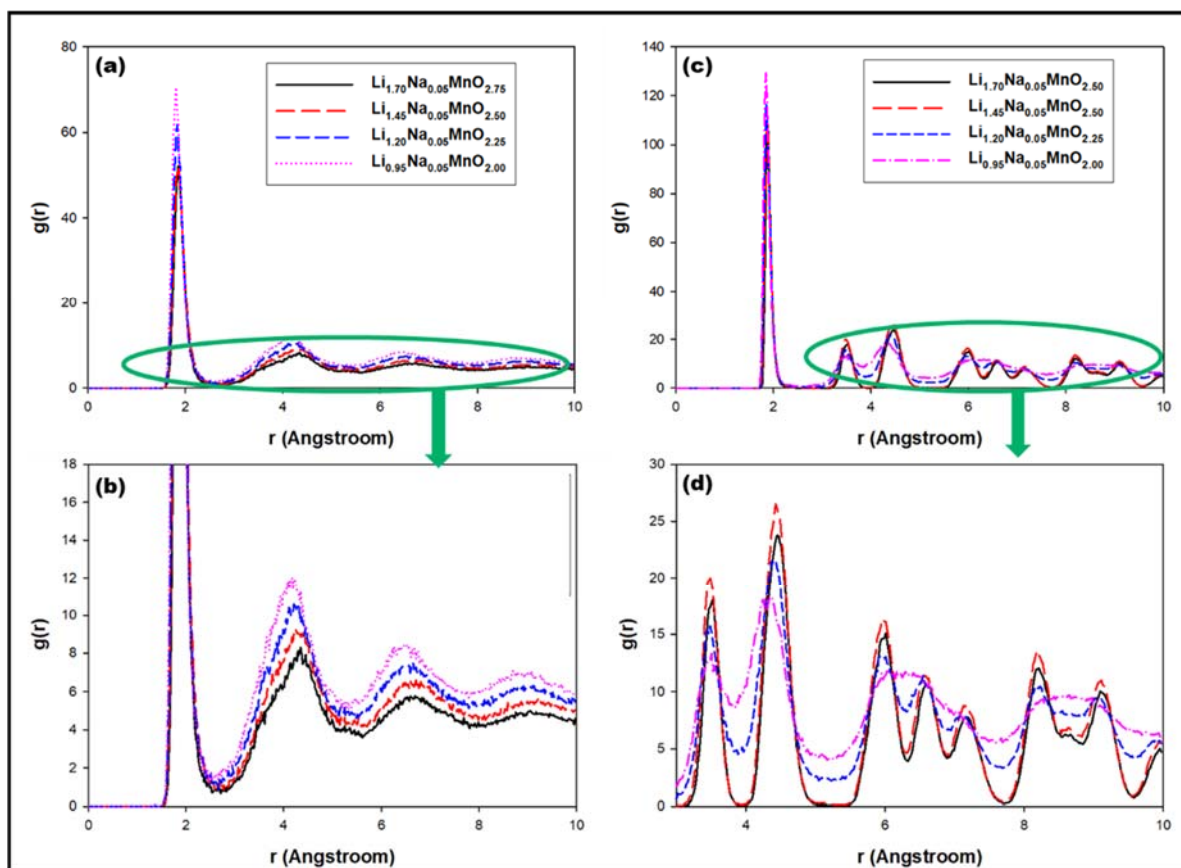
Figure 6.2: Radial distribution functions (Mn-O) for the $Li_{1.95}Na_{0.05}MnO_3$ configuration during the removal of Li/O, before (a.b) and after (c.d) recrystallisation, where $Li_{1.70}Na_{0.05}MnO_{2.75}$, $Li_{1.45}Na_{0.05}MnO_{2.50}$, $Li_{1.20}Na_{0.05}MnO_{2.25}$ and $Li_{0.95}Na_{0.05}MnO_{2.00}$ graphs are depicted by black, red, blue and pink trace.

The RDF plots for the $Li_{1.975}Na_{0.025}MnO_3$ configuration during the extraction of Li/O content are illustrated in figure 6.3 below. In (a), the peaks are broader indicating that all the systems i.e. $Li_{1.725}Na_{0.025}MnO_{2.75}$ (black), $Li_{1.475}Na_{0.025}MnO_{2.50}$ (red), $Li_{1.225}Na_{0.025}MnO_{2.25}$ (blue) and $Li_{0.995}Na_{0.025}MnO_{2.00}$ (pink) are in their amorphous states. The magnified portion of (a), illustrated in (b) confirms that all systems are in their amorphous state.

During recrystallisation, sharp peaks emerged as shown in (c). The graph's intensity has also doubled due to the high probability of locating the nearest neighbouring atom within the radial distance. It is evident from (d), a magnified portion of (c) that the $Li_{1.475}Na_{0.025}MnO_{2.50}$ is more crystalline, followed by the $Li_{1.75}Na_{0.025}MnO_{2.75}$ system. Moreover, the $Li_{1.225}Na_{0.025}MnO_{2.25}$ and $Li_{0.995}Na_{0.025}MnO_{2.00}$ systems with low Li/O content exhibit broader peaks with low intensity.
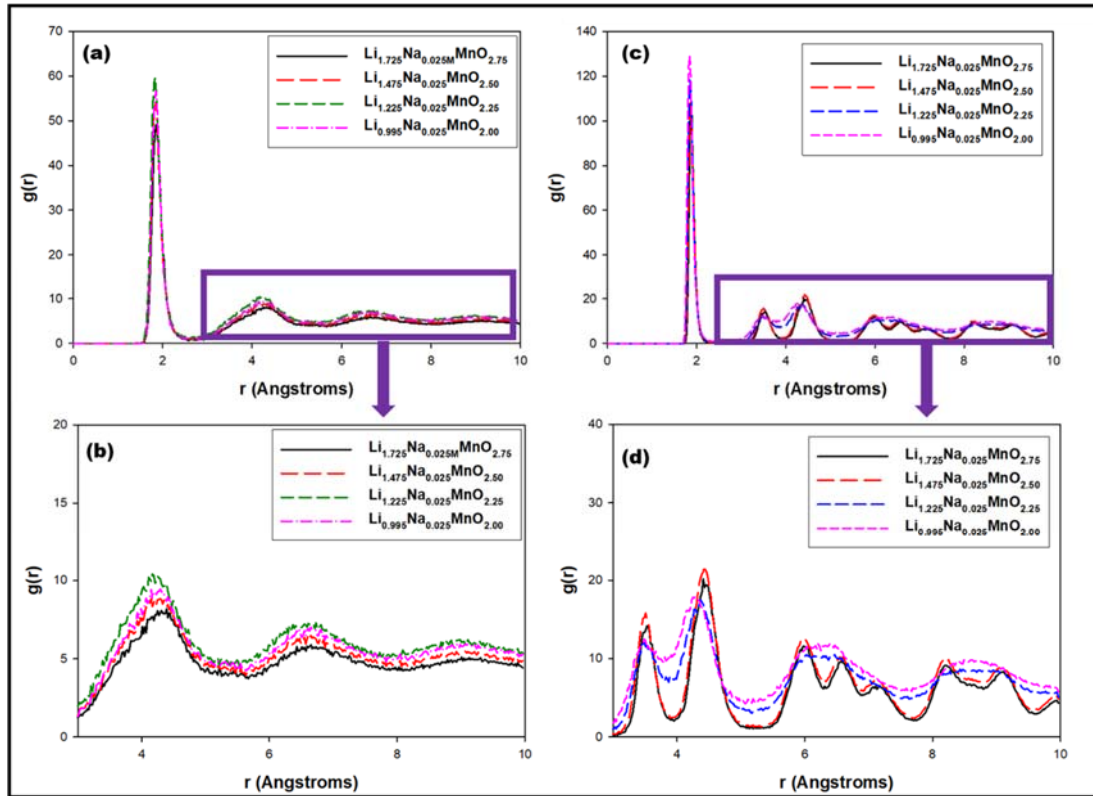
Figure 6.3: RDF graphs (Mn-O) for the Li$_{1.975}$Na$_{0.025}$MnO$_3$ configuration during the removal of Li/O, before (a.b) and after (c.d) recrystallisation, where Li$_{1.70}$Na$_{0.05}$MnO$_{2.75}$, Li$_{1.45}$Na$_{0.05}$MnO$_{2.5}$, Li$_{1.20}$Na$_{0.05}$MnO$_{2.25}$ and Li$_{0.95}$Na$_{0.05}$MnO$_{2.00}$ systems are depicted by black, red, blue and pink trace.

6.3.2. Atomistic Models

Molecular graphics for the recrystallised (i) Li$_{1.75}$Na$_{0.25}$MnO$_3$, (ii) Li$_{1.975}$Na$_{0.025}$MnO$_3$ and (iii) Li$_{1.95}$Na$_{0.25}$MnO$_3$ configurations, during Li/O extraction, are depicted in figure 6.4 respectively. In figure 6.4 (i), charging resulted in structures comprising grain boundaries. These grain boundaries evolved from the initial stage of Li/O removal i.e. Li$_{1.50}$Na$_{0.25}$MnO$_{2.75}$ and increased with a decrease in Li/O content. This is the same system that depicted broader RDFs, confirming the loss in crystal arrangement during charging.

The charging of the Li$_{1.975}$Na$_{0.025}$MnO$_3$ system depicted in (ii) also reveals the presence of grain boundaries as indicated by the orange dotted lines. Again, as the Li/O content decreased, more grain boundaries evolved especially for the charged Li$_{1.225}$Na$_{0.025}$MnO$_{2.25}$ and Li$_{1.995}$Na$_{0.025}$MnO$_{2.00}$ systems. In (iii), the first two systems (Li$_{1.70}$Na$_{0.05}$MnO$_{2.75}$, Li$_{1.45}$Na$_{0.05}$MnO$_{2.50}$) display no grain boundaries, however, as charging progressed, grain boundaries evolved for the Li$_{1.20}$Na$_{0.05}$MnO$_{2.25}$ and Li$_{0.95}$Na$_{0.05}$MnO$_{2.00}$ systems with low Li/O content.
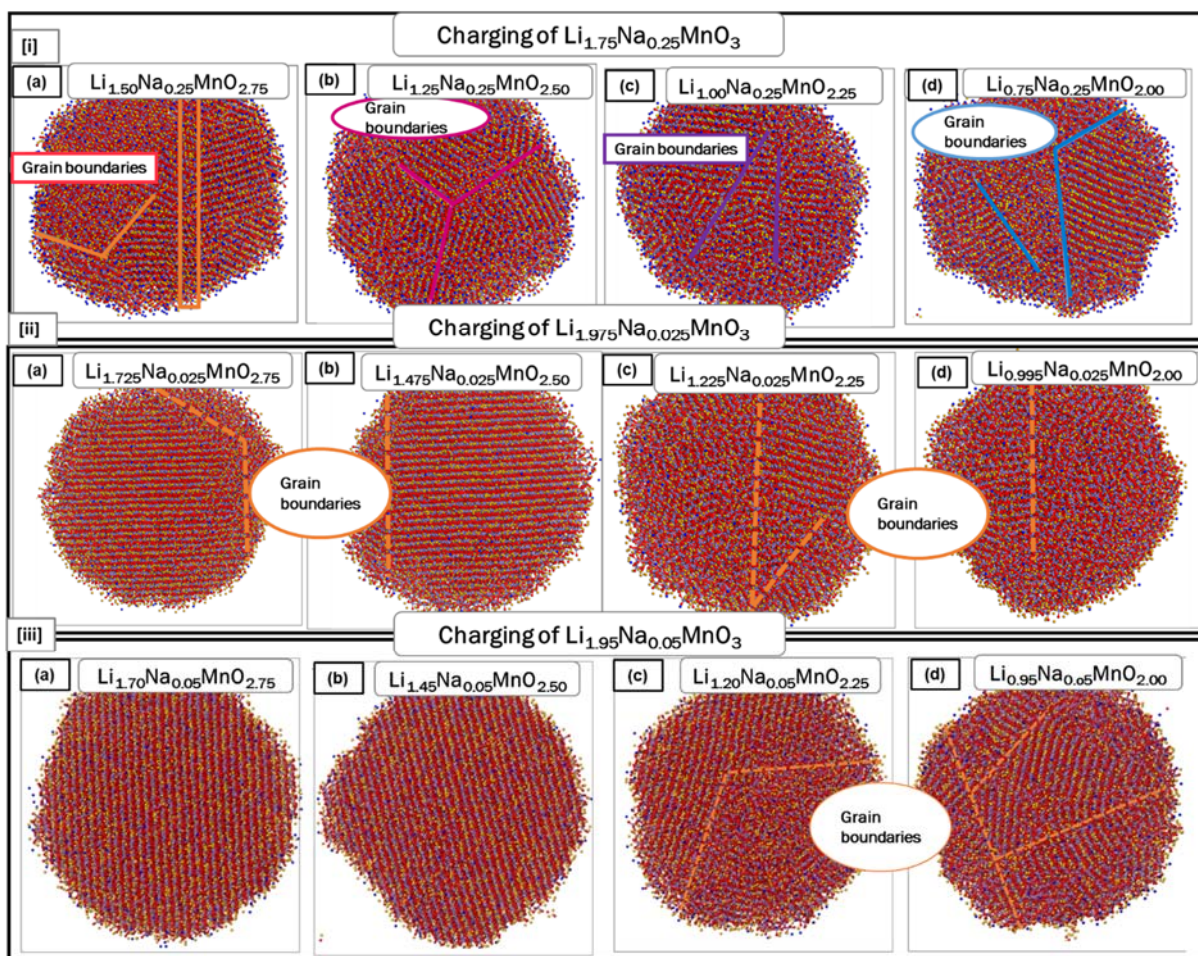
Figure 6.4: Recrystallised sodium incorporated atomistic models during the removal of Li/O, indicating the $Li_{1.75}Na_{0.05}MnO_3$ (i), $Li_{1.975}Na_{0.025}MnO_3$ (ii) and $Li_{1.95}Na_{0.25}MnO_3$ (iii) systems.

6.3.3. X-Ray Diffraction Patterns (XRDs)

The XRD plots calculated during the charging of $Li_{1.75}Na_{0.25}MnO_3$ are presented in figure 6.5, where the $Li_{1.75}Na_{0.25}MnO_3$ (a) diffraction peaks before Li/O removal are superimposed with charged $Li_{1.50}Na_{0.25}MnO_{2.75}$ (b) $Li_{1.25}Na_{0.25}MnO_{2.50}$ (c) $Li_{1.00}Na_{0.25}MnO_{2.25}$ (d) and $Li_{0.75}Na_{0.25}MnO_{2.00}$ (e) diffraction peaks. Upon Li/O removal, the systems exhibit extensive broadening of peaks with some peaks drastically decreasing in intensity. Emerging peaks at approximately $2\Theta \sim 18\text{-}35°$ increases for the $Li_{1.50}Na_{0.25}MnO_{2.7}$ and $Li_{1.25}Na_{0.25}MnO_{2.50}$ systems and significantly decreases for $Li_{1.00}Na_{0.25}MnO_{2.25}$ and $Li_{0.75}Na_{0.25}MnO_{2.00}$ systems. Also, the peak at $2\Theta \sim 38°$ becomes broad and increases in intensity with a slight shift to the right as a result of sodium ions which enlarges the Li^+ layers. The sharp peak at around $2\Theta \sim 48°$ becomes broad during the first stage of Li/O extraction and slightly decreases for the $Li_{1.25}Na_{0.25}MnO_{2.50}$ system, increases again for $Li_{1.75}Na_{0.25}MnO_3$ and drastically

decreases for the $Li_{0.75}Na_{0.25}MnO_{2.00}$ system. This fluctuation of peaks was also observed for the peak at approximately 2Θ ~ 68.
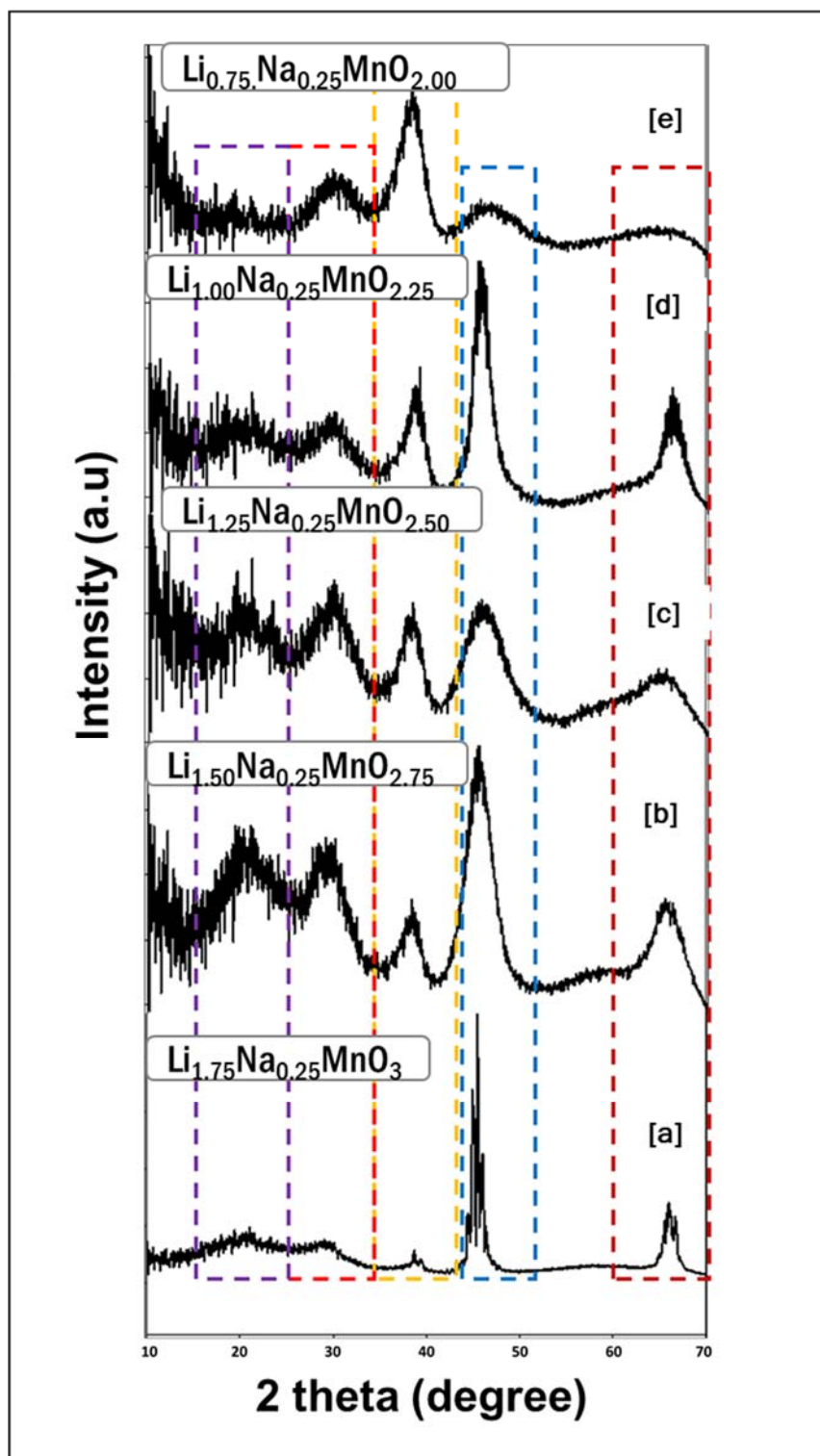
Figure 6.5: XRD plots for the charging of (a) Li₁.₇₅Na₀.₂₅MnO₃, with (b) Li₁.₅₀Na₀.₂₅MnO₂.₇₅, (c) Li₁.₂₅Na₀.₂₅MnO₂.₅₀, (d) Li₁.₀₀Na₀.₂₅MnO₂.₂₅ and Li₀.₇₅Na₀.₂₅MnO₂.₀₀.

Figure 6.6 illustrates XRD graphs for the charging of the $Li_{1.975}Na_{0.025}MnO_3$ (black) system with charged $Li_{1.725}Na_{0.025}MnO_{2.75}$, $Li_{1.475}Na_{0.025}MnO_{2.50}$, $Li_{1.225}Na_{0.025}MnO_{2.25}$ and $Li_{0.975}Na_{0.025}MnO_{2.00}$ configurations indicated by black, red, blue, pink and green traces. Again, Li/O leaching resulted in the broadening of peaks. The peaks associated with Li/Mn ordering in the transitional metal layers ($2\Theta \sim 18\text{-} 25^o$) and the peak at $2\Theta \sim 25\text{-} 35^o$ grow along with decreasing Li/O content. At $2\Theta \sim 38^o$, the shifting to the right is also evident and the peak monotonously increases in intensity. The peak at $2\Theta \sim 48^o$ increases in intensity but decreases for low Li/O content i.e. $Li_{1.225}Na_{0.025}MnO_{2.25}$, and $Li_{0.975}Na_{0.025}MnO_{2.00}$. The same was observed for the peak at approximately $2\Theta \sim 68^o$.
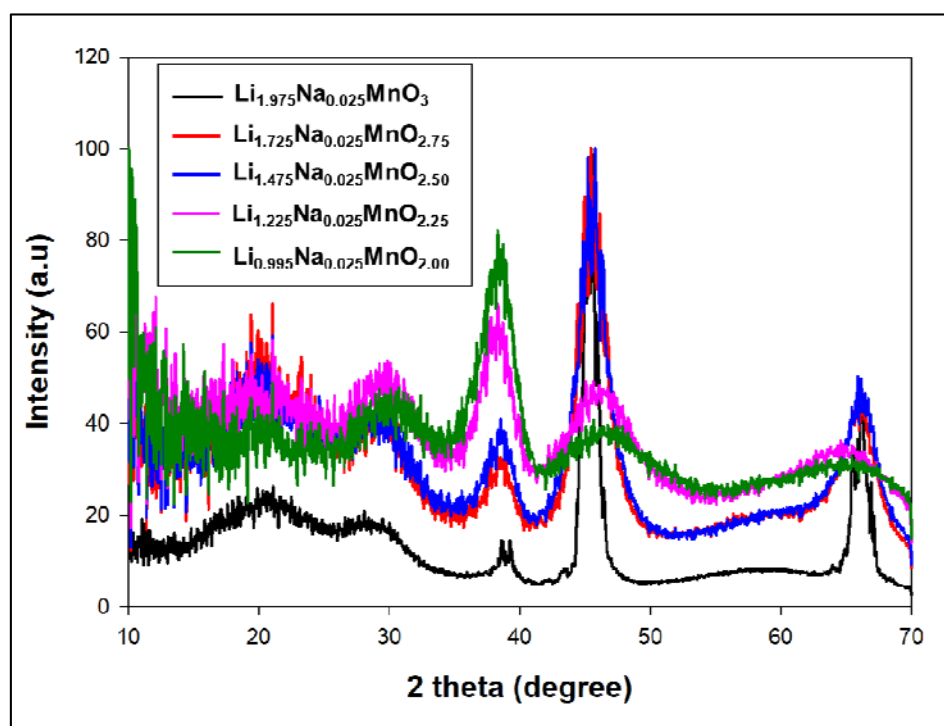
Figure 6.6: Diffraction peaks for the charging of $Li_{1.975}Na_{0.025}MnO_3$ (black), showing $Li_{1.725}Na_{0.025}MnO_{2.75}$ (red), $Li_{1.475}Na_{0.25}MnO_{2.50}$ (blue), $Li_{1.225}Na_{0.025}MnO_{2.25}$ (pink) (d) $Li_{0.995}Na_{0.25}MnO_{2.00}$ (green) plots.

A comparison of the diffraction peaks of the $Li_{1.95}Na_{0.05}MnO_3$ (black) system before and after Li/O extraction i.e. $Li_{1.70}Na_{0.05}MnO_{2.75}$ (red), $Li_{1.45}Na_{0.05}MnO_{2.50}$ (blue), $Li_{1.20}Na_{0.05}MnO_{2.25}$ (pink) and $Li_{0.95}Na_{0.05}MnO_{2.00}$ (green) is depicted in figure 6.7 below. The graphs indicate that the diffraction peaks increase along with decreasing Li/O, with the $Li_{1.95}Na_{0.05}MnO_3$ system showing superlattice peaks at lower angles as an indication of well-ordered Li/Mn in transition metal layers. The $Li_{0.95}Na_{0.05}MnO_{2.00}$

diffraction peaks for the system constituting the lowest Li/O exhibit broader peaks with extremely low intensities at $2\Theta \sim 48$ and 68°.
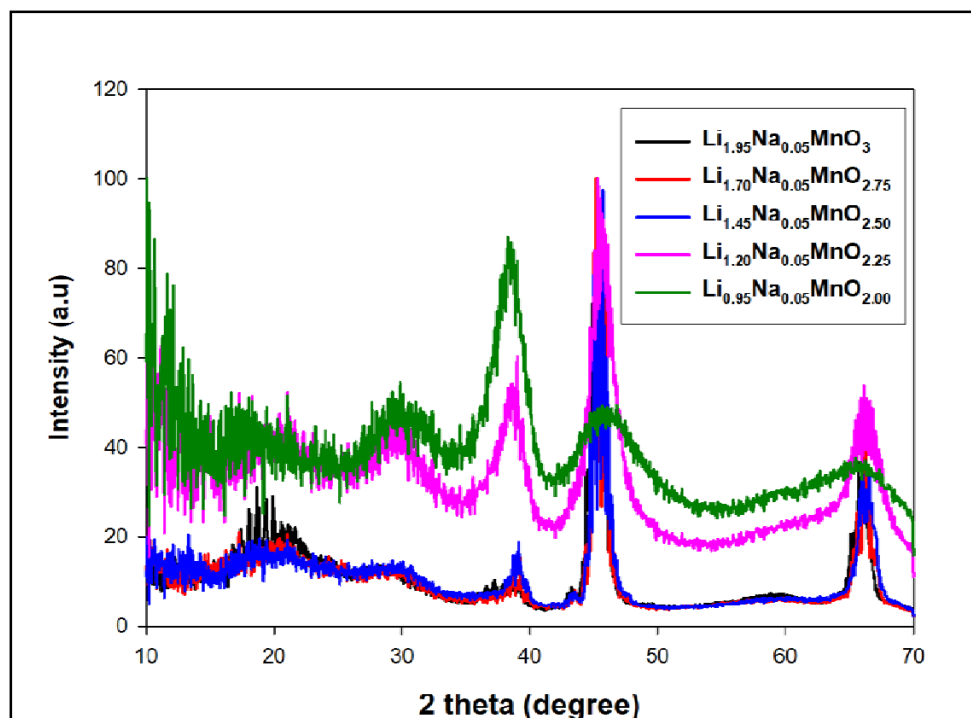
Figure 6.7: XRD graphs for the nano spherical $Li_{1.95}Na_{0.05}MnO_3$ (black), $(Li_{1.70}Na_{0.05}MnO_{2.75}$ (red), $Li_{1.45}Na_{0.05}MnO_{2.50}$ (blue), $Li_{1.20}Na_{0.05}MnO_{2.25}$ (pink), and $Li_{0.95}Na_{0.05}MnO_{2.00}$ (green) during the leaching of Li/O.

The XRD plots for (i) $Li_{1.975}Na_{0.025}MnO_3$ and (ii) $Li_{1.95}Na_{0.05}MnO_3$ are compared with XRDs from the literature to explore phases that may have evolved during the simulated charge. In figure 6.8 (i), the calculated XRDs $Li_{1.975}Na_{0.025}MnO_3$ (a), $Li_{1.725}Na_{0.025}MnO_{2.75}$ (b), $Li_{1.475}Na_{0.025}MnO_{2.50}$ (c), $Li_{1.225}Na_{0.025}MnO_{2.25}$ (d), and $Li_{0.975}Na_{0.025}MnO_{2.00}$ (e) are superimposed with (f) Li_2MnO_3 [74], (g) $LiMn_2O_4$ [75] (h) $LiMnO_2$ and (i) MnO_3 [76] from experiments for comparison. The decline in intensity for the shoulder peak at $2\Theta \sim 18 - 24^\circ$, observed for the $Li_{1.225}Na_{0.025}MnO_{2.25}$ and $Li_{0.975}Na_{0.025}MnO_{2.00}$ systems may be ascribed to the disorientation of Li/Mn in the transition metal layer. An emerging peak at around $2\Theta \sim 29^\circ$ due to the presence of tetrahedral manganese atoms, indicating the growth of the spinel Mn_3O_4 component. The peak at approximately $2\Theta \sim 37^\circ$ increases in intensity as the Li/O content decrease and is associated with the Li_2MnO_3 and $LiMnO_2$. The peak at $2\Theta \sim 48^\circ$ decreases, especially for the last two charged systems and is associated with the spinel phase ($LiMn_2O_4$). The peak at $2\Theta \sim 68^\circ$ also decreases upon Li/O removal and is associated with the Li_2MnO_3, $LiMn_2O_4$ and Mn_3O_4.
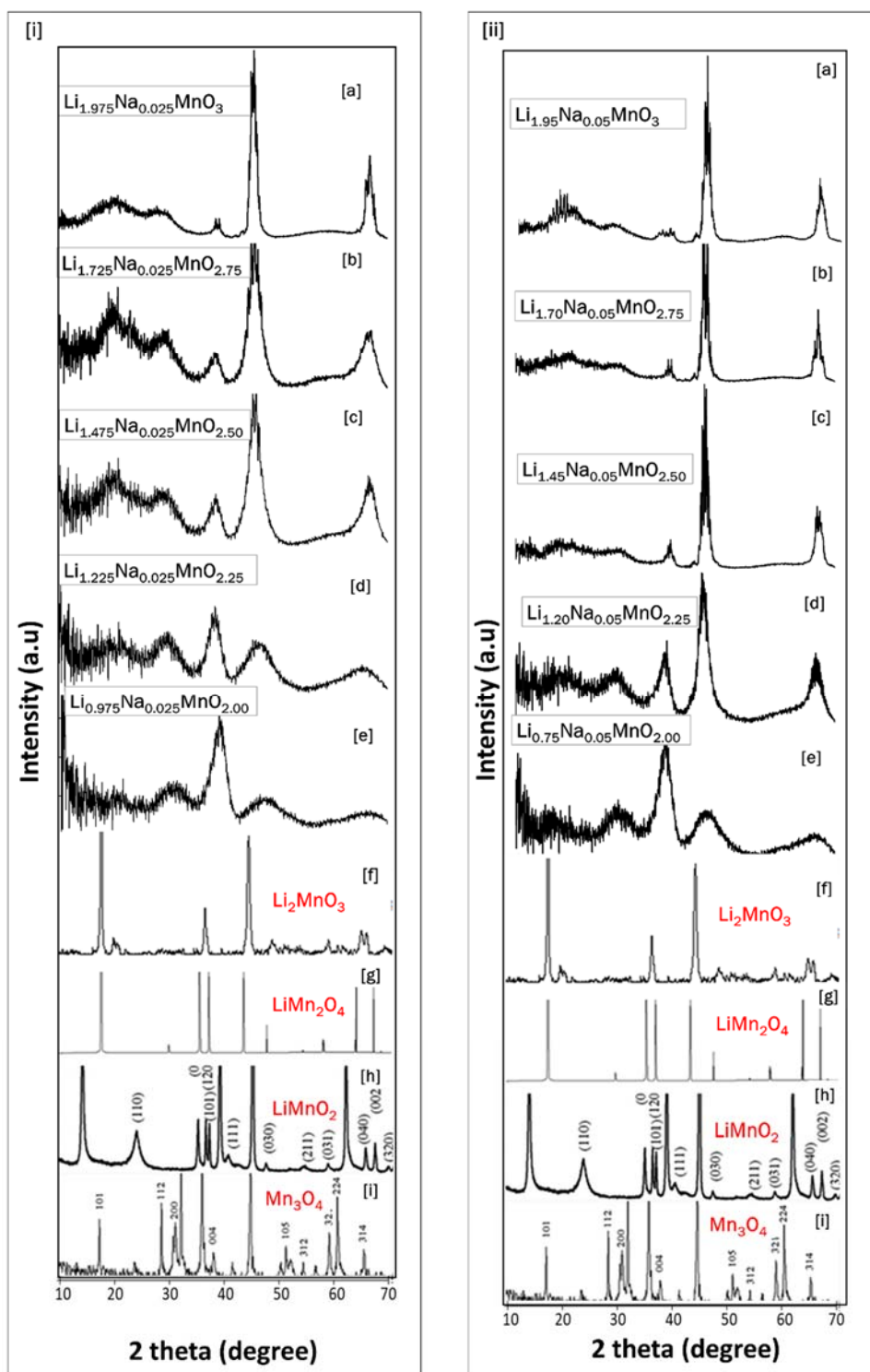
Figure 6.8: [i] XRD plots for Li₁.₉₇₅Na₀.₀₂₅MnO₃ (a), Li₁.₇₂₅Na₀.₀₂₅MnO₂.₇₅ (b) Li₁.₄₇₅Na₀.₀₂₅MnO₂.₅₀, (c) Li₁.₂₂₅Na₀.₀₂₅MnO₂.₂₅ (d) and Li₀.₉₇₅Na₀.₀₂₅MnO₂.₀₀ (e) nanospheres during Li/O removal compared with XRDs for (f) Li₂MnO₃ [80], **(g) LiMn₂O₄** [81], **(h) LiMnO₂ and (i) MnO₃** [82]. **[ii] Calculated XRDs for (a) Li₁.₉₅Na₀.₀₅MnO₃, (b) Li₁.₇₀Na₀.₀₅MnO₂.₇₅, (c) Li₁.₄₅Na₀.₀₅MnO₂.₅₀, (d) Li₁.₂₀Na₀.₀₅MnO₂.₂₅ and (e) Li₀.₇₅Na₀.₀₅MnO₂.₀₀ nanospheres superimposed with Li₂MnO₃ (f)** [80], **LiMn₂O₄ (g)** [81], **LiMnO₂ (h) and (i) MnO₃** [82]**.**

78

Figure 6.8 (ii) above illustrates the calculated diffraction peaks for the uncharged $Li_{1.95}Na_{0.05}MnO_3$ (a), charged $Li_{1.70}Na_{0.05}MnO_{2.75}$ (b), $Li_{1.45}Na_{0.05}MnO_{2.50}$ (c), $Li_{1.20}Na_{0.05}MnO_{2.25}$ (d) and $Li_{0.95}Na_{0.05}MnO_{200}$ (e) systems compared with XRD plots of known morphologies Li_2MnO_3 (f) [80], $LiMn_2O_4$ (g) [81], $LiMnO_2$ (h) and MnO_3 (i) [82]. In comparison to $Li_{1.975}Na_{0.025}MnO_3$ above, the charging of $Li_{1.95}Na_{0.05}MnO_3$ resulted in sharp diffraction peaks suggesting minimized defects and more crystalline structures. Again, emerging peaks were observed at low angles associated with the transition metal layer ordering of the Li/Mn. The MnO_3 spinel phase, depicted by the growth of peak at $2\Theta \sim 29^o$ is more evident for systems comprising low Li/O content i.e. at $Li_{1.20}Na_{0.05}MnO_{2.25}$ and $Li_{0.95}Na_{0.05}MnO_{2.00}$. All diffraction peaks increase with a decrease in Li/O concentration except for the $Li_{0.95}Na_{0.05}MnO_{2.00}$ system which showed extensive reduction peaks at $2\Theta \sim 48$ and 68° associated with the spinel phase.

.

6.3.4. Microstructures

The microstructural details for the $Li_{1.75}Na_{0.25}MnO_3$ system before and after the removal of Li/O are illustrated in figure 6.9. A slice cut-through of the uncharged $Li_{1.75}Na_{0.25}MnO_3$ system is depicted in figure 6.9 (i)(a) revealing the mixing of layers. Though the structure is dominated by defects, there are a few regions still maintaining the Li_2MnO_3 ordering with the presence of vacancies and cation mixing as shown in the magnified portion (b), and compared with the perfect model in (c).

Figure 6.9(ii)(a), represents the slice cut-through charged $Li_{1.50}Na_{0.25}MnO_{2.75}$ and exhibits grain boundaries (green dotted line) and excessive mixing of layers resulting in the formation of the distorted spinel $LiMn_2O_4$ structures as indicated by the magnified segment in (b) and compared with $LiMn_2O_4$ perfect model in (c). Further Li/O removal led to a considerable number of Mn ions occupying vacant Li layers. The $Li_{1.25}Na_{0.25}MnO_{2.50}$ slice cut-through is illustrated in figure 6.9 (iii) (a), and magnified in (b) to show the formation of the layered $LiMnO_2$ component that was comparable to the perfect model $LiMnO_2$ in (c). Another magnified portion of (a), showing the presence of a distorted Li_2MnO_3 component is represented in (d) and compared with its perfect model in (e).
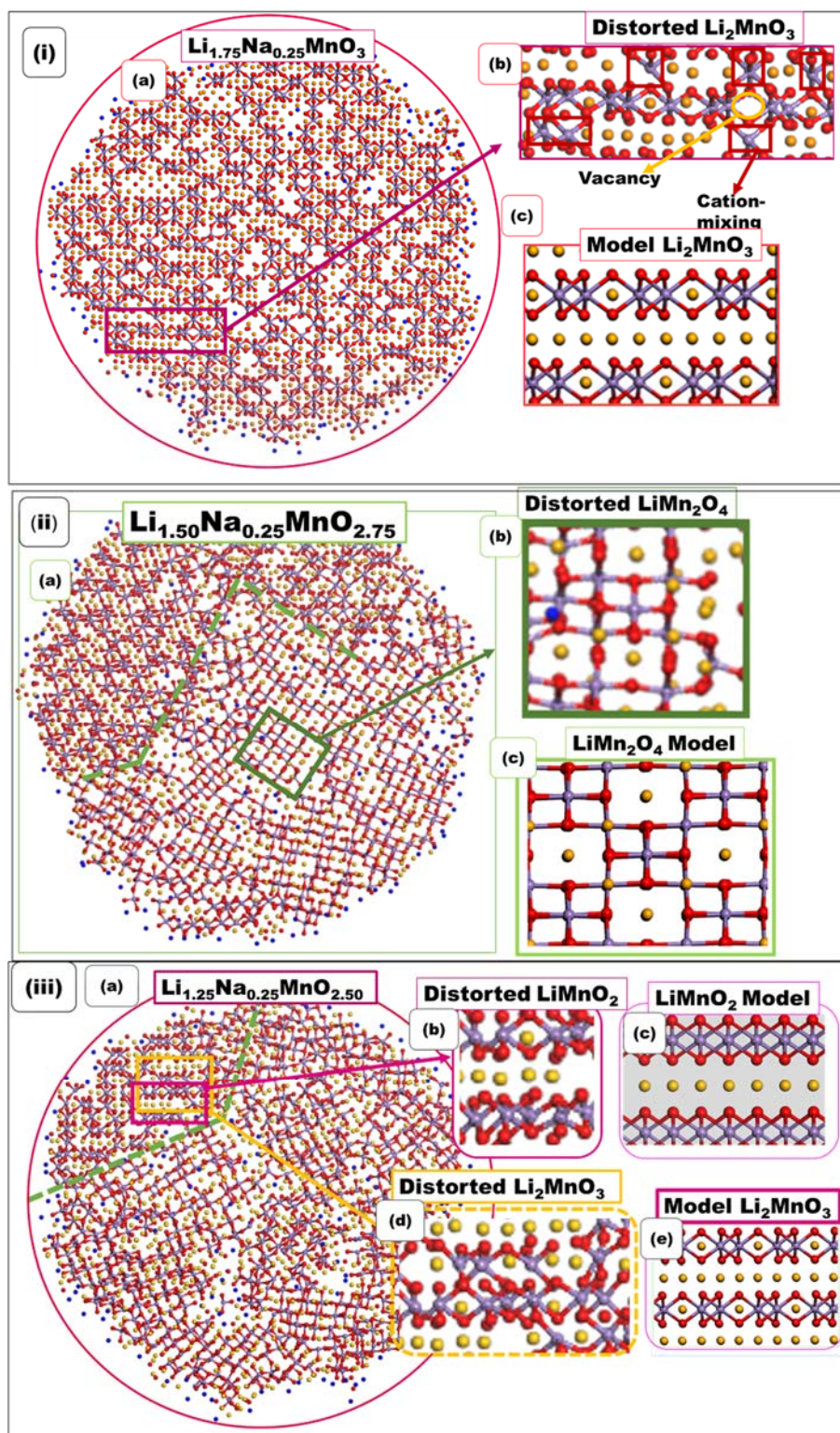
Figure 6.9: [i] (a) *A slice cut-through Li$_{1.75}$Na$_{0.25}$MnO$_{2.75}$, (b) magnified portion from (a) revealing Li$_2$MnO$_3$ component, (c) Li$_2$MnO$_3$ perfect model. [ii] (a) A slice cut-through Li$_{1.50}$Na$_{0.25}$MnO$_{2.75}$, (b) magnified segment from (a) showing LiMn$_2$O$_4$ component compared with (c) perfect LiMn$_2$O$_4$ model. [ii] (a) Li$_{1.50}$Na$_{0.25}$MnO$_{2.75}$ slice (b) magnified distorted LiMnO$_2$ compared with (c) perfect LiMn$_2$O$_4$, (d) magnified Li$_2$MnO$_3$ compared with perfect Li$_2$MnO$_3$ model in (e).*

80

Structural analysis before and after the charging of the $Li_{1.95}Na_{0.05}MnO_3$ is depicted in figure 6.10. In (i) (a), the slice cut-through $Li_{1.95}Na_{0.05}MnO_3$ reveal a large portion of a well-ordered layered Li_2MnO_3, this was maximized in (b) and compared with c, Li_2MnO_3 perfect model. During the first stage of leaching, the ordering of the Li_2MnO_3 is maintained with minimal Mn^+ migration to the Li^+ layers. A slice cut-through $Li_{1.70}Na_{0.05}MnO_{2.75}$ is depicted in (ii) and the portion of the Li_2MnO_3 is magnified in (b) and is comparable to (c), the Li_2MnO_3 perfect model.
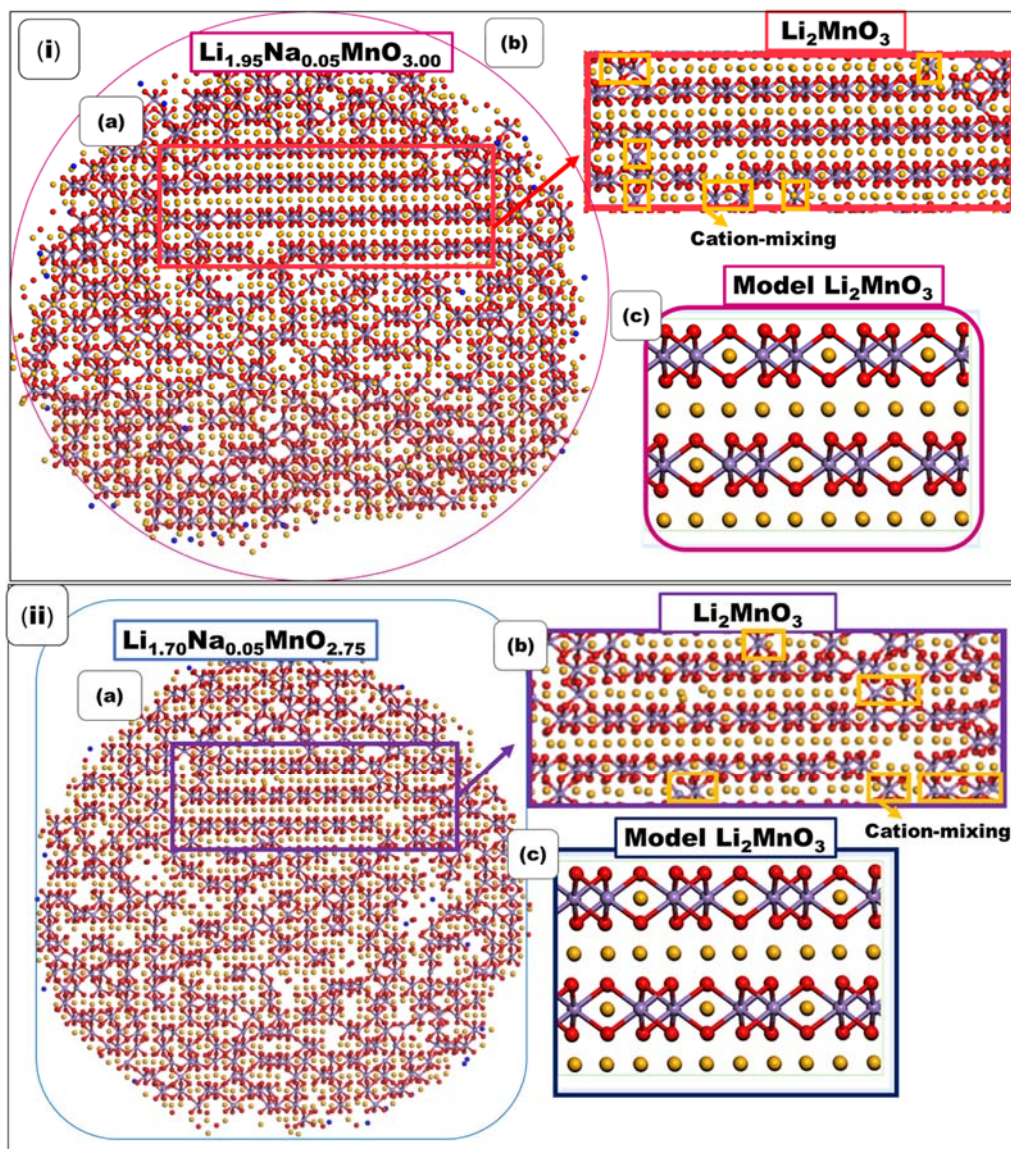
Figure 6.10: [i] (a) A slice cut-through $Li_{1.95}Na_{0.05}MnO_3$, (b) magnified portion from (a) revealing a well-ordered Li_2MnO_3 morphology, (c) Li_2MnO_3 perfect model. [ii] (a) A slice cut-through $Li_{1.70}Na_{0.05}MnO_{2.75}$, (b) magnified portion from (a) showing ordered Li_2MnO_3 morphology, (c) Li_2MnO_3 perfect model.

In figure 6.11 (i), the cut-through $Li_{1.45}Na_{0.05}MnO_{2.50}$ indicated by (a), reveals that at this concentration, the ordering of Li_2MnO_3 observed in figure 6.10 above is lost, and the structure has a significant number of Mn^+ migrating to the tetrahedral sites resulting in most of the layers mixed. Magnified portions from the slice cut-through $Li_{1.45}Na_{0.05}MnO_{2.50}$ features the presence of both layered $LiMnO_2$ (b) and Li_2MnO_3 (d), which are compared to their perfect models depicted in (c) and (d). Li/O deficient structure $Li_{1.20}Na_{0.05}MnO_{2.25}$ is outlined in (ii), where the portion reveals the presence of the ordered Li_2MnO_3 morphology previously observed (figure 6.10), magnified in (b) and also the $LiMnO_2$ magnified in (d), these were compared with their perfect models depicted in (c) and (e). This system has also shown the presence of grain boundaries as denoted by the dotted yellow line.
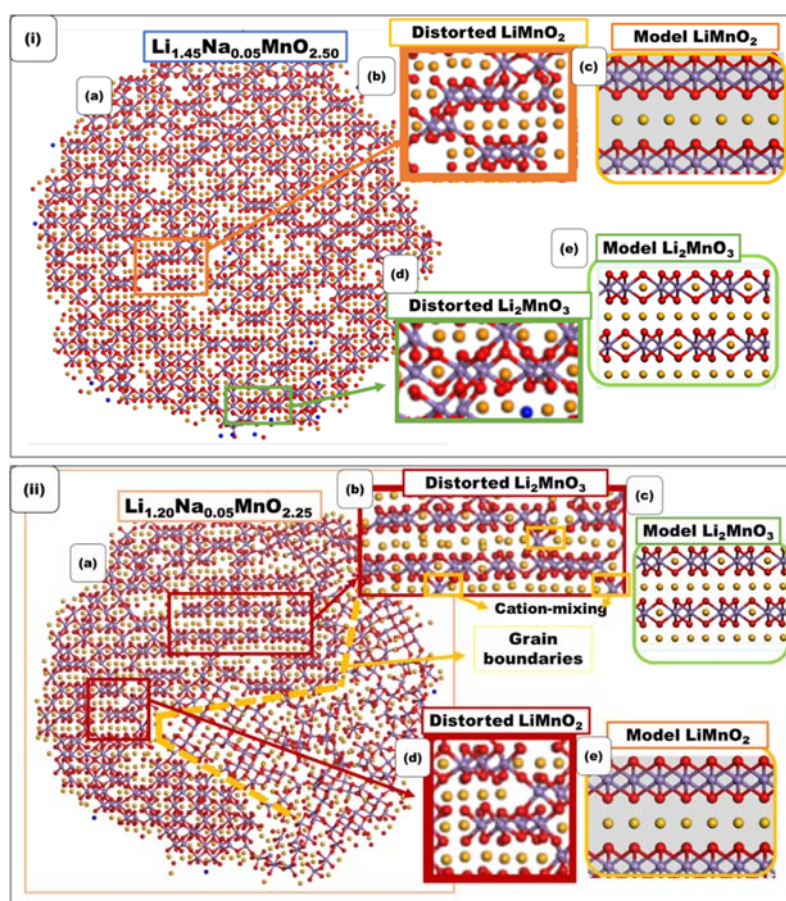
Figure 6.11: [i] (a) A slice cut-through $Li_{1.45}Na_{0.05}MnO_{2.50}$, (b) magnified portion from (a) showing the $LiMn_2O_4$ component, (c) $LiMn_2O_4$ perfect model, (d) distorted Li_2MnO_3 magnified from (a), (e) Li_2MnO_3 perfect model. [ii] (a) A slice cut-through $Li_{1.20}Na_{0.05}MnO_{2.25}$, (b) magnified portion from (a) depicting a distorted Li_2MnO_3 component, (c) Li_2MnO_3 perfect model, (d) magnified $LiMnO_2$ component compared with (e) perfect model $LiMnO_2$.

The atomistic arrangement for the last concentration i.e. $Li_{0.95}Na_{0.05}MnO_{2.00}$ is indicated in figure 6.12 and it can be noted from the slice cut-through (a), that the structure has recrystallised into a multi-grained crystal. The structure exhibits the mixing of layers, resulting from the migration of Mn to Li layers. A magnified portion of the slice cut-through is depicted in (b), showing the evolution of a distorted spinel-like structure that was comparable to the $LiMn_2O_4$ perfect model in (c).
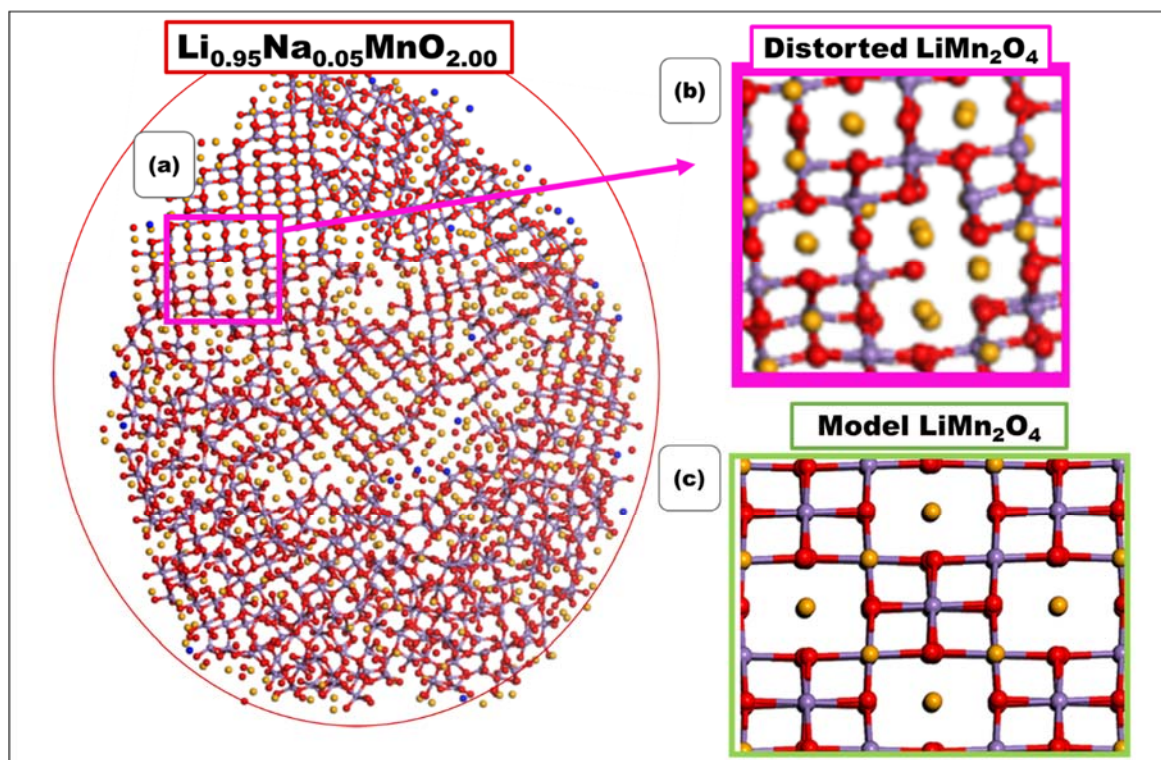
Figure 6.12: (a) A slice cut-through $Li_{0.95}Na_{0.05}MnO_{2.00}$, (b) distorted magnified portion of $LiMn_2O_4$, compared to (c) $LiMn_2O_4$, perfect model.

Figure 6.13 (i) represents the structural analysis for the $Li_{1.975}Na_{0.025}MnO_3$ system before the removal of Li/O. The slice cut-through is presented by (a), and (b) is the magnified portion from (a), indicating the presence of the Li_2MnO_3 phase accompanied by vacancies and also the cation mixing. Another magnified portion (c) also details the presence of the layered Li_2MnO_3 structure comparable to the Li_2MnO_3 perfect model. Upon Li/O removal, the $Li_{1.725}Na_{0.025}MnO_{2.75}$ structure develops grain boundaries (yellow dotted line) as shown in figure (ii), also, the magnified portion (b) depicts the Li_2MnO_3 layered phase, and another magnified potion (c) also depicts the presence of Li_2MnO_3. The last magnified segment (d) illustrates the formation of a distorted $LiMnO_2$ and (e) is the Li_2MnO_3 perfect model for comparison.
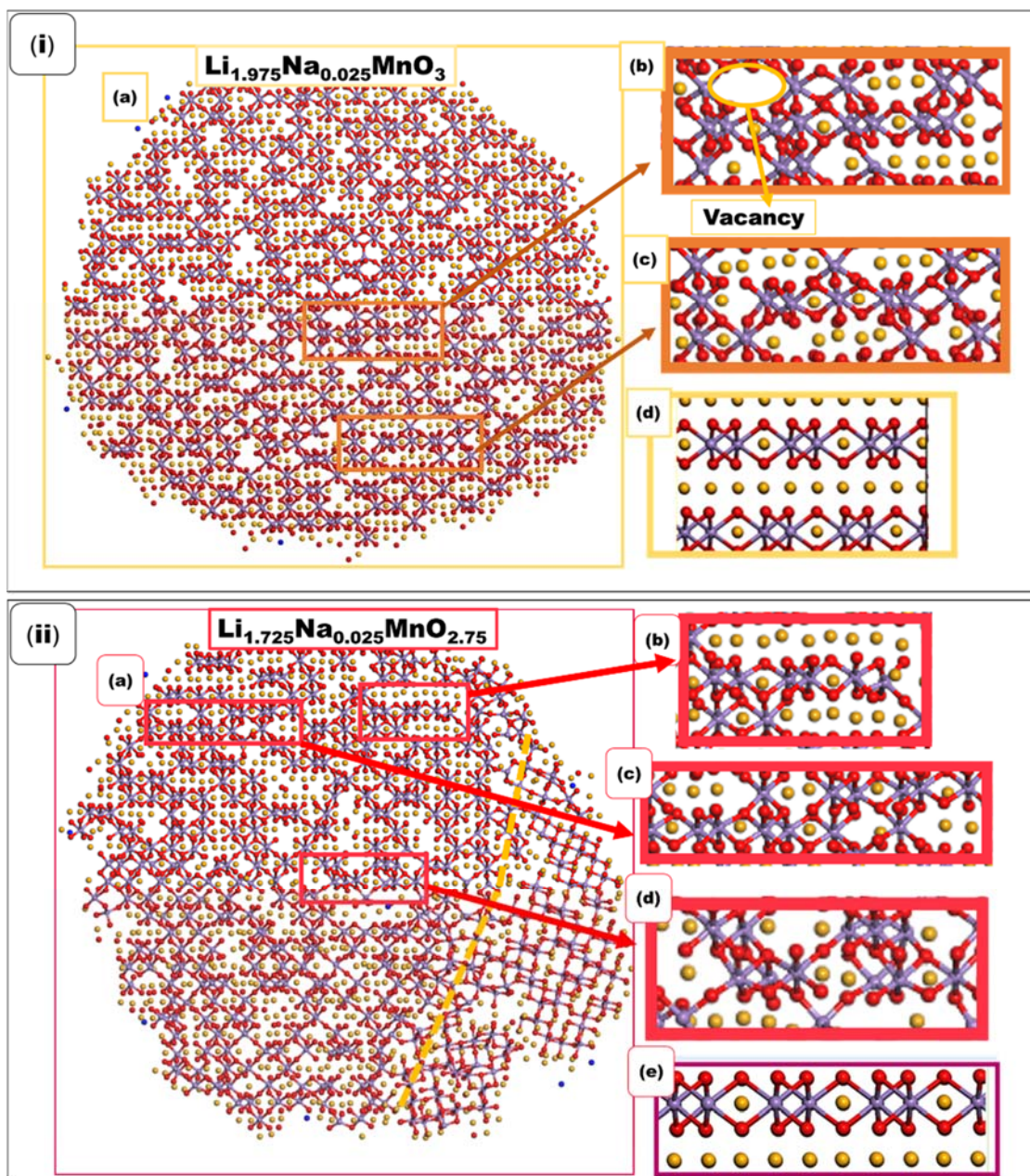
Figure 6.13: [i] (a) A slice cut-through $Li_{1.975}Na_{0.025}MnO_3$, **(b)** magnified portion from **(a)** displaying the Li_2MnO_3 component, **(c)** magnified portion from **(a)** also showing the Li_2MnO_3 component, **(c)** Li_2MnO_3 perfect model. **[ii] (a)** Cut-through $Li_{1.725}Na_{0.025}MnO_{2.75}$, **(b)**, **(c)** and **(d)** magnified portions from **(a)** showing Li_2MnO_3 and $LiMnO_2$ morphologies, **(e)** Li_2MnO_3 perfect model.

As charging progressed, the $Li_{1.475}Na_{0.025}MnO_{2.50}$ slice cut-through (a), depicted in figure 6.14, revealed the presence of the layered $LiMnO_2$ phase dominating most regions of the structure. The magnified segment (b) illustrates the $LiMnO_2$ component with the Li-layers highly occupied by Mn-ions and was compared with the $LiMnO_2$ perfect model in (c). The presence of the layered Li_2MnO_3 phases was confirmed

through the enlarged portions from the slice cut-through (d,e), which depicted cation mixing, these were also compared with the perfect model (f) Li_2MnO_3.
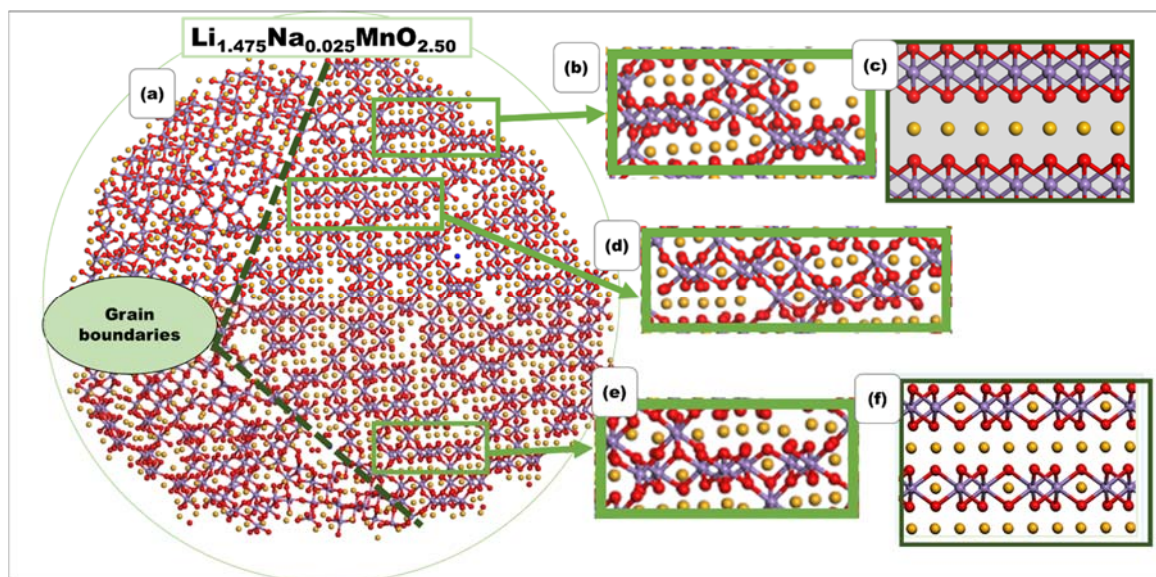
Figure 6.14: (a) A slice cut-through $Li_{1.475}Na_{0.025}MnO_{2.50}$, (b) magnified portion from (a) displaying the $LiMnO_2$ component, (c, d) magnified segments from (a) showing the Li_2MnO_3 components, (f) Li_2MnO_3 perfect model.

The last concentrations are depicted in figure 6.15, where (i) and (ii) indicate the $Li_{1.225}Na_{0.025}MnO_{2.25}$ and $Li_{0.975}Na_{0.025}MnO_{2.00}$, respectively. In (i), charging resulted in severe mixing of layers, making it difficult for accurate structural analysis. The magnified portions from the slice cut-through $Li_{1.225}Na_{0.025}MnO_{2.25}$ (a) are depicted in (b,c), where (b) illustrates the distorted $LiMnO_2$ and (c) the Li_2MnO_3 phase along with cation mixing.

For figure 6.15 (ii), a slice cut through $Li_{0.975}Na_{0.025}MnO_{2.00}$ is depicted by (a). This again is governed by defects with minimal regions constituting all Li layers. A magnified portion of the slice display highly distorted layers and the presence of the Li_2MnO_3 and $LiMnO_2$ phases co-existing. The perfect model depicted in $LiMnO_2$ (d) and (e) Li_2MnO_3 is for comparison.
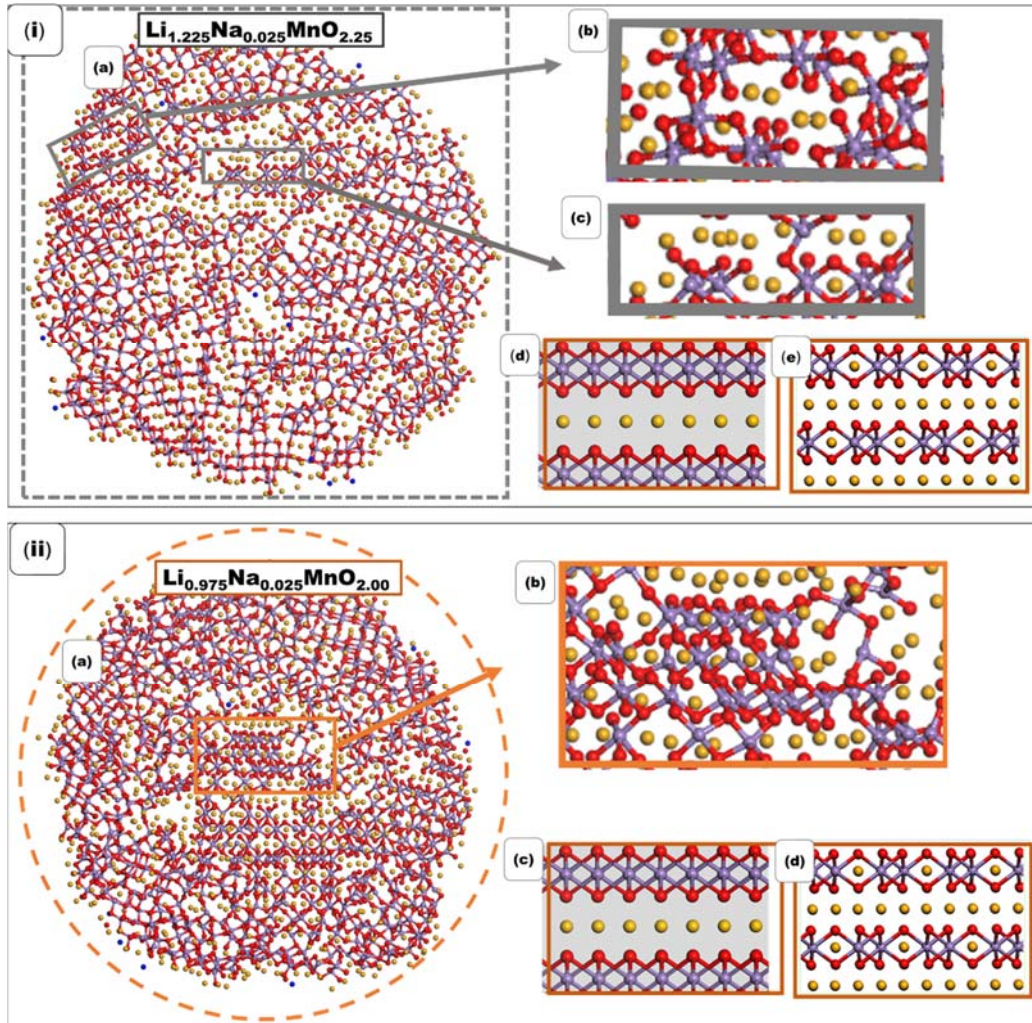
Figure 6.15: [i] (a) a slice cut through $Li_{1.225}Na_{0.025}MnO_{2.25}$, (b,) magnified portion from (a) displaying the LiMnO₂ component, (c,) magnified segments from (a) showing the Li_2MnO_3 components, (d) $LiMnO_2$ perfect model and (e) Li_2MnO_3 perfect model. [ii] (a) A slice ut-through $Li_{0.975}Na_{0.025}MnO_{2.00}$, (b,) magnified portion from (a) displaying the co-existence of Li_2MnO_3 and $LiMnO_2$, (c, d) $LiMnO_2$ and Li_2MnO_3 perfect models

6.3.5. Diffusion Coefficient

The diffusion coefficient plots for the $Li_{1.75}Na_{0.25}MnO_3$ (green) system with varying Li/O concentrations i.e. $Li_{1.50}Na_{0.25}MnO_{2.75}$ (black), $Li_{1.25}Na_{0.25}MnO_{2.50}$ (red), $Li_{1.00}Na_{0.25}MnO_{2.25}$ (blue) and $Li_{0.75}Na_{0.25}MnO_{2.00}$ (pink) are compared with that of pristine Li_2MnO_3 (brown) in figure 6.16 below. From the plots, the incorporation of Na^+ has increased Li^+ diffusion kinetics, with the $Li_{1.75}Na_{0.25}MnO_3$ (before Li/O extraction) reaching a maximum of 4.2×10^{-9} $nm^2.s^{-1}$ at 1000 K. Upon Li/O extraction, this value decreases to a value below 1.5×10^{-9} $nm^2.s^{-1}$ for all concentrations, except for $Li_{1.25}Na_{0.25}MnO_{2.5}$ which recorded its highest value of $3.9 \times 10^{-9}nm^2.s^{-1}$.
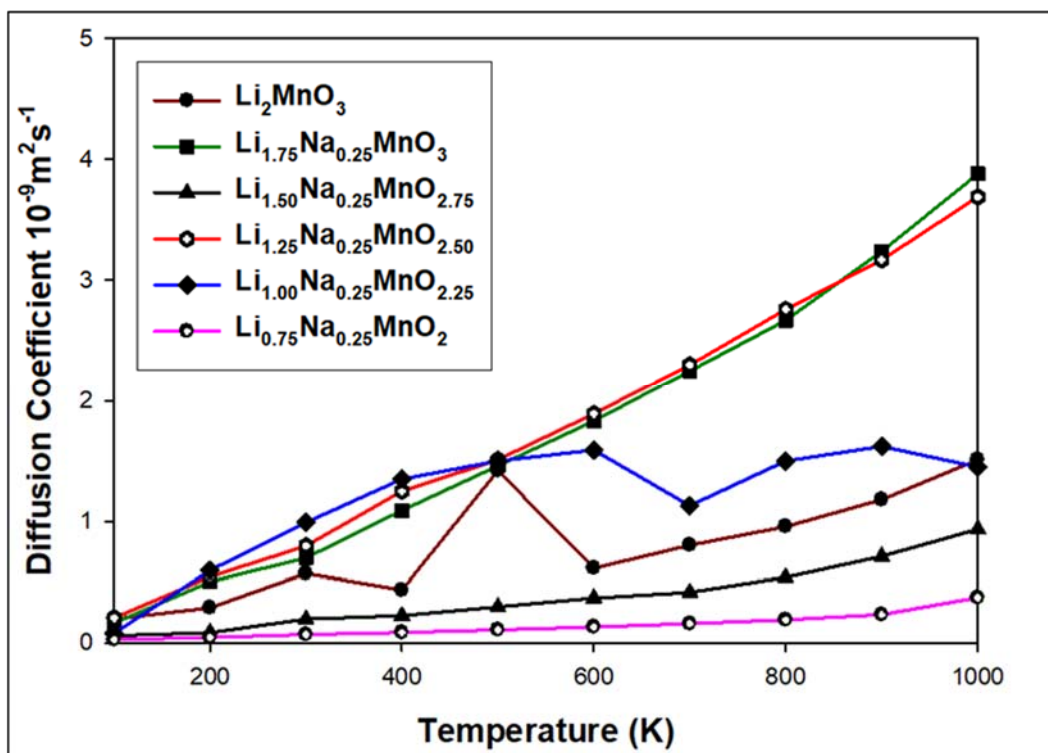
Figure 6.16: Diffusion coefficient plots for the Li₁.₇₅Na₀.₂₅MnO₃ (green) during Li/O removal Li₁.₅₀Na₀.₂₅MnO₂.₇₅ (black), Li₁.₂₅Na₀.₂₅MnO₂.₅₀ (red), Li₁.₀₀Na₀.₂₅MnO₂.₂₅ (blue) and Li₀.₇₅Na₀.₂₅MnO₂.₀₀ (pink) system, compared with Li₂MnO₃ (brown).

Figure 6.17 outlines the diffusion coefficient plots for $Li_{1.95}Na_{0.05}MnO_3$, calculated at various temperatures and Li/O concentrations. Li-ions in $Li_{1.45}Na_{0.05}MnO_{2.50}$ (pink), display high mobility as compared to the other systems. Accordingly, Li-ions become mobile from 0 $nm^2.s^{-1}$, increase up to 3.2 $nm^2.s^{-1}$ at 500 K, the graph abruptly increases to 6.4 $nm^2.s^{-1}$ at 600 K, decreases to 4.8 $nm^2.s^{-1}$ at 700 K, increases again to 7.2 $nm^2.s^{-1}$ at 800 K, drops to 6.3 $nm^2.s^{-1}$ at 900 K and reaches its maximum value of 9.2 $nm^2.s^{-1}$ at 1000 K. The fluctuation of the diffusion coefficient values may be attributed to phase change and also the presence of defects as the Li/O content was varied. The $Li_{1.95}Na_{0.05}MnO_3$ (red) is the system before Li/O removal and has shown the highest Li-ion value of 5.8 $nm^2.s^{-1}$ at 1000 K. For the $Li_{0.95}Na_{0.05}MnO_{2.00}$ (green), $Li_{1.70}Na_{0.05}MnO_{2.70}$ (blue), $Li_{1.45}Na_{0.05}MnO_{2.50}$ and $Li_{1.45}Na_{0.05}MnO_{2.50}$ Li-ion mobility was below 4 $nm^2.s^{-1}$.
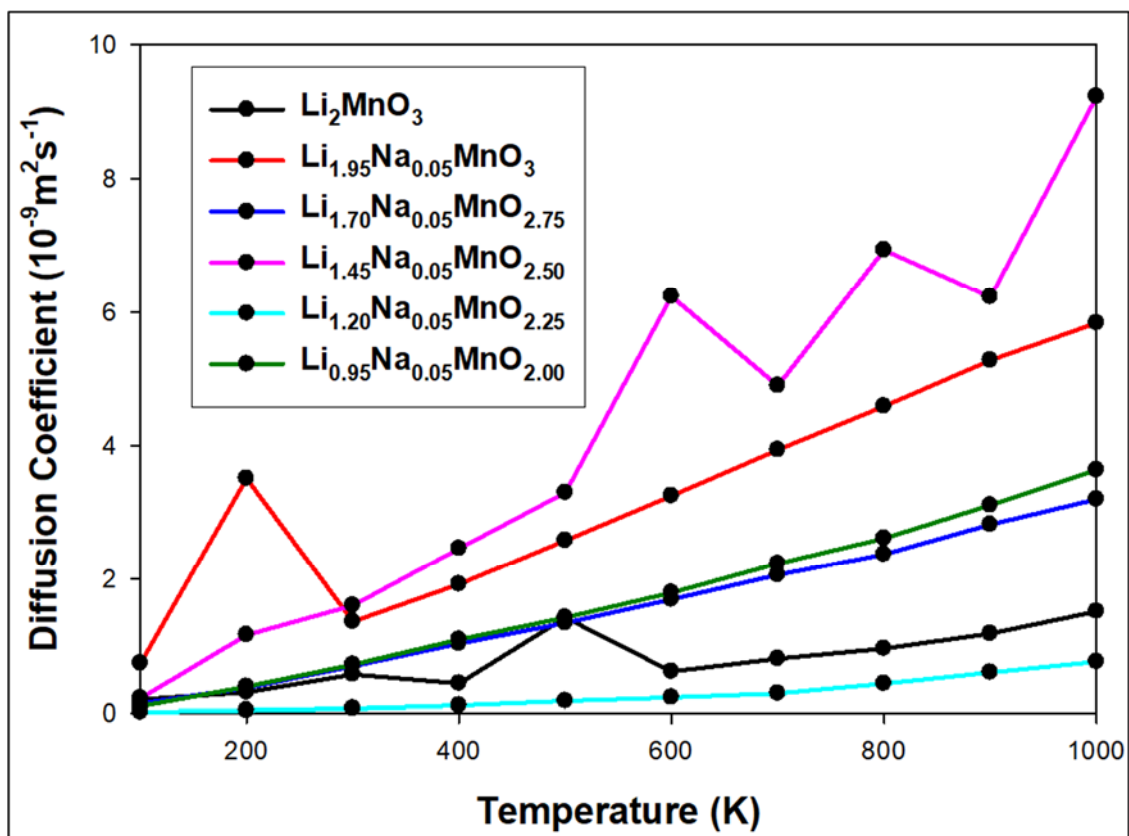
Figure 6.17: Diffusion coefficient graphs for the charging of Li₁.₉₅Na₀.₀₅MnO₃ (red) with charged Li₁.₇₀Na₀.₀₅MnO₂.₇₅ (blue), Li₁.₄₅Na₀.₀₅MnO₂.₅ (pink), Li₁.₂₀Na₀.₀₅MnO₂.₂₅ (teal) and Li₀.₉₅Na₀.₀₅MnO₂.₀₀ (green) compared with the Li₂MnO₃ (black) configuration.

Li-ion kinetics for the $Li_{1.975}Na_{0.025}MnO_3$ system during the simulated charging process is illustrated in figure 6.18. From the diffusion coefficient plots, Li-ions in $Li_{0.975}Na_{0.025}MnO_{2.00}$ diffuse better than the rest of the systems. This is the same system that depicted broader XRD, and RDF peaks as a result of highly distorted layers. Accordingly, Li-ions start diffusing from 0 $nm^2.s^{-1}$ and exponentially increase until 1000 K with a diffusion coefficient of 3.7 $nm^2.s^{-1}$. This was followed by the $Li_{1.725}Na_{0.025}MnO_2$. Li-ion mobility was also observed to have exponentially increased from 0 $nm^2.s^{-1}$ up to 3.3 $nm^2.s^{-1}$ at 1000 K. For the $Li_{1.475}Na_{0.025}MnO_{2.25}$ and $Li_{1.225}Na_{0.025}MnO_{2.50}$ systems, the diffusion coefficient decreased and was found to be lower than 1.3 $nm^2.s^{-1}$, in comparison with the pristine Li_2MnO_3. The two systems exhibit poor Li-ion kinetics.
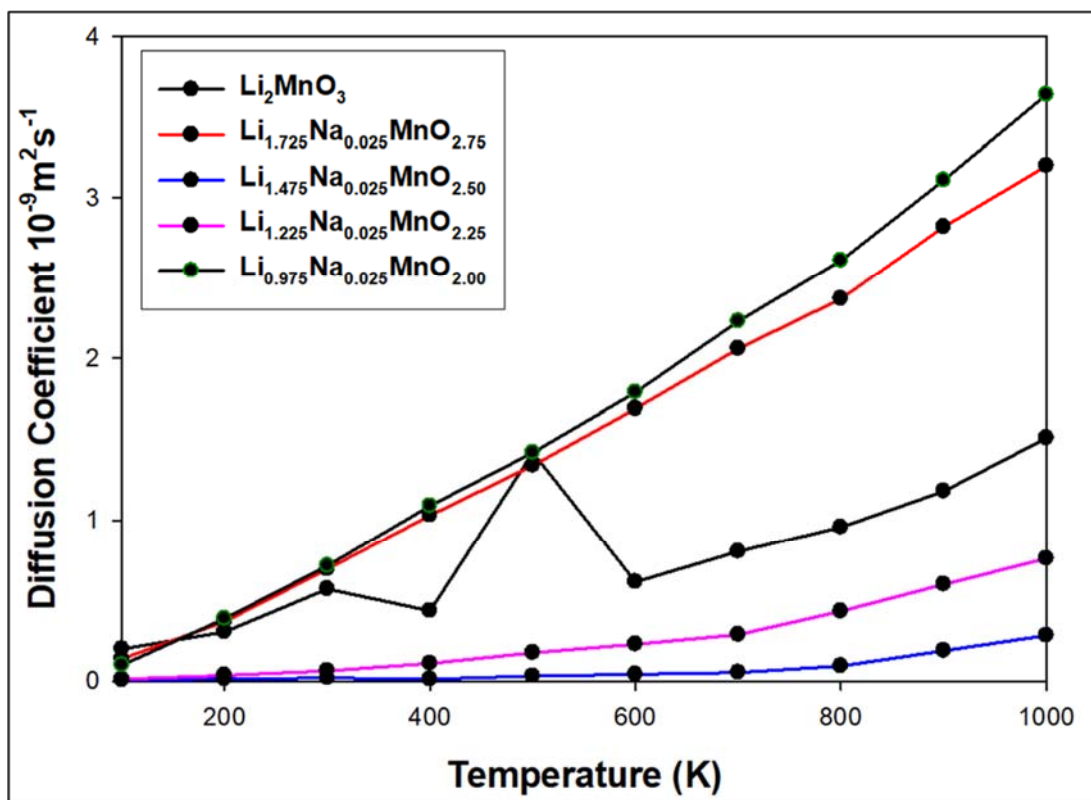
Figure 6.18: Diffusion coefficient graphs for the charging of $Li_{1.975}Na_{0.025}MnO_3$ showing charged $Li_{1.725}Na_{0.025}MnO_{2.75}$ (red), $Li_{1.475}Na_{0.025}MnO_{2.50}$ (blue), $Li_{1.225}Na_{0.025}MnO_{2.25}$ (pink) and $Li_{0.995}Na_{0.025}MnO_{2.00}$ (green) compared with pristine Li_2MnO_3 (black) system.

6.4. Summary

Investigation of the $Li_{1.75}Na_{0.25}MnO_3$, $Li_{1.95}Na_{0.05}MnO_3$, and $Li_{1.975}Na_{0.025}MnO_3$ systems during the charging process involving the leaching of O^- and Li^+ was carried out via the A+R technique in a quest to explore their structural and electrochemical properties. For the $Li_{1.75}Na_{0.25}MnO_3$ system constituting high Na content (12,5 %), the RDF analysis revealed peak broadening even after recrystallisation was carried out, suggesting that Li/O removal induced highly distorted and deformed crystal layers. This was also confirmed by the presence of considerable grain boundaries on the molecular graphics with structures resembling that of amorphous configurations. Again, the XRD displayed broader diffraction peaks, with some characteristic peaks being lost as the leaching of Li/O progressed, this confirms the severity of defects. Microstructural analysis during the charging process also revealed a considerable amount of defects, particularly, the migration of Mn^+ into Li^+ layers leading to the formation of spinel-like configurations. The Li-ion mobility for the $Li_{1.75}Na_{0.25}MnO_3$ and throughout the charging process was significantly low when compared to the pristine

structure. The results suggest that doping a large amount of Na^+ into the Li_2MnO_3 structure deteriorates the structural and electrochemical properties during the charging process [49].

The crystallisation of the $Li_{1.975}Na_{0.025}MnO_3$ system, constituting 1.25% Na^+ content was confirmed by the presence of multiple sharp peaks of increased intensity on the RDF plots, with the atomistic models showing a reduced number of grain boundaries when compared to the $Li_{1.75}Na_{0.05}MnO_3$ (12,5 % Na) system. The leaching of Li/O for this system also resulted in broader XRDs, with the evolution of the spinel $LiMn_2O_4$, layered Li_2MnO_3, and $LiMnO_2$ morphologies. However, the peaks associated with the spinel phase ($2\Theta \sim 48^\circ$ and 68°) decrease significantly for the $Li_{1.225}Na_{0.025}MnO_{2.25}$ and $Li_{0.975}Na_{0.025}MnO_{2.00}$ configurations. The microstructures confirmed regions dominated by the $LiMnO_2$ and also the mixing of layers intensified as the Li/O content varied. Diffusion coefficient plots displayed an increase in Li^+ mobility for the $Li_{1.975}Na_{0.025}MnO_3$ system before Li/O removal, and also the last configuration $Li_{0.975}Na_{0.025}MnO_{2.00}$ which showed a high concentration of defects. Again, it was noted that the fluctuation of the diffusion coefficient plots was minimal for the charging of the $Li_{1.975}Na_{0.025}MnO_3$ system, this may be due to the small number of sodium incorporated in the system.

In comparison with the $Li_{1.75}Na_{0.25}MnO_3$ (12.5% Na) and $Li_{1.975}Na_{0.025}MnO_3$ (1.25% Na), the charging of $Li_{1.95}Na_{0.05}MnO_3$ (2.5% Na) resulted in improved structural arrangement and Li-ion diffusion kinetics. Recrystallisation was again confirmed through increased sharp Mn-O pair distribution peaks with only the $Li_{0.95}Na_{0.05}MnO_{2.00}$ concentration exhibiting broader peaks due to increased defects. From the molecular graphics, grain boundaries evolved at a later stage of charge ($Li_{1.20}Na_{0.05}MnO_{2.25}$). The XRD analysis again confirmed the presence of Li_2MnO_3 and the evolution of the spinel $LiMn_2O_4$, layered and $LiMnO_2$ morphologies, with the $Li_{1.45}Na_{0.05}MnO_{2.50}$ system showing decreased peak intensity at lower angles, suggesting a perturbed ordering of the Li/Mn in the transition layers. Internal microstructures revealed well-ordered Li_2MnO_3 regions which were maintained throughout the charging process except for the $Li_{1.45}Na_{0.05}MnO_{2.50}$ and $Li_{0.95}Na_{0.05}MnO_{2.00}$ systems. These are the two charged systems that displayed improved Li-ion diffusion kinetics with fluctuating graphs. The fluctuation of the diffusion coefficient plots was observed for systems dominated by the $LiMnO_2$ morphology. From the results, it is apparent that the charging of

$Li_{1.95}Na_{0.05}MnO_3$ leads to orderly arranged Li_2MnO_3 structures with significantly increase Li-ion kinetics [18] as evidenced by the increase in diffusion coefficient values as the charging progressed.

7.1. Conclusion

The exploration of new electrode materials exhibiting improved electrochemical performance and low cost for high-density LIBs applicable in electric vehicles is one of today's most challenging issues in material research. This study unveils the simulated synthesis of ternary Li_2MnO_3 and quaternary $Li_{2-x}Na_xMnO_3$ composites i.e., nanospheres, nanoporous and bulk electrode materials through the high-temperature synthesis and crystallisation process. This strategy is responsible for the spontaneous growth of crystals from an amorphous precursor exhibiting microstructural features observed experimentally, such as grain boundaries, point defects and dislocations. Accordingly, nanostructured Li_2MnO_3 (spherical, porous) and the bulk material with a large number of atoms (32148) were modelled to investigate their electrochemical and structural properties. Our Li_2MnO_3 models revealed their melting point at approximately 1845 K, this is in accord with previous studies [17]. Subsequently, the radial distribution functions around this temperature depict broader peaks as an indicative measure of phase transition from crystalline to amorphous state. A perfectly ordered Li_2MnO_3 structure constitutes alternating layers of lithium, and lithium/manganese slotted between oxygen layers. However, upon crystallisation, our models reveal cation mixing accompanied by vacancies leading to incoherent structures. These disoriented structures are analogous to the NaCl-type structures fabricated by Kataoka, et al. [37] which displayed improved performance when compared to the ordered Li_2MnO_3 structures. We also note that the uncharged systems (Li_2MnO_3) crystallised into single-grain crystals with no emergence of grain boundaries as evidenced by their internal microstructures. We, therefore, scrutinised the diffusion coefficients of the generated morphologies at various temperatures and the nanosphere depicted the highest lithium-ion diffusion in comparison to the other morphologies (porous and bulk).

To mirror the discharge process, $Li_{2-x}MnO_{3-X}$ (x = 0.25, 0.50, 0.75 and 1.0) configurations for the nanostructures (porous, spherical) were carried out by removing systematically both lithium and oxygen ions simultaneously from the Li_2MnO_3 with

oxygen charge compensated. Contrary to the uncharged systems (Li_2MnO_3), the charged systems crystallised into multi-grained crystals with grain boundaries increasing with a decrease in Li/O content. Interrogative analysis of the internal microstructures revealed crystallographic details such as cationic (Li-Mn) site mixing, vacancies and migration of Mn into the Li layers leading to the formation of distorted layered (Li_2MnO_3, $LiMnO_2$) and spinel (Mn_3O_4, $LiMn_2O_4$) polymorphs. Similarly, the formation of diffraction patterns associated with these polymorphs was deduced from the XRD patterns which showed extensive peak broadening along with splitting and displacement of certain peaks. The coexistence of these polymorphs plays a significant role in Li-Mn-O cathodes, for example, $LiMnO_2$ can increase the capacity and possess better electronic conductivity than the pristine Li_2MnO_3 phase resulting in less electrode polarization [25]. It is worth noting that the nanoporous with lattice size 73 Å behaves differently from all the structures. Particularly, the $Li_{1.25}MnO_{2.25}$ concentration depicts minimal grains and narrowing of the XRD pattern resulting in the formation of morphologies with reduced defects.

Efforts toward alleviating structural instability during the cycling of the Li_2MnO_3 nanosphere which exhibited improved Li-ion kinetics were successfully achieved by doping a small amount of Na^+ into the Li^+ sites thus generating models of the form $Li_{2-x}Na_xMnO_3$ (x = 0.25, 0.50, 0.75 and 1.0). Models involving large Na content displayed poor structural stability with some structures failing to amorphise due to lattice deformation. The lattice deformation hinders the smooth movement of Li ions during the charging process which significantly decreases the electrochemical performance of the host material [19], as observed from the modelled $Li_{1.75}Na_{0.25}MnO_3$ system constituting 12% sodium. For this system ($Li_{1.75}Na_{0.25}MnO_3$), charging induced the distortion and deformation of the lattice, resulting in the formation of amorphous structures in some regions [89]. The $Li_{1.95}Na_{0.05}MnO_3$ system displayed considerably improved structural stability in comparison with the rest of the sodium-doped systems. This system is closer to the $Li_{1.90}Na_{0.10}MnO_3$ prepared by Dong et al. which showed enhanced cycling stability compared to the undoped Li_2MnO_3 structure and delivered excellent discharge capacity retention of 99.3% after 45 cycles [83]. The internal microstructures for the $Li_{1.95}Na_{0.05}MnO_3$ system depicted large regions dominated by the well-ordered Li_2MnO_3 and minimal structural defects which promotes the electrochemical activation of the host material [5]. Structural stability was maintained

throughout the charging process and the spinel phase emerges at a later stage of charge. Similar results were noticed for the sodium-incorporated $Li_{1.15}Na_{0.05}[Ni_{0.13}Co_{0.13}Mn_{0.54}]O_2$ with improved electrochemical performance. The structural stability enhancement may be attributed to the correct amount of sodium incorporated into the lithium lattice, which serves as a barrier for the formation of three adjacent lithium vacancies and the migration of manganese ions responsible for structural transformation to the undesired spinel structures [83]. Moreover, the shifting of the diffraction peak at approximately $2\Theta \sim 38^{\circ}$ to lower angles confirms the enlargement of Li layers upon sodium entrance, which is responsible for inhibiting the layered to spinel transformation.

Lithium-ions in the Li_2MnO_3 nanosphere during the charging process exhibited high kinetics compared to both the nanoporous (75,73 Å) and sodium-doped $Li_{2-x}Na_xMnO_3$ systems. The nanoporous diffusion coefficient values were below $0.4 \times nm^2.s^{-1}$ except for nanoporous 75 Å, which showed improved lithium mobility of $6.1 \times nm^2.s^{-1}$ for the $Li_{1.00}MnO_{2.00}$ system. Sodium-doped $Li_{2-x}Na_xMnO_3$ nanospheres depicted better lithium mobility than the nanoporous systems. For the $Li_{1.75}Na_{0.25}MnO_3$ configuration, the charged $Li_{1.25}Na_{0.25}MnO_{2.5}$ yielded the highest diffusion coefficient at $3.9 \times nm^2.s^{-1}$. The $Li_{1.95}Na_{0.05}MnO_3$ on the other hand revealed a diffusion coefficient value of 9.2 $nm^2.s^{-1}$ for the charged $Li_{1.45}Na_{0.05}MnO_{2.50}$, however, the graph fluctuates. For the $Li_{1.975}Na_{0.025}MnO_3$ configuration, the highest diffusion ($3.7 nm^2.s^{-1}$) was reached for the $Li_{0.975}Na_{0.025}MnO_{2.00}$ with no fluctuation. From the results, lithium ions are highly mobile in charged configurations (systems with low lithium and oxygen content), accompanied by the fluctuation of the diffusion coefficient graphs, emanating from the transformation to spinel-like structures.

This study sheds light pertaining to the influence of oxygen loss and sodium ion doping on the Li_2MnO_3 host material in terms of ionic diffusion and structural transitions that occur within the intermediate phases during the cycling process and their impact on the cycling capabilities.

7.2. Recommendations

To better understand the heterogeneity in our results, high-temperature studies will be carried out on the charged $Li_{2-x}MnO_{3-x}$ systems. The mechanical properties and

volume change properties of the nanostructures will be analysed as this contributes toward the performance properties of this material. Another aspect of interest will be the exploration of sodium-doped systems of different morphologies i.e. nanoporous, nanosheets and nanorods since they play a significant role in the performance of the lithium-ion battery's host materials.

References

[1] A Manthiram, "A Reflection on Lithium-Ion Battery Cathode Chemistry," Nature Communications,11,1550, 2020.

[2] J. Duan, X. Tang, H. Dai, Y. Yang, W. Wu, X. Wei, and Y. Huang, "Building Safe Lithium Ion Batteries for Electric Vehicles: A Review," Electrochemical Energy Reviews, 3, 1-42, 2020.

[3] B. Scrosati and J. Garche, "Lithium Batteries: Status, Prospects and Future," Journal of Power Sources, 95, 2419-2430, 2010.

[4] Y. Chen, Y. Kang, Y. Zhao, L. Wang, J. Liu, Y. Li, Z. Liang, X. He, X. Li, N. Tavajohi, and B. Li, "A Review of Lithium-Ion Battery Safety Concerns: The Issues, Strategies and Testing Standards," Journal of Energy Chemistry, 59, 3-99, 2021.

[5] J. Yang, F. Cheng, X. Zhang, H. Gao, Z. Tao and J. Chen, "Improving Electrochemical Properties by Sodium Doping for Lithium-Rich Layered Oxides," ACS Applied Energy Materials, 3, 8953-8959, 2020.

[6] J-Y. Piao, L. Gu, Z. Wei, J Ma, J. Wu, W. Yang, Y. Gong, Y-G. Sun, S-Y. Duan, X-S. Tao, D-S. Bin, A-M. Cao and L-j. Wan, "Phase Control on Surface for Stabilization of High Energy Cathode Materials of Lithium Ion Batteries," Journal of the American Chemical Society, 141, 4900-4907, 2019.

[7] W. Zhao, S. Yamamoto, A. Tanaka and H. Noguchi, "Synthesis of Li-Excess Layered Cathode Material with Enhanced Reversible Capacity for Lithium Ion Batteries through the Optimization of Precursor Synthesis Method," Electrochimica Acta, 143, 347-356, 2014.

[8] I. Takahashi, T. Maeda, H. Kiuchi, K. Nakanishi, A. Ohma, M. Hatano, T. Fukunaga, T. Ohta and E. Matsubara, "Mechanism of Structural Change and the Trigger of Electrochemical Degradation of Li-Rich Layered Oxide Cathodes during Charge–Discharge Cycles," ACS Applied Energy Materials, 2, 8118-8124, 2019.

[9] M.D Radin, J. Vinckeviciute, R. Seshadri and A. Van der Ven, "Manganese Oxidation as the Origin of the Anomalous Capacity of Mn-Containing Li-excess Cathode Materials," Nature Energy, 4, 639-646, 2019.

[10] Y. Song, X. Zhao, C. Wang, H. Bi, J. Zhang, S. Li, M. Wang and R. Che, "Insight Into the Atomic Structure of Li_2MnO_3 in Li-rich Mn-based Cathode Materials and the Impact of its Atomic Arrangement on Electrochemical Performance," Journal of Materials Chemistry, 5, 11214-11223, 2017.

[11] E. Cho, K. Kim, C. Jung, S-W Seo, K. Min, H. S. Lee, G-S. Park and J. Shin, "Overview of the Oxygen Behavior in the Degradation of Li_2MnO_3 Cathode Material," Journal of Physical Chemistry C, 121, 21118-21127, 2017.

[12] A. Marusczyk, J. Albina, T. Hammerschmidt, R. Drautz, T. Eckl and G. Henkelman, "Oxygen Activity and Peroxide Formation as Charge Compensation Mechanisms in Li_2MnO_3," Journal of Materials Chemistry A, 5, 15183-15190, 2017.

[13] A. S. Menon, D. O. Ojwang, T. Willhammar, V. K. Peterson, K. Edstrom, C. P. Gomeza and W. R. Brant, "The Influence of Synthesis Routes on the Crystallography, Morphology and Electrochemistry of Li_2MnO_3," ACS Applied Materials and Interfaces, 5, 1-15, 2020.

[14] S. F. Amalraj, D. Sharon, M. Talianker, C. M. Julien, L. Burlaka, R. Lavia, E. Zhechevad, B. Markovsky, E. Zinigrad, D. Kovacheva, R. Stoyanova and D. Aurbach, "Study of the Nanosized Li_2MnO_3: Electrochemical Behavior, Structure, Magnetic Properties and Vibrational Modes," Electrochimica Acta, 97, 259-270, 2013.

[15] Y. Ding· Z. P. Cano, A. Yu · J Lu and Z. Chen, "Automotive Li-Ion Batteries: Current Status and Future Perspectives," Electrochemical Energy Reviews, 2, 1-28, 2019.

[16] R. Chen, T. Zhao, X. Zhang, L. Li and F. Wu, "Advanced Cathode Materials for Lithium-Ion Batteries Using Nanoarchitectonics," Nanoscale Horizons, 423-444, 2016.

[17] T. X. T. Sayle, F. Caddeo, N. O Monama, K. M. Kgatwane, P. E. Ngoepe and D.C. Sayle, "Origin of Electrochemical Activity in Nano-Li_2MnO_3; Stabilization via a 'Point Defect Scaffold'," Nanoscale, 7, 1167-1180, 2015.

[18] A. M. Hashem, A. E. Abdel-Ghany, R. S. El-Tawil, A. Mauger and C. M. Julien, "Effect of Na Doping on the Electrochemical Performance of $Li_{1.2}Ni_{0.13}Co_{0.13}Mn_{0.54}O_2$ Cathode for Lithium-Ion Batteries," Sustainable Chemistry, 3, 131-148, 2022.

[19] J. J. Abraham, C. R. A. Arro, H. A. Tariq, R. Kahraman, S. Al-Qaradawi, T. M. Al tahtamouni and R.A. Shakoor, "Sodium and lithium incorporated cathode materials for energy storage applications - A focused review," Journal of Power Sources, 506, 230098, 2021.

[20] P. G. Bruce, B. Scrosati and J. M. Tarascon, "Nanomaterials for Rechargeable Lithium Batteries," Angewandte Chemie International Edition, 47, 2930-2946, 2008.

[21]   F. Massel, K. Hikima, H. Rensmo, K. Suzuki, M. Hirayama, C. Xu, R. Younesi, Y-S. Liu, J. Guo, R. Kanno, M. Hahlin and L-C. Duda, "Excess Lithium in Transition Metal Layers of Epitaxially Grown Thin Film Cathodes of Li_2MnO_3 Leads to Rapid Loss of Covalency during First Battery Cycle," The Journal of Physical Chemistry C,123, 28519-28526, 2019.

[22] F. Zheng, C. Yang, X. Xiong, J. Xiong, R. Hu, Y. Chen and M. Liu, "Nanoscale Surface Modification of Lithium-Rich Layered-Oxide Composite Cathodes for Suppressing Voltage Fade," Angewandte Chemie International Edition, 54, 13058-13062, 2015.

[23] M. M. Thackeray, C. S. Johnson, J. T Vaughey, N. Li and S. A. Hackney, "Advances in Manganese-oxide Composite Electrodes for Lithium-Ion Batteries," Journal of Materials Chemistry, 5, 2257-2267, 2005.

[24] T. Matsunaga, H. Komatsu, K. Shimoda, T. Minato, M. Yonemura, T. Kamiyama, S. Kobayashi, T. Kato, T. Hirayama, Y. Ikuhara, H. Arai, Y. Ukyo, Y. Uchimoto and Z. Ogumi, "Dependence of Structural Defects in Li_2MnO_3 on Synthesis Temperature," Chemistry of Materials, 28, 4143-4150, 2016.

[25] Y. Sun, H. Cong, L. Zan and Y. Zhang, "Oxygen Vacancies and Stacking Faults Introduced by Low-Temperature Reduction Improve the Electrochemical Properties of Li_2MnO_3 Nanobelts as Lithium-Ion Battery Cathodes," ACS Applied Materials and Interfaces, 9, 38545-38555, 2017.

[26] G. Yang, L. Wang, J. Wang and W. Yan, "Fabrication and Formation Mechanism of Li_2MnO_3 Ultrathin Porous Nanobelts by Electrospinning," Ceramics International, 43, 71-76, 2017.

[27] B. Ammundsen and J. Paulsen, "Novel Lithium-Ion Cathode Materials Based on Layered Manganese Oxides," Advanced Materials, 13, 943-956, 2001.

[28] M. H. Rossouw and M. M. Thackeray, "Lithium Manganese Oxides from Li_2MnO_3," Materials Research Bulletin, 26, 463-473, 1991.

[29] A. D. Robertson and P. G. Bruce, "Mechanism of Electrochemical Activity in Li_2MnO_3," Chemistry of Materials, 15, 1984-1992, 2003.

[30] M. M Thackeray, "Manganese Oxides for Lithium Batteries," Progress in Solid State Chemistry, 25, 1-71, 1997.

[31] G. R. Jain, J. S. Yang, M. Balasubramanian and J. J. Xu, "Synthesis, Electrochemistry, and Structural Studies of Lithium Intercalation of a Nanocrystalline Li_2MnO_3-like Compound," Chemistry of Materials, 17, 3850-3860, 2005.

[32] J. Lim, J. Moon, J. Gim, S. Kim, K. Kim, J. Song, J. Kang, W. B. Im and J. Kim, "Fully Activated Li_2MnO_3 Nanoparticles by Oxidation Reaction," Journal of Materials Chemistry, 22, 11772-11777, 2012.

[33] G. Liu and S. Zhang, "One-step Synthesis of Low-cost and High Active Li_2MnO_3 Cathode Materials," International Journal of Electrochemical Science, 11, 5545-5551, 2016.

[34] Y. Xiang and X. Wu, "Enhanced Electrochemical Performances of Li_2MnO_3 Cathode Materials by Al Doping," Ionics, 24, 83-89, 2018.

[35] N. Kuganathan, E. N. Sgourou, Y. Panayiotatos and A. Chroneuos, "Defect Process, Dopant Behaviour and Li-Ion Mobility in the Li_2MnO_3 Cathode Material," Energies, 12, 1329-1339, 2019.

[36] C. Jacob, J. Jian, Y. Zhu, Q. Sub and H. Wang, "A New Approach to Investigate Li_2MnO_3 and $Li(Ni_{0.5}Mn_{0.3}Co_{0.2})O_2$ Mixed Phase Cathode Materials," Journal of Materials Chemistry. A, 2, 2283-2289, 2014.

[37] R. Kataoka, N. Taguchi, T. Kojima, N. Takeichi and T. Kiyobayashi, "Improving the Oxygen Redox Stability of NaCl-Type Cation Disordered Li_2MnO_3 in a Composite Structure of Li_2MnO_3 and Spinel-Type $LiMn_2O_4$," Journal of Materials Chemistry, 7, 5381-5390, 2019.

[38] M. M. Thackeray, M. F. Mansuetto, D. W. Dees and D. R. Vissers, "The Thermal Stability of Lithium-Manganese-Oxide Spinel Phases," Materials. Research. Bulletin, 31, 133-140, 1996.

[39] A. Boulinea, L. Croguennec, C. Delmas and F. Weill, "Structure of Li_2MnO_3 with Different Degrees of Defects," Solid State Ionics, 180, 1652-1659, 2010.

[40] F. Fu, Y-P. Deng, C-H. Shen, G-L. Xu, X-X. Peng, Q. Wanga, Y-F. Xu, J-C. Fang, L. Huang and S. G. Sun, "A Hierarchical Micro/Nanostructured $0.5Li_2MnO_3 \cdot 0.5LiMn_{0.4}Ni_{0.3}Co_{0.3}O_2$ Material Synthesized by Solvothermal Route as High Rate Cathode of Lithium Ion Battery," Electrochemistry Communications, 44, 54-58, 2014.

[41] Y. Nakao, K. Ozawa, Y. Nemoto, F. Uesugi, H. Fujil and T. Mchiku, "Structural Variation of Li_2MnO_3 During Charge-Discharge Cycling," Journal of the Ceramic Society of Japan, 123, 589-594, 2015.

[42] H. Huang, C. A. Vincent and P. G. Bruce, "Correlating Capacity Loss of Stoichiometric and Nonstoichiometric Lithium Manganese Oxide Spinels electrodes with their structural integrity," Journal of the Electrochemical Society, 146, 3649-3654, 1999.

[43] T. X. T. Sayle, C. R. A. Catlow, R. R. Maphanga, P. E. Ngoepe and D. C. Sayle, "Generating MnO_2 Nanoparticles Using Simulated Amorphization and Recrystallization," Journal of the American Chemical Society, 127, 12828-12837, 2005.

[44] W. Sun, F. Cao, Y. Liu, X. Zhao, X Liu and J. Yuan J, "Nanoporous $LiMn_2O_4$ Nanosheets with Exposed {111} Facets as Cathodes For Highly Reversible Lithium-ion Batteries," Journal of Materials Chemistry, 22, 20952-20957, 2012.

[45] R. R. Maphanga, T. X. T. Sayle, P. E. Ngoepe and D. C. Sayle, "Amorphization and Recrystallization Study of Lithium Insertion into Manganese Dioxide," Physical Chemistry Chemical Physics, 13, 1307-1313, 2011.

[46] D. C Sayle, and T. X. T. Sayle, "Formation and Elimination of Anti-site Defects During Crystallization in Perovskite $Ba_{1-x}Sr_xLiF_3$," Journal of Computational and Theoretical Nanoscience, 4, 299-308, 2007.

[47] M. G. Matshaba, D. C. Sayle, T. X. Sayle and P. E.Ngoepe, "Structure of Surface Entrance Sites for Li Intercalation into TiO_2 Nanoparticles, Nanosheets, and Mesoporous Architectures with Application for Li-Ion Batteries," Journal of Physical Chemistry C, 120, 14001-14008, 2016.

[48] R. S. Ledwaba, D. C. Sayle and P. E. Ngoepe, "Atomistic Simulation and Characterization of Spinel $Li_{1+x}Mn_2O_4$ ($0 \leq x \leq 1$) Nanoparticles," ACS Appl. Energy Mater., 3, 1429-1438, 2020.

[49] Q. Ma, Z. Chen, S. Zhong, J. Meng, F. Lai, Z. Li, Chen. Cheng, L. Zhang and T. Liu, "Na-substitution Induced Oxygen Vacancy Achieving High Transition Metal Capacity in Commercial Li-Rich Cathode," Nano Energy, 81,105622, 2021.

[50] D-H. Seo, J. Lee, A. Urban, R. Malik, S. Y. Kang and G. Ceder, "The Structural and Chemical Origin of the Oxygen Redox Activity in Layered and Cation-Disordered Li-Excess Cathode Materials," Nature Chemistry, 8, 692-697, 2016.

[51] A. Leonardi, "Molecular Dynamics and X-Ray Powder Diffraction Simulations," University of Trento. PhD Thesis, Trento (Italy), 2012.

[52] P. E. Ngoepe. R. R. Maphanga and D. C. Sayle, "Toward the Nanoscale," in Computational Approaches to Energy Materials, John Wiley and Sons, 2013, 261-294.

[53] H. Zhang and J. Banfield, "Aggregation, Coarsening, and Phase Transformation in ZnS Nanoparticles Studied by Molecular Simulations," Nano Letters, 4, 713-718, 2014.

[54] M. P Allen, "Introduction to Molecular Dynamics Simulation," Computational Soft Matter, 23, 1-28, 2004.

[55] E. R. Hernández, "Molecular Dynamics: from basic techniques to applications (A Molecular Dynamics Primer)," in American Institute of Physics, Barcelona, 2018.

[56] P. W. Atkins, Physical Chemistry 6th Edition, New York: Oxford University, 1998.

[57] T. R. Forester and W. Smith, "DL_POLY_2.0: A General-purpose Parallel Molecular Dynamics Simulation Package," J. Mol. Dyn, 14, 136-141 , 1996 .

[58] R.A Buckingham, "The Classical Equation of State of Gaseous Helium, Neon and Argon," *Proceedings of the Royal Society A,*163, 264-283, 1938.

[59] D. C. Sayle, S. C. Parker, and J. Am, "Encapsulated Oxide Nanoparticles: The Influence of The Microstructure on Associated Impurities Within a Material," J. Am. Chem. Soc, 125, 8581-8594, 2003.

[60] D. Keffer, "Structural Properties from Molecular Dynamics Simulations," Knoxville, 2016.

[61] A. R. Leach, Molecular modelling: principles and applications, United Kingdom: Pearson, 2001.

[62] Y. Xue and G. A. Mansoori, "Self-Assembly of Diamondoid Molecules and Derivatives (MD Simulations and DFT Calculations)," International Journal of Molecular Sciences, 11, 288-303, 2010.

[63] A. A. Bunaciu, E. G. Udristioiu and H. Y. Aboui-Enein, "X-Ray Diffraction: Instrumentation and Applications," Critical Reviews in Analytical Chemistry, 45, 289–299, 2015.

[64] S. A. Nelson, "Earth & Environmental Sciences 2110 Mineralogy," Tulane University, Department of Earth and Environmental Science, 18 September 2018. [Online]. Available: https://www.tulane.edu/~sanelson/eens211/x-ray.htm. [Accessed 4 September 2019].

[65] A. Ali, Y. W. Chiang and R. M. Santos, "X-ray Diffraction Techniques for Mineral Characterization: A Review for Engineers of the Fundamentals, Applications, and Research Direction," Minerals, vol. 12, p. 205, 2022.

[66] A. A. Bunaciu, E. G. Udristioiu and H. Y. Aboui-Enein, "X-Ray Diffraction: Instrumentation and Applications," Critical Reviews in Analytical Chemistry, vol. 45, p. 289–299, 2015.

[67] The Editors of Encyclopaedia, "Britannica," Encyclopedia Britannica, 15 March 2022.[Online]. Available: Encyclopaedia.https://www.britannica.com/science/Bragg-law. Accessed 24 July 2023. [Accessed 22 July 2023].

[68] H. Mehrer, "Diffusion: Introduction and Case Studies in Metals and Binary Alloys," in Diffusion in Condensed Matter, Berlin, Heidelberg, Springer, 2005, 3-63.

[69] J. E. Baur, "19 - Diffusion Coefficients," in Handbook of Electrochemistry, New Mexico, USA, Elsevier, 2007, 829-848.

[70] National Research Council, Mathematical Research in Materials Science, Washington, D.C. : National Academy Press, 1993

[71] J.W. Morris, "Defects in crystals," California, Materials Science, 2013, 76-79.

[72] W. L. Hosch, "Encyclopedia Britannica," 06 10 2006. [Online]. Available: https://www.britannica.com/science/crystal-defect. [Accessed 15 11 2019].

[73] W TEC-Science, "TECS," 26 04 2018. [Online]. Available: https://www.tec-science.com/material-science/structure-of-metals/crystallographic-defects/. [Accessed 15 11 2019].

[74] M. Born and K. Huang, Dynamical Theory of Crystal Lattice, Oxford: Clarendon Press, 1954.

[75] R.S. Ledwaba, "Atomistic simulation studies of composite layered-spinel Li-Mn-O nanoarchitectures," University of Limpopo, PhD Thesis, South Africa, Polokwane, 2017.

[76] F. Li, X. Zhang, J. Lin, J. Ma, S. Zhang and G. Yang, "Unveiling the Role of Oxygen Vacancy in Li_2MnO_3 upon Delithiation," The Journal of Physical Chemistry C, 123, 23403-23409, 2019

[77] G. W. Watson. E. T. Kelsey, N. H. De Leeuw, D. J. Harris and S. C. Parker, "Atomistic Simulation of Dislocation, Surfaces and Interfaces in MgO," Journal of the Chemical Society, Faraday Transactions, 92, 433-438, 1996.

[78] R. S. Ledwaba, K. M. Kgatwane, D. C. Sayle and P. E. Ngoepe. "Structural Characterisation and Mechanical Properties of Nanosized Spinel $LiMn_2O_4$ Cathode Investigated using Atomistic Simulation," Materials Research Bulletin, 141, 111611, 2022.

[79] T. N. Nakamura, H. Gao, K. Ohta, Y. Kimura, Y. Tamenori, K. Nitta, T. Ina, M. Oishi and K. Amezawa, "Defect Chemical Studies on Oxygen Release from the Li-Rich Cathode Material $Li1.2Mn0.6Ni0.2O2-\delta$," Journal of Materials Chemistry A, 7, 5009-5019, 2019.

[80] F. X Wang, S. Y. Xiao, Z. Chang, M. X. Li. Y. P. Wu and R. Holze, "Coaxial $LiCoO_2@Li_2MnO_3$ Nanoribbon as a High Capacity Cathode for Lithium Ion Batteries," International Journal of Electrochemical Science, 9, 6182-6190, 2014.

[81] X. Y. Tu and K. Y. Shu, "X-Ray Diffraction Study on Phase Transition of Orthorhombic $LiMnO_2$ in Electrochemical Conversions," Journal of Solid State Electrochemistry, 12, 245-249, 2008.

[82] A. K. M. A. Ullah, A. K. M. F. Kibria, M. Akter, M. N. I. Khan, A. R. M. T. Shakhawat and H. Firoz, "Oxidative Degradation of Methylene Blue Using Mn_3O_4 Nanoparticles," Water Conservation Science and Engineering, 1, 249-256, 2017.

[83]   Y. Shin and K. A. Persson, "Surface Morphology and Surface Stability against Oxygen Loss of the Lithium-Excess Li_2MnO_3 Cathode Material as a Function of Lithium Concentration," ACS Applied Materials and Interfaces, 8, 25595-25602, 2016.

[84] Y. Sun, H. Wang, D. Meng, X. Li, X. Liao, H. Che, G. Cui, F. Yu, W. Yang, L. Li and Z-F. Ma, "Degradation Mechanism of O3-Type $NaNi_{1/3}Fe_{1/3}Mn_{1/3}O_2$ Cathode Materials During Ambient Storage and Their In Situ Regeneration," ACS Applied Energy Materials, 4, 2061-2067, 2021.

[85] Z. Xue, X. Qi, L. Li, W. Ii, L. Xu, Y. Xie, X. Lai, G. Hu, Z. Peng, Y. Cao and K. Du, "Sodium Doping to Enhance Electrochemical Performance of Overlithiated Oxide

Cathode Materials for Li-Ion Batteries via Li/Na Ion-Exchange Method," American Chemical Society Applied Materials and Interfaces, 10, 27141-27149, 2018.

[86] X. Dong, Y. Xu, L. Xiong, X. Sun and Z. Zhang, "Sodium Substitution for Partial Lithium to Significantly Enhance the Cycling Stability of Li_2MnO_3 Cathode Material," Journal of Power Sources, 243, 78-87, 2013.

[87] R-P. Qing, J-L. Shi, D-D. Xiao, X-D. Zhang, Y-X. Yin, Y-B. Zhai, L. Gu and Y-G. Guo, "Enhancing the Kinetics of Li-Rich Cathode Materials through the Pinning Effects of Gradient Surface Na+ Doping," Advanced Energy Materials, 6, 1501914, 2016.

[88] Y. Yang, H. Su, T. Wu, Y. Jiang, D. Liu, P. Yan, H. Tian and H. Yu, "Atomic Pair Distribution Function Research on Li_2MnO_3 Electrode Structure Evolution," Science. Bulletin, 64, 553-561, 2019.

[89] S. Chen, Z. Chen, M. Xia, C. Cao and Y. Luo, "Toward Alleviating Voltage Decay by Sodium Substitution in Lithium-Rich Manganese-Based Oxide Cathodes," Energy Materials, 1, 4065-4074, 2018.

Appendix A

Conference Presentations and Publications

Presentations

1. Synthesis of Li_2MnO_3 nanoarchitectures using amorphisation and recrystallisation technique (oral presentation), Faculty of Science and Agriculture research day (FSA), Fusion Boutique, Polokwane, 20-21 September 2018.

2. Exploration of intermediate phases that form during lithium and oxygen extraction from the Li_2MnO_3 nanoporous cathode material (poster presentation), South African Institute of Physics (SAIP) Conference, Protea Hotel The Ranch Resort, Polokwane, 8-12 July 2019.

3. The structural behaviour of simulated Li_2MnO_3 nanoarchitectures during lithium and oxygen extraction (oral presentation), Faculty of Science and Agriculture Research day, Protea Hotel The Ranch Resort, Polokwane,19-20 September 2019.

4. Simulated crystal growth of intermediate phases formed during Li and O extraction of nano-Li_2MnO_3 cathode material (poster presentation), Electrochemical Society (ECS) Conference, Hilton Hotel, Atlanta Ga (USA), 13-17 October 2019.

5. Structural variation of nano-Li_2MnO_3 cathode material during Li and O extraction (poster presentation), Centre for High-Performance Computing (CHPC) Conference, Birchwood Hotel, Johannesburg,1-5 December 2019.

6. Simulated amorphisation and recrystallisation of nano-Li_2MnO_3 cathodes during Li/O extraction (poster presentation), Women in STEM conference, Premier Hotel, East London,17-20 February 2020.

7. The simulated synthesis of nanostructured Li_2MnO_3 cathode materials (online presentation), South African Institute of Physics (SAIP), online, 23-30 July 2021.

8. The effect of sodium substitution on the lithium sites of Li_2MnO_3 cathode materials for lithium-ion batteries (macro-talk presentation), Centre for High-Performance Computing (CHPC), online, 1-3 December 2021.

9. Exploring the effect of sodium substitution on Li_2MnO_3 nanostructured cathodes for lithium-ion batteries (oral presentation), Faculty of Science and Agriculture Research Day, Bolivia Lodge, Polokwane, 21-23 September 2022.

10. Investigating the effect of sodium partial substitution on nanostructured Li_2MnO_3 cathodes during the simulated charge process (poster presentation), South African Institute of Physics (SAIP) Conference, University of Zululand,Kwazulu Natal,3-7 July 2023.

Awards

1. Most outstanding MSc poster presentation in the condensed matter physics and materials division. Exploration of intermediate phases that form during lithium and oxygen extraction from the Li_2MnO_3 nanoporous cathode material, South African Institute of Physics (SAIP), Protea Hotel The Ranch Resort, Polokwane, 8-12 July 2019.

2. PhD oral presentation 1st place. Exploring the effect of sodium substitution on Li_2MnO_3 nanostructured cathodes for lithium-ion batteries, Faculty Research Day (FSA), Bolivia Lodge, Polokwane, 21-23 September 2022.

3. Most outstanding PhD poster presentation in the condensed matter physics and materials division. Investigating the effect of sodium partial substitution on nanostructured Li_2MnO_3 cathodes during the simulated charge process, South African Institute of Physics (SAIP) Conference, University of Zululand, Kwazulu Natal,3-7 July 2023.

Publications

1. T. Mogashoa, R. S. Ledwaba and P. E. Ngoepe, "Analyzing the Implications of Charging of Nanostructured Li_2MnO_3 Cathode Materials for Lithium-Ion Battery Performance" Materials 2022, 15, 5687. https://doi.org/10.3390/ma15165687.